

DISSERTATION

Basil Mohammad Darras

The Graduate School
University of Kentucky

2008

INTEGRATED THERMO-MECHANICAL INVESTIGATIONS OF FRICTION STIR
PROCESSING OF LIGHT WEIGHT ALLOYS

DISSERTATION

A dissertation submitted in partial fulfillment of the requirements
for the degree of Doctor of Philosophy in
Mechanical Engineering at the
University of Kentucky

By
Basil Mohammad Darras

Lexington, Kentucky

Director: Dr. Marwan Khraisheh, Professor of Mechanical Engineering

Lexington, Kentucky

2008

Copyright © Basil Mohammad Darras 2008

UMI Number: 3301318

Copyright 2008 by
Darras, Basil Mohammad

All rights reserved.

INFORMATION TO USERS

The quality of this reproduction is dependent upon the quality of the copy submitted. Broken or indistinct print, colored or poor quality illustrations and photographs, print bleed-through, substandard margins, and improper alignment can adversely affect reproduction.

In the unlikely event that the author did not send a complete manuscript and there are missing pages, these will be noted. Also, if unauthorized copyright material had to be removed, a note will indicate the deletion.

UMI[®]

UMI Microform 3301318

Copyright 2008 by ProQuest LLC.

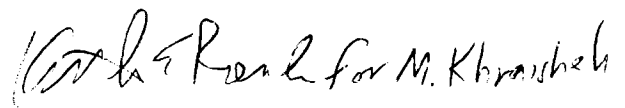
All rights reserved. This microform edition is protected against
unauthorized copying under Title 17, United States Code.

ProQuest LLC
789 E. Eisenhower Parkway
PO Box 1346
Ann Arbor, MI 48106-1346

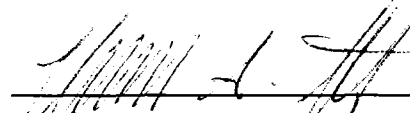
INTEGRATED THERMO-MECHANICAL INVESTIGATIONS OF FRICTION STIR
PROCESSING OF LIGHT WEIGHT ALLOYS

By

Basil Mohammad Darras

Handwritten signature of M. Khraish

Director of Dissertation

Handwritten signature of M. Khraish

Director of Graduate Studies

02/19/2008

ABSTRACT OF DISSERTATION

Basil Mohammad Darras

The Graduate School
University of Kentucky

2008

INTEGRATED THERMO-MECHANICAL INVESTIGATIONS OF FRICTION STIR
PROCESSING OF LIGHT WEIGHT ALLOYS

ABSTRACT OF DISSERTATION

A dissertation submitted in partial fulfillment of the requirements
for the degree of Doctor of Philosophy in
Mechanical Engineering at the
University of Kentucky

By
Basil Mohammad Darras

Lexington, Kentucky

Director: Dr. Marwan Khraisheh, Professor of Mechanical Engineering

Lexington, Kentucky

2008

Copyright © Basil Mohammad Darras 2008

ABSTRACT OF DISSERTATION

INTEGRATED THERMO-MECHANICAL INVESTIGATIONS OF FRICTION STIR PROCESSING OF LIGHT WEIGHT ALLOYS

The phenomenon of friction stirring is extensively used and researched in the field of welding (FSW). On observing the advantages associated with FSW, mainly the grain refinement, the phenomenon is being extended to processing of commercial alloys. Friction Stir Processing (FSP) is a new advanced material processing technique used to refine and homogenize the microstructure of sheet metals. FSP is a solid-state process and the material within the processed zone undergoes intense plastic deformation. To conduct FSP, a specially-designed rotating tool, which consists of a pin and a shoulder, is used. The rotating pin is plunged into the sheet, traversing in the desired direction, while the shoulder rubbing the surface of the sheet generates enough heat to soften the material below its melting temperature. The mechanical stirring caused by the plunged rotating pin forces the softened material to undergo intense plastic deformation, which yields a processed zone characterized by dynamically recrystallized fine grain structure.

In this work, a multi-disciplinary integrated approach is adapted to give more understanding of the process itself. Analytical modeling, numerical modeling, microstructural and hardness characterization and thermal investigations have been done throughout this work. The results show the effects of different process parameters on the resulting microstructure, hardness, temperature distributions, strain-rate distributions and material flow during FSP.

KEYWORDS: Friction Stir Processing, Microstructural Modification, Analytical Modeling, Strain Rate Distributions, Velocity Fields.

A handwritten signature in black ink, consisting of several fluid, connected strokes, positioned above a horizontal line.

02/18/2008

TO MY PARENTS

ACKNOWLEDGEMENT

Firstly I would like to thank my advisor, Dr. Marwan Khraisheh for his continuous support, mentoring, advising, and guidance extended throughout the period I spent at University of Kentucky.

I also would like to thank Dr. Mohamed Hassan Ali for introducing me to the CFD code (STAR-CCM+). And I would like to express my sincere gratitude to Mr. VonKuster for his technical support and guidance throughout the course of the experiments.

Also I would like to thank my research team members and my friends, with whom I've shared and discussed this project in several versions. Above all, I would like to thank my parents, brothers, sisters and wife for their continuous support and motivation.

TABLE OF CONTENTS

| | |
|-----------------------|-----|
| ACKNOWLEDGEMENT | iii |
| LIST OF TABLES | vi |
| LIST OF FIGURES | vii |

Chapter One

| | |
|------------------------------------|---|
| 1. INTRODUCTION | 2 |
| 1.1 Statement of Problem..... | 2 |
| 1.2 Motivations | 3 |
| 1.3 Objective and Methodology..... | 4 |
| 1.4 Dissertation Layout..... | 5 |

Chapter Two

| | |
|--|----|
| 2. BACKGROUND | 8 |
| 2.1 Superplastic Forming (SPF)..... | 8 |
| 2.2 Grain Refinement..... | 14 |
| 2.3 Friction Stir Processing (FSP) | 16 |
| 2.4 Previous Work | 18 |

Chapter Three

| | |
|-----------------------------------|----|
| 3. EXPERIMENTAL SETUP..... | 25 |
| 3.1 Material | 25 |
| 3.2 Tools and Equipments | 27 |
| 3.3 Experimental Procedures | 30 |
| 3.4 Process Parameters | 31 |

Chapter Four

| | |
|--|----|
| 4. MICROSTRUCTURE AND HARDNESS CHARACTERIZATION..... | 36 |
| 4.1 Previous Work | 36 |
| 4.2 Experimental Setup and Procedures | 40 |
| 4.3 Microstructure..... | 41 |
| 4.4 Hardness..... | 50 |
| 4.5 Conclusions..... | 54 |

Chapter Five

| | |
|--|----|
| 5. EXPERIMENTAL THERMAL INVESTIGATION..... | 56 |
| 5.1 Previous Work | 56 |
| 5.2 Experimental Setup..... | 58 |
| 5.3 Results & Discussion | 60 |
| 5.4 Conclusions..... | 72 |

| | |
|---|-----|
| <i>Chapter Six</i> | |
| 6. ANALYTICAL MECHANICAL MODEL..... | 74 |
| 6.1 Previous Work | 74 |
| 6.2 Current Model..... | 81 |
| 6.2-1 Model Development..... | 84 |
| 6.2-2 State-variables | 86 |
| 6.2-3 Weight functions | 88 |
| 6.2-4 Velocity fields | 89 |
| 6.2-5 Strain rate | 90 |
| 6.3 Results and Discussion | 91 |
| 6.3-1 Shoulder and pin effects | 91 |
| 6.3-2 Rotational and translational speeds effects..... | 95 |
| 6.3-3 Interfacial contact conditions..... | 98 |
| 6.3-4 Tool geometry (Pin diameter/Shoulder diameter ratio)..... | 106 |
| 6.3-5 Validation of current results..... | 108 |
| 6.4 Conclusions..... | 110 |
| <i>Chapter Seven</i> | |
| 7. CFD SIMULATION..... | 112 |
| 7.1 Previous Work | 112 |
| 7.2 STAR-CCM+ CFD Code..... | 115 |
| 7.3 Model Description | 117 |
| 7.4 Results and Discussions..... | 120 |
| 7.5 Conclusions..... | 128 |
| <i>Chapter Eight</i> | |
| 8. SUMMARY AND RECOMMENDATIONS..... | 130 |
| 8.1 Concluding Remarks..... | 130 |
| 8.2 Unique Features & Contributions..... | 131 |
| 8.3 Recommendations for Future Work | 132 |
| REFERENCES | 133 |
| VITA..... | 145 |

LIST OF TABLES

| | |
|--|----|
| Table 3- 1 composition of AA5052 alloy [52]..... | 25 |
| Table 3- 2 composition of Mg AZ31 alloy [52]..... | 26 |
| Table 3- 3 Rotational and translational speeds used for FSP different materials..... | 31 |
| Table 4-1 Average grain size for Mg AZ31B-O alloy, as-received and FS processed samples..... | 47 |
| Table 6- 1 Nomenclature..... | 83 |

LIST OF FIGURES

| | |
|--|----|
| <i>Figure 1- 1 Overall research framework</i> _____ | 5 |
| <i>Figure 2- 1 Superplasticity in the Pb-Sn eutectic alloy pulled in tension at 140 °C [1].</i> _ | 9 |
| <i>Figure 2- 2 Schematic of superplastic forming process [2].</i> _____ | 10 |
| <i>Figure 2- 3 SPF applications a) wing tip for the Boeing 777 [3], b) Aston Martin car panels [3] , c) dental implant superstructure [4] and d) art and architecture[3].</i> ____ | 11 |
| <i>Figure 2- 4 Characteristic curve of superplastic material showing the effect of using fine grain structure.</i> _____ | 13 |
| <i>Figure 2- 5 The effect of grain size on the tensile ductility of 7475 Aluminum Superplastic alloy [5].</i> _____ | 13 |
| <i>Figure 2- 6 Schematic of equal channel angular extrusion (ECAE) process [6].</i> ____ | 15 |
| <i>Figure 2- 7 Schematic of torsional strain severe plastic deformation ((TS)-SePD) process [7].</i> _____ | 15 |
| <i>Figure 2- 8 Schematic of friction stir processing.</i> _____ | 17 |
| <i>Figure 3- 1 Different FSP tool configurations [55].</i> _____ | 27 |
| <i>Figure 3- 2 HAAS VF-0F CNC vertical milling machine.</i> _____ | 28 |
| <i>Figure 3- 3 Single pass setup[55].</i> _____ | 28 |
| <i>Figure 3- 4 Multi passes setup.</i> _____ | 29 |
| <i>Figure 3- 5 Different sheet thicknesses and higher load setup which is equipped with a cooling system.</i> _____ | 29 |
| <i>Figure 3- 6 Schematics of the stages of friction stir processing (FSP)[55].</i> _____ | 30 |
| <i>Figure 3- 7 Successfully FS processed AA5052 samples at a) 500 rpm and 2.0 in. /min. and b) 600 rpm and 2.0 in. /min. (Tool is 0.5” shoulder diameter, flat pin and flat shoulder).</i> _____ | 32 |
| <i>Figure 3- 8 Defective FS processed Mg AZ31 samples, processed at typical Aluminum alloys FSP conditions. a) 800 rpm and 2.0 in. /min. and b) 400 rpm and 2.0 in. /min. (Tool is 0.5” shoulder diameter, flat pin and flat shoulder).</i> _____ | 32 |
| <i>Figure 3- 9 Successfully FS processed Mg AZ31B-H24 samples at a) 1200 rpm and 22 in. /min. And b) 1200 rpm and 25 in. /min. (Tool is 0.5” shoulder diameter, flat pin and flat shoulder).</i> _____ | 33 |

| | |
|---|----|
| <i>Figure 3- 10 Mg AZ31B-H24 samples processed at a) 1200 rpm and 15.0 in. /min., and b) 1500 rpm and 18.0 in. /min. (Tool is 0.75" shoulder diameter, flat pin and concave shoulder).</i> | 33 |
| <i>Figure 3- 11 Mg AZ31B-O samples processed at a) 2500 rpm and 12.0 in. /min., and b) 1750 rpm and 12.0 in. /min. (Tool is 0.75" shoulder diameter, flat pin and concave shoulder).</i> | 34 |
| <i>Figure 4- 1 Schematic shows the tested area within the FS processed area.</i> | 41 |
| <i>Figure 4- 2 Microstructure of AZ31B-H24 Mg a) as-received, b) FS processed sample at 1200 rpm and 22 in. /min., and c) FS processed sample at 1200 rpm and 25 in. /min.</i> | 43 |
| <i>Figure 4- 3 Microstructure of an as-received Mg AZ31B-O sample (Average grain size is 8.9 μm).</i> | 44 |
| <i>Figure 4- 4 Microstructure of Mg AZ31B-O sample FS processed at 1000 rpm and 12 in/min (Average grain size is 5.2 μm).</i> | 45 |
| <i>Figure 4- 5 Microstructure of Mg AZ31B-O sample FS processed at 1200 rpm and 12 in/min (Average grain size is 6.1 μm).</i> | 45 |
| <i>Figure 4- 6 Microstructure of Mg AZ31B-O sample FS processed at 1750 rpm and 12 in/min (Average grain size is 8.1 μm).</i> | 45 |
| <i>Figure 4- 7 Microstructure of Mg AZ31B-O sample FS processed at 2500 rpm and 12 in/min (Average grain size is 14.4 μm).</i> | 46 |
| <i>Figure 4- 8 Microstructure of Mg AZ31B-O sample FS processed at 1200 rpm and 8 in/min (Average grain size is 5.8 μm).</i> | 46 |
| <i>Figure 4- 9 Microstructure of Mg AZ31B-O sample FS processed at 1200 rpm and 15 in/min (Average grain size is 5.4 μm).</i> | 46 |
| <i>Figure 4- 10 Microstructure of Mg AZ31B-O sample FS processed at 1200 rpm and 20 in/min (Average grain size is 4.7 μm).</i> | 47 |
| <i>Figure 4- 11 Effect of rotational speed on the resulting grain size of FS processed Mg AZ31B-O sample (translational speed is 12 in/min).</i> | 48 |
| <i>Figure 4- 12 Effect of translational speed on the resulting grain size of FS processed Mg AZ31B-O samples (rotational speed is 1200 rpm).</i> | 48 |
| <i>Figure 4- 13 OIM maps for the grain structure of AA5052 sheet; a) as-received (13.4 μm), b) FSP @ 1000 rpm and 2.5 in/min (4.5 μm) and c) FSP @ 600 rpm and 2.5 in/min (1.7</i> | |

| | |
|---|----|
| $\mu\text{m})$ (In collaboration with Department of Mechanical Engineering, FAMU-FSU) [12,55] _____ | 49 |
| Figure 4- 14 grain structure at different locations of the FS processed AA5052 sheet, at two different conditions using OIM (In collaboration with Department of Mechanical Engineering, FAMU-FSU) [55] _____ | 49 |
| Figure 4- 15 Variation of hardness of FS processed AZ31B-H24 magnesium sample with translational speed (rotational speed is 1200 rpm.). _____ | 51 |
| Figure 4- 16 Variation of the hardness of FS processed AZ31B-H24 magnesium sample with rotational speed (translational speed is 30.0 in. /min.). _____ | 51 |
| Figure 4- 17 Hardness variation within the thickness of FS processed AZ31B-H24 magnesium sample (1200 rpm and 22 in /min). _____ | 53 |
| Figure 4- 18 Transverse hardness profile of FS processed AZ31B-H24 magnesium sample (1200 rpm and 30 in /min). _____ | 53 |
| Figure 5- 12 Two-dimensional thermal map obtained using infrared camera. _____ | 59 |
| Figure 5- 13 Experimental setup _____ | 60 |
| Figure 5- 14 Two-dimensional thermal map obtained using infrared camera, which shows the measured contact point. _____ | 61 |
| Figure 5- 15 Effect of Translational speed on the contact point temperature (fixed rotational speed 500 rpm) (AA5052 samples). _____ | 61 |
| Figure 5- 16 Effect of Rotational speed on the contact point temperature (fixed translational speed 2 inch/min) (AA5052 samples). _____ | 62 |
| Figure 5- 17 Effect of rotational speed on maximum temperature reached during FSP of AA5052 samples. _____ | 63 |
| Figure 5- 18 Effect of rotational speed on the resulting grain size of FS processed AA5052 samples. _____ | 64 |
| Figure 5- 19 Close-up of the steady part of the 600 rpm curve (AA5052 samples). _____ | 65 |
| Figure 5- 20 Average hardness (HV) of FS processed AA5052 sample at different longitudinal positions (FSP at 500 rpm and 2 inch/min). _____ | 66 |
| Figure 5- 21 Two-dimensional thermal map obtained using infrared camera, which shows the measured longitudinal segment. _____ | 67 |

| | |
|--|-----|
| <i>Figure 5- 22 Temperature distribution of a longitudinal segment during FSP at different rotational speeds (fixed translational speed 2 inch/min) (AA5052 samples).</i> | 67 |
| <i>Figure 5- 23 Close-up of the 600 rpm curve (AA5052).</i> | 68 |
| <i>Figure 5- 24 Temperature histories for a point during FSP of Mg AZ31B-H24 sheets at different rotational speeds.</i> | 70 |
| <i>Figure 5- 25 Temperature histories for a point during FSP of Mg AZ31B-H24 sheets at different Translational speeds.</i> | 70 |
| <i>Figure 5- 26 Effect of rotational speed on the maximum temperature reached during FSP of Mg AZ31B-H24 samples (translational speed is 22 in/min).</i> | 71 |
| <i>Figure 5- 27 Effect of translational speed on the maximum temperature reached during FSP of Mg AZ31B-H24 samples (rotational speed is 1200 rpm).</i> | 71 |
| <i>Figure 6- 1 Model's geometry a) 3-D and b) cross section EE</i> | 86 |
| <i>Figure 6- 2 Velocity fields for FSP at 400 rpm and 0.847 mm/s a) pin alone b) shoulder alone c) combined shoulder and pin</i> | 93 |
| <i>Figure 6- 3 Strain rate distributions for FSP at 400 rpm and 0.847 mm/s a) pin alone b) shoulder alone c) combined shoulder and pin</i> | 94 |
| <i>Figure 6- 4 Velocity field for FSP at a) 400 rpm and 0.847 mm/s b) 600 rpm and 0.847 mm/s c) 400 rpm and 2.540 mm/s</i> | 96 |
| <i>Figure 6- 5 Strain rate distributions for FSP at a) 400 rpm and 0.847 mm/s b) 600 rpm and 0.847 mm/s c) 400 rpm and 2.540 mm/s</i> | 97 |
| <i>Figure 6- 6 Velocity field for separate shoulder effect scenario (FSP at 400 rpm and 0.847 mm/s) a) full sticking at the shoulder/sheet interface (A=1.0), b) 50% sticking at the shoulder/sheet interface (A=0.5), and c) 25 % sticking at the shoulder/sheet interface (A=0.25)</i> | 99 |
| <i>Figure 6- 7 Strain rate distribution for separate shoulder effect scenario (FSP at 400 rpm and 0.847 mm/s) a) full sticking at the shoulder/sheet interface (A=1.0), b) 50% at the shoulder/sheet interface sticking (A=0.5), and c) 25 % sticking at the shoulder/sheet interface (A=0.25)</i> | 100 |
| <i>Figure 6- 8 Velocity field for separate pin effect scenario (FSP at 400 rpm and 0.847 mm/s) a) Full sticking at the pin/sheet interface (C=1.0), b) 50% sticking at the pin/sheet interface (C=0.5), and c) 25 % sticking at the pin/sheet interface (C=0.25)</i> | 101 |

| | |
|--|-----|
| <i>Figure 6- 9 Strain rate distribution for separate pin effect scenario (FSP at 400 rpm and 0.847 mm/s) a) full sticking at the pin/sheet interface (C=1.0), b) 50% sticking at the pin/sheet interface (C=0.5), and c) 25 % sticking at the pin/sheet interface (C=0.25)</i> | 102 |
| <i>Figure 6- 10 Velocity field for combined shoulder/pin effect scenario (FSP at 400 rpm and 0.847 mm/s) a) full sticking at the shoulder/sheet interface (A=1.0) and full sticking at the pin/sheet interface (C=1.0), b) 50% at the shoulder/sheet interface sticking (A=0.5) and full sticking at the pin/sheet interface (C=1.0), c) full sticking at the shoulder/sheet interface (A=1.0) and 50% sticking at the pin/sheet interface (C=0.5), and d) 50% sticking at the shoulder/sheet interface (A=0.5) and 50% sticking at the pin/sheet interface (C=0.5)</i> | 104 |
| <i>Figure 6- 11 Strain rate distribution for combined shoulder/pin effects scenario (FSP at 400 rpm and 0.847 mm/s) a) full sticking at the shoulder/sheet interface (A=1.0) and full sticking at the pin/sheet interface (C=1.0), b) 50% at the shoulder/sheet interface sticking (A=0.5) and full sticking at the pin/sheet interface (C=1.0), c) full sticking at the shoulder/sheet interface (A=1.0) and 50% sticking at the pin/sheet interface (C=0.5), and d) 50% sticking at the shoulder/sheet interface (A=0.5) and 50% sticking at the pin/sheet interface (C=0.5)</i> | 106 |
| <i>Figure 6- 12 Velocity fields for different (r_p/r_s) ratios (FSP at 400 rpm and 0.847 mm/s) a) (r_p/r_s) = 1/2, and b) (r_p/r_s) = 1/3</i> | 107 |
| <i>Figure 6- 13 Effective strain rate distribution for different (r_p/r_s) ratios (FSP at 400 rpm and 0.847 mm/s) a) (r_p/r_s) = 1/2, and b) (r_p/r_s) = 1/3</i> | 108 |
| <i>Figure 6- 14 Predicted shape of the deformation zone (Velocity field for FSP at 400 rpm and 0.847 mm/s)</i> | 109 |
| <i>Figure 6- 15 Macrostructure of FS processed zone (a) Ericsson et al. [84] and (b) Hassan et al. [85].</i> | 109 |
| <i>Figure 7- 1 Model's geometry.</i> | 118 |
| <i>Figure 7- 2 Meshed geometry.</i> | 119 |
| <i>Figure 7- 3 Effect of rotational speed on the velocity field of a traverse section of FS processed zone; a) FSP at 400 rpm and 0.847 mm/s, b) FSP at 600 rpm and 0.847 mm/s, and c) FSP at 800 rpm and 0.847 mm/s).</i> | 121 |

Figure 7- 4 Effect of translational speed on the velocity field of a traverse section of FS processed zone; a) FSP at 400 rpm and 0.847 mm/s and b)FSP at 400 rpm and 0.847 mm/s. _____ 122

Figure 7- 5 Velocity fields of a traverse section of FS processed zone (FSP at 600 rpm and 0.847 mm/s), using a) CFD analysis, and b) analytical model proposed in Chapter Six). _____ 123

Figure 7- 6 Maximum material's velocity at different rotational speeds using both CFD analysis and analytical model presented in chapter 6. _____ 124

Figure 7- 7 Material's velocity at different radial locations at the middle of the sheet thickness using both CFD analysis and analytical model presented in chapter 6 ____ 124

Figure 7- 8 a) Different sections within the model's geometry, b) velocity vector field of a traverse section of FS processed zone (section A-A), c) velocity vector field of a section taken at the middle the sheet thickness (section C-C),and d) velocity vector fields of a section taken along the FS processed pass(section B-B). (FSP at 800 rpm and 0.847 mm/s). _____ 127

Chapter One

INTRODUCTION

1. INTRODUCTION

1.1 Statement of Problem

The environmental and the economical issues which are facing the world (especially in transportation fields) make research on lightweight alloys as a primary interest in both scientific and industrial communities. However, the limited formability of light weight alloys at room temperature presents a major challenge for both automotive and aerospace applications. One way to overcome the obstacle in improving the formability is to refine and homogenize the microstructure; and to use advanced forming techniques, such as superplastic forming (SPF), to form sheet metals at elevated temperatures. The Superplastic Forming (SPF) technique utilizes a unique class of materials that has extraordinarily large tensile ductility. The influence of grain size on superplastic properties is significant; smaller grain size and more homogenous grain structure improves the superplastic behavior of the material, and consequently advances the SPF technique.

The difficulty in producing ultrafine grain-structured sheet metals still hinders the widespread utilization of lightweight alloys. In general; conventional grain refinement techniques are costly, time consuming and negatively affect the environment. Although there are some advanced processing techniques which effectively refine the grain structure, such as: equal channel angular extrusion (ECAE) and torsional strain severe plastic deformation (TS)-SePD, their limited size capabilities, high load and long processing time limit the widespread utilization of such techniques.

One innovative technique that can be used to produce fine and homogenous grain structure is Friction Stir Processing (FSP), which is based on Friction Stir Welding (FSW). Friction Stir Processing is becoming an acceptable technique for modifying the grain structure of sheet metals. FSP is a solid-state technique in which a specially designed cylindrical tool is plunged into the sheet causing intense plastic deformation through stirring action, yielding a defect free and dynamically recrystallized fine-grained microstructure. Some of the main advantages of FSP over other refinement techniques are: it is a single step process which uses simple tooling, it can be easily automated, and it is an environmentally friendly and energy efficient process.

1.2 Motivations

Since the concept of FSP is relatively new, there are many areas, which need thorough investigation to optimize the process and make it commercially viable. The lack of available data correlating process parameters to thermal histories, resulting microstructure and consequently the mechanical properties for different light weight alloys, is one of the major issues facing the widespread utilization of FSP. Moreover, there are very limited predictive models that can accurately describe the FSP process. Therefore, there is a great need to develop a predictive model that can accurately predict the resulting microstructure from process parameters, which is an important step towards designing the material microstructure.

1.3 Objective and Methodology

The main objective of this work is to develop a physics-based model based on theory and experiments that can accurately predict the strain-rate distribution and the material flow during friction stir processing. This model can serve as a first step towards using FSP to “design” a certain microstructure for optimum performance. This goal is achieved through the following phases.

- Designing an effective experimental setup to conduct friction stir processing. This includes building a fixture to conduct the tests on, and designing the FSP tool with different configurations.
- Investigating the effects of different process parameters on the resulting microstructure. The microstructure of different FSP samples that have been processed at different rotational speed, translational speed, tool geometries and thermal conditions is characterized.
- Investigating the effect of FSP on the resulting mechanical properties of the FS processed material. This will include microhardness testing as well as tensile testing.
- Thermal investigations; which include measuring temperature distributions associated with the process.
- Analytical modeling of the FS process based on an integrated thermo-mechanics approach.
- Simulation of the process using computational continuum mechanics algorithms (STAR-CCM+). Material flow and velocity fields during the process are the main outputs.

To develop a comprehensive model and to give more understanding to the physics of the process itself; an integrated multidisciplinary approach is adapted in this work. The

framework of this research involves analytical, numerical and experimental efforts. The current research framework is shown in *Figure 1-1*.

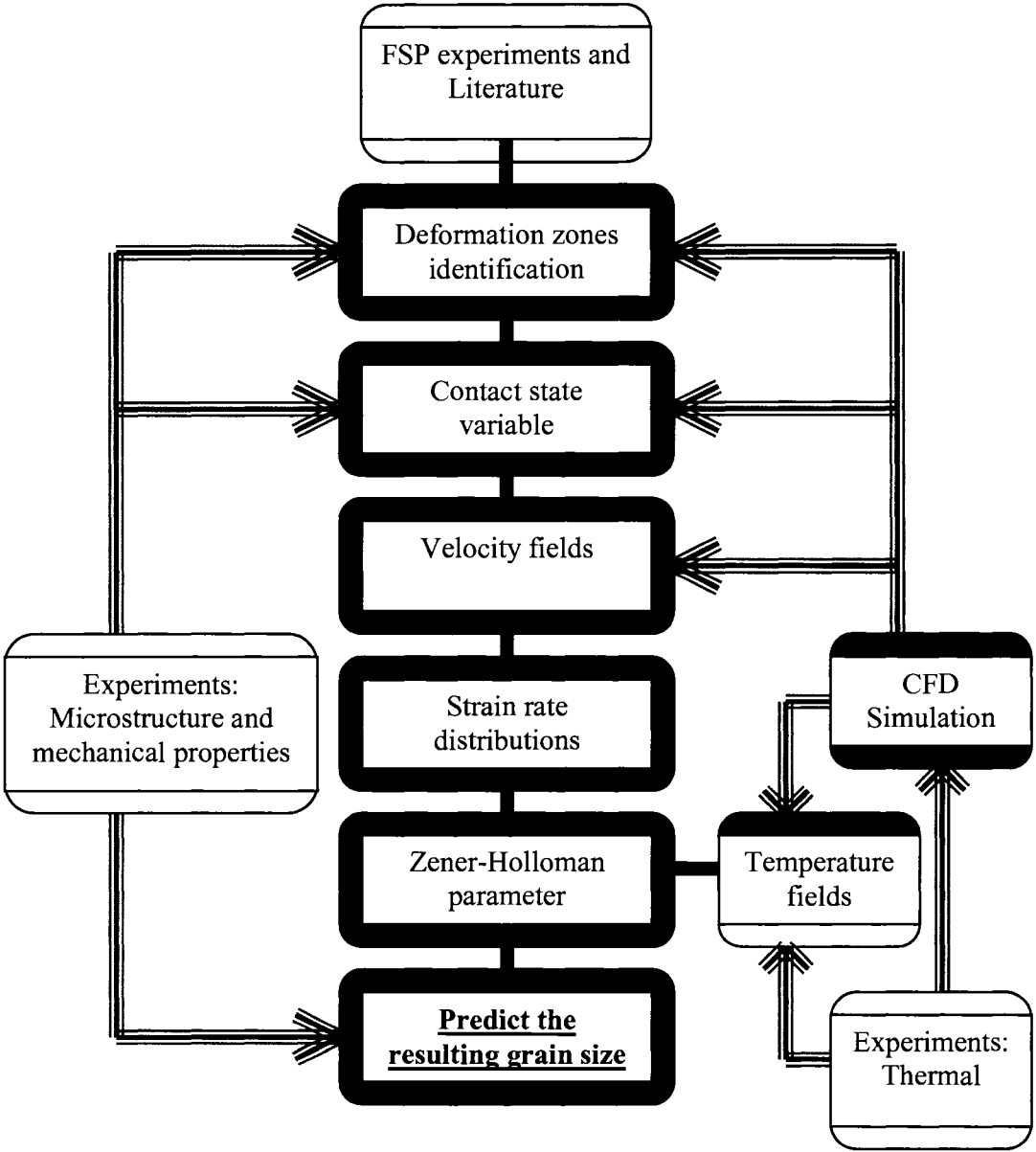


Figure 1- 1Overall research framework

1.4 Dissertation Layout

This dissertation consists of eight chapters. In *Chapter Two*; an overview about forming lightweight alloys, superplastic forming, and grain refinement techniques are

presented. This chapter also gives an introduction about friction stir processing; how it started, how it works, its advantages and limitations, and some the previous work that had been in done in the field, are all briefly discussed. In *Chapter Three*; the experimental setup that has been used throughout this work to conduct friction stir processing, in addition to the materials and process parameters used, are all presented. *Chapter Four* presents the microstructural and hardness investigations of the friction stir processed material. Literature review about the subject is first presented, and then microstructural and hardness results are discussed. Experimental thermal investigations are discussed in *Chapter Five*; the previous work which had been done is discussed, and results related to peak temperature, thermal distributions, heating and cooling curves are all discussed. *Chapter Six* presents the analytical mechanical model; a detailed literature review about modeling activities that have been taking place is presented. Model development is explained in details. Results that show the model capabilities in predicting velocity fields and strain rate distributions for different process parameters, interfacial conditions, and tool geometries are discussed. And finally, validation through comparing the velocity field generated by the model with the shape of the experimentally-determined deformation field is also presented. In *Chapter Seven*, numerical modeling through CFD simulations, in order to determine velocity fields and material flow during FSP, is presented. The last chapter (*Chapter Eight*) concludes this work with final remarks, contributions and unique features and recommendation for future work.

Chapter Two

BACKGROUND

2. BACKGROUND

Forming and Formability of light weight alloys at room temperatures for aerospace and automotive applications present a major challenge. One way to improve the formability is to refine and homogenize the microstructure and form the sheet at high temperatures using advanced forming techniques such as superplastic forming. Superplastic Forming (SPF) is a forming process used with superplastic materials, a unique class of metals that has the ability to undergo extraordinary tensile ductility. An elongation in excess of 200% is usually indicative of superplasticity. It is the large ductility that attracted many investigators due to the potential benefits in the area of metal forming. The widespread use of SPF has been hampered by a number of issues including cost of initial processing to prepare superplastic materials and slow forming process due to low optimum forming strain rate. The influence of grain size on superplastic properties is significant. The optimum superplastic forming strain rate is increased by decreasing grain size which means faster forming time.

2.1 Superplastic Forming (SPF)

Superplastic forming (SPF) is an advanced near-net shape forming technique used to form a unique class of metals: superplastic materials which have extraordinary tensile ductility that exceeds 200% [1]. *Figure 2-1* shows an example of the extraordinary tensile

ductility of a superplastic material. Aluminum alloys, magnesium alloys, titanium alloys, iron alloys and other composites and ceramics are examples of superplastic material.

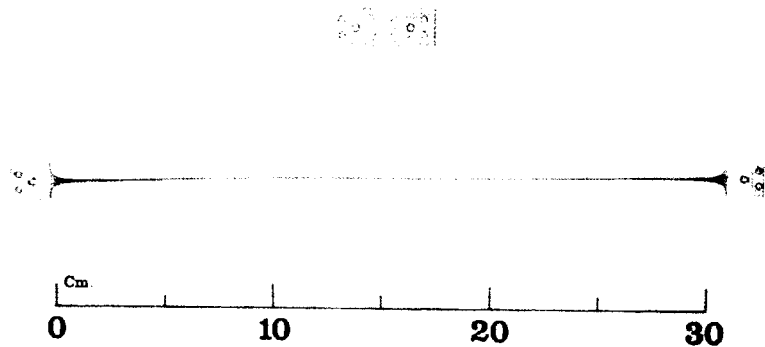


Figure 2- 1 Superplasticity in the Pb-Sn eutectic alloy pulled in tension at 140 °C [1].

There are certain **requirements** that are needed to achieve superplastic behavior. The first requirement is to have a fine and stable grain structure; the reason why fine and equiaxed grains are required to achieve superplasticity is that grain boundary sliding is the dominant mechanism during superplastic deformation. High temperature is another important requirement; in general temperature greater than one half of the melting temperature is needed. Lastly, the deformation rate need to be controlled in order to achieve superplastic behavior, typically a strain rate between 10^{-5} s^{-1} and 10^{-1} s^{-1} is used for conventional superplastic materials.

The most common practice that has been used to form superplastic materials is the gas blow forming in which a pressurized gas is used to form the sheet into the desired shape in single step using single die. *Figure 2-2* shows a schematic which illustrates Superplastic forming process.

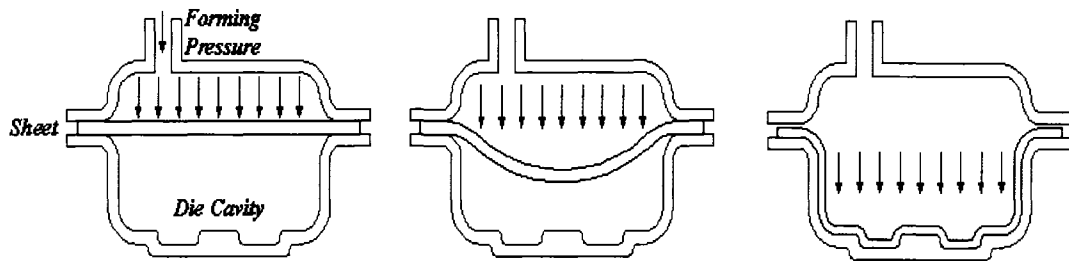


Figure 2- 2 Schematic of superplastic forming process [2].

SPF offers many *advantages* over conventional forming techniques; such as:

- The ability to form complex shapes.
- Great design flexibility.
- Low die cost (single die).
- Reduced number of fasteners and joints.
- The ability to form hard material.
- Reduced number of forming steps

However; there are still some *limitations* which keep SPF from being used on large scale; and some of these limitations are:

- Slow forming process.
- Limited predictive capabilities of deformation failure, and lack of comprehensive data regarding superplastic materials.

- Pre-forming steps, like getting fine grain structure sheets.

Currently aerospace industry is where SPF applications are mostly used. Different titanium and aluminum alloys have been superplastically formed to produce different components for aerospace industry such as: electrical devices, gate panels and other small structural elements. Other applications for SPF includes: car panels but it is still limited due to high cost and low production rate, medical and dental implants and in art and architecture. *Figure 2-3* shows parts that have been produced using SPF.

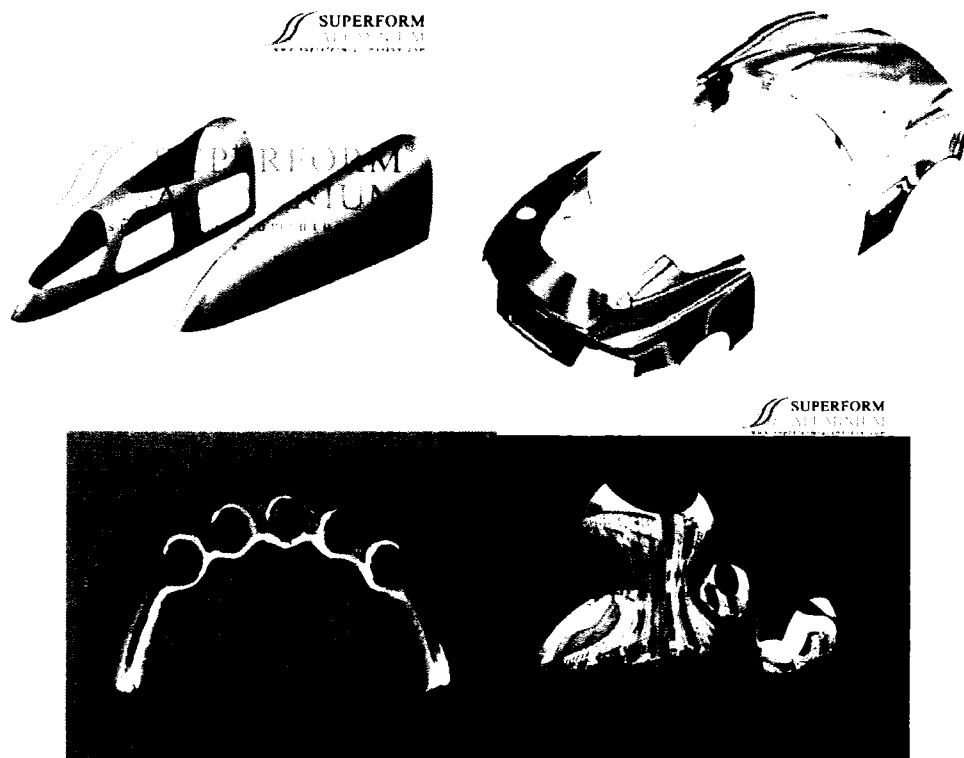


Figure 2- 3 SPF applications a) wing tip for the Boeing 777 [3], b) Aston Martin car panels [3] , c) dental implant superstructure [4] and d) art and architecture[3].

Recent observations have indicated that ultrafine-grain sheet metals have superior formability at relatively moderate temperatures. High strength accompanied by high ductility is possible with materials having fine and homogenous grain structures. Superplastic forming is an advanced technique which is being used to formed parts with such desirable properties. *Figure 2-4* explains how grain refinement enhances the superplastic behavior of superplastic material:

- It shifts the optimum strain rate to a higher value (higher production rate)
- It increases strain rate sensitivity index (more ductility, more homogenous deformation).
- It reduces optimum superplastic forming temperature (less energy, longer tool life).

The effect of grain size on the tensile ductility of 7475 Aluminum superplastic alloy is shown in *Figure 2-5*. There are different processing techniques that would produce a material with small grain size that satisfies the requirements of strength and ductility. However, the difficulty in producing ultrafine grain sheet metals hinders the widespread utilization of light weight alloys in the transportation industry.

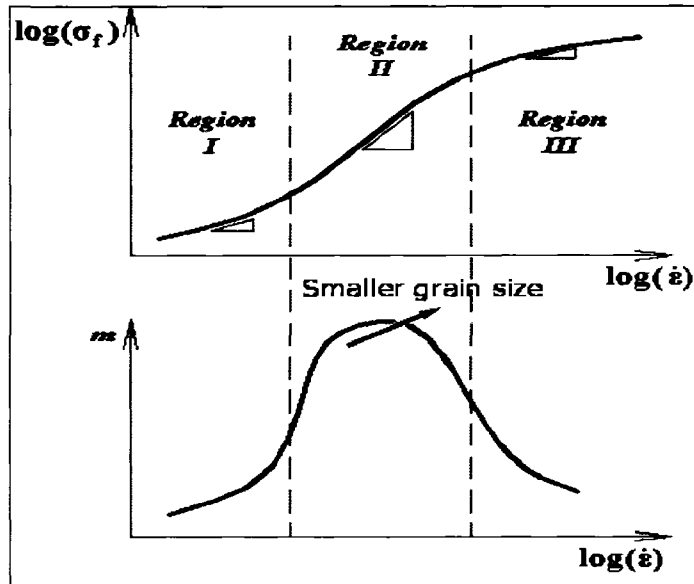


Figure 2- 4 Characteristic curve of superplastic material showing the effect of using fine grain structure.

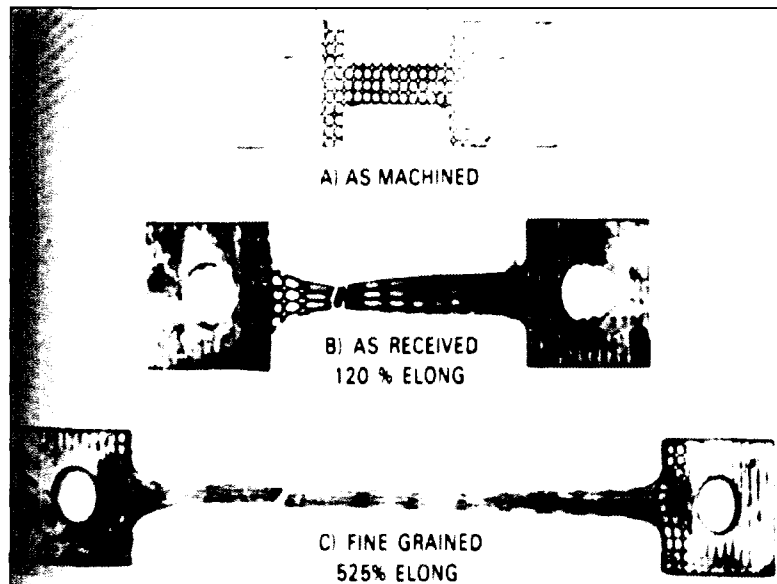


Figure 2- 5 The effect of grain size on the tensile ductility of 7475 Aluminum Superplastic alloy [5].

2.2 Grain Refinement

Conventional grain refinement techniques usually involve thermo-mechanical processing (e.g. hot rolling) which is costly, time consuming, and negatively affects the environment due to high energy consumption. Alternative effective grain refinement methods are very much needed.

Recently new advanced processing techniques have been used to effectively refine the grain structure. Equal channel angular extrusion (ECAE) is one of these advanced techniques but the fact that many passes (8-10 passes) are needed, in addition to the limited size of the billets and the high load required limited the wide spread utilization of this technique (*Figure 2-6* shows a schematic of the ECAE process). Another way of producing fine grain structure is the torsional strain severe plastic deformation (TS)-SePD (*Figure 2-7* shows a schematic of the (TS)-SePD process), but again this technique is very limited by the size of the processed sheet. Recently, a new process based on Friction Stir Welding (FSW) has been found to produce fine-grained microstructure. Friction Stir Processing (FSP) can be used to effectively produce ultrafine grain and homogenized structure.

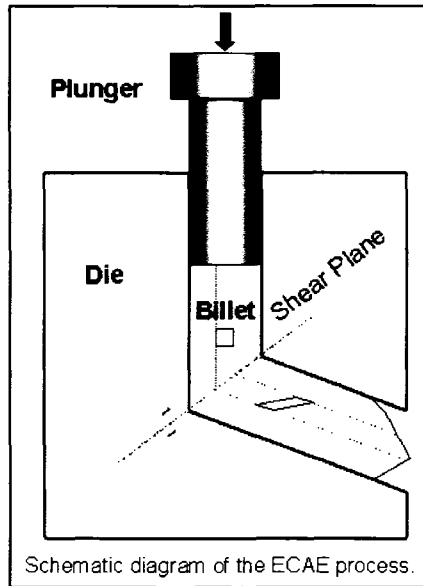


Figure 2- 6 Schematic of equal channel angular extrusion (ECAE) process [6].

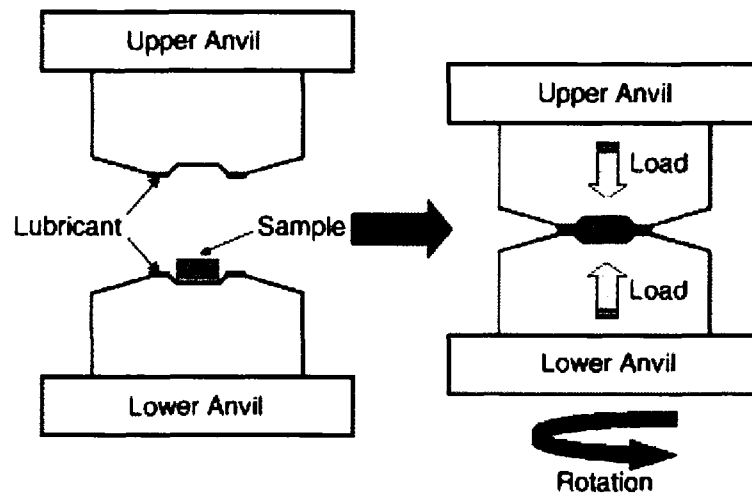


Figure 2- 7 Schematic of torsional strain severe plastic deformation ((TS)-SePD) process [7].

2.3 Friction Stir Processing (FSP)

Aluminum welding has always been a great challenge, which motivated the researchers at TWI to invent a new advanced welding technique; friction stir welding (FSW) [8]. Being a solid state joining process gives FSW a major advantage over other joining processes; by avoiding the creation of a molten pool which shrinks significantly on resolidification, the distortion after welding and the residual stresses are low. It was observed that the welding zone is characterized by equiaxed fine grain structure. As a result, the concept of FSW was extended to a new advanced microstructural modification process in the late 1990's; Friction Stir Processing (FSP). Since then, many researchers have investigated several aspects of the process. It has been reported that FSP can enhance the superplasticity of lightweight materials through producing an equiaxed ultrafine grain structure and favorably modifying the material properties [9-12].

During FSP, a specially-designed rotating tool which consists of a pin and a shoulder is used. The rotating pin is plunged into the sheet, traversing in the desired direction, while the shoulder is rubbing against the surface of the sheet generating enough heat (remains solid state) to soften the material beneath the tool. The mechanical stirring caused by the plunged rotating pin forces the softened material to undergo intense plastic deformation yielding a processed zone characterized by dynamically recrystallized fine grain structure. *Figure 2-8* shows a schematic of FSP.

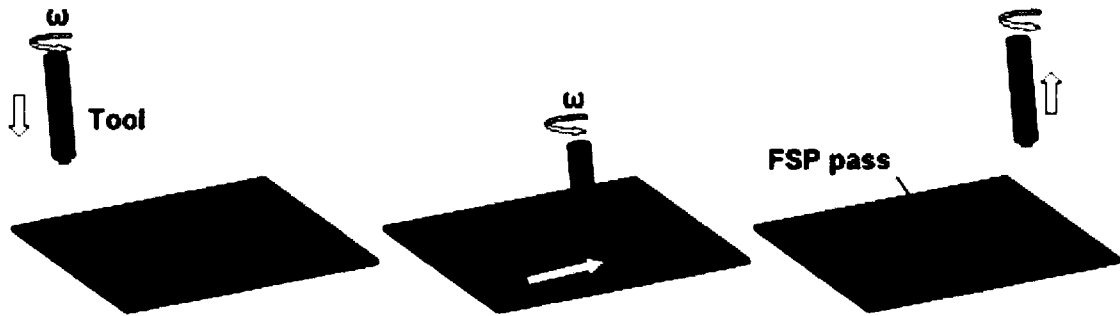


Figure 2- 8 Schematic of friction stir processing.

Friction stir processing offers many *advantages* over conventional and other newer material processing techniques.

- It is a single step process, while other techniques require multiple steps which make FSP easier and less time consuming.
- It uses a simple inexpensive tool.
- It can utilize a readily available machine such as a milling machine to conduct the process.
- It is suitable for automation.
- It is environmentally friendly since no gases or chemical are used.
- It is an energy efficient processes compare to other processing techniques since it does not need very high pressure or high amount

These features together make FSP easier, less expensive and so preferable over other processing techniques. However, there are some *limitations* that need to be addressed through extensive research.

- The lack of data correlating the various process parameters with the resulting microstructure.
- Very limited predictive models exist that can accurately describe the FSP process.

2.4 Previous Work

Friction stir processing (FSP) is believed to have a great potential in the field of superplasticity. The fine and homogenous grain structure produced by FSP makes this technique gain an impressive attention from the researchers in the *superplasticity* field. The effects of FSP on the superplastic behavior (through studying ductility, strain sensitivity and flow stress) were investigated for different materials and at different process parameters and at different tensile test conditions (temperature, strain rate etc...).

Dutta et al. [13] performed a deep cup forming by superplastic punch stretching of multiple overlapping passes of friction stir processed 7075 Al alloy plate at different strain rates. And they used FEM simulation to predict the load and thickness variations. The simulation results showed good prediction of the load as well as the thickness variations up to the beginning of instability. Mahony et al. [14] superplastically formed friction stir processed aluminum sheet. Their results suggested that FSP enhanced the superplasticity of the aluminum sheet through obtaining higher strain rate sensitivity

value at lower temperature and higher strain rate than the unprocessed material. Johannes and Mishra [15] attempted to create larger superplastic sheet by conduction multi passes of friction stir processing on 7075 Al sheet. They concluded that the multi passes FS processed sheets exhibited superplastic behavior, and that the primary mechanism of superplastic deformation of multi passes FS processed 7075Al is the boundary grain sliding. Cavaliere and Marco [16] investigated the superplastic behavior of FS processed AZ91 magnesium alloy. Different temperature and strain rate values were used and the results showed that an increase of elongation and strain rate sensitivity value were achieved through FSP. Ma et al. [17] investigated friction stir processing of commercial 7075 Al rolled plates with different processing parameters. They observed that heat treating the FS processed sheets at 490 °C for an hour showed that the fine grain microstructures were stable at high temperatures. Superplastic investigations in the temperature range of 420–530 °C and strain rate range of 1×10^{-3} – 1×10^{-1} s⁻¹ were carried out and they demonstrated that a decrease in grain size resulted in significantly enhanced superplasticity and a shift to higher optimum strain rate and lower optimum deformation temperature. Salem et al. [18] studied the ability of friction stir welded 2095 sheet to maintain superplastic behavior in the weld region. They stated that higher welding rates result in higher % elongation to fracture. High welding rates increased the density of dislocations and developed microstructures consisting of tangled dislocation structures and sub-grains with small misorientations. It was observed that necking took place within the region adjacent to the friction stir weld nugget, followed by fracture. Johannes et al. [19] investigated the effects of FSP on the superplastic behavior of continuous cast AA5083 aluminum. The results showed that compared to the as-cast

samples the FS processed samples exhibited 2-3 times more elongation, and that the flow stress for the FS processed sample was lower than that for the as-cast samples. Mishra et al. [20] investigated the effects of overlapping passes of FSP on superplastic behaviors of 7075 aluminum alloy sheets. They used a constant velocity punch forming tests to study the effect of strain rate on forming. Tensile tests were performed for several samples taken from various areas of the FSP sheet. Their results showed that the as received sample did not exhibit superplastic behavior however the overlapped FSP exhibited superplastic behavior. Ma et al. [11] investigated the superplasticity in friction stir processed cast A356 aluminium alloy. They conducted single pass FSP at different temperatures and strain-rates. Mini tensile samples were tested. And they concluded that FSP converted a non-superplastic cast A356 to superplastic. Charit et al. [21] investigated the effect of FSP on the superplasticity of 2024 aluminum alloy. They concluded that superplasticity is achieved in 2024 alloy at a higher strain rate and lower temperature via friction stir processing. They suggested that FSP of commercial 2024 aluminum alloy is a simple and effective technique that can produce microstructure suitable for superplasticity at high strain-rates, lower temperature and lower flow stress.

Studies on the effects of FSP on *microstructure and mechanical properties* have been targeted by many researchers in the FSP field. Different techniques have been used to investigate the microstructure of the FSW or FSP material such as such as optical microscopy, Transmission Electron Microscopy (TEM), Scanning Electron Microscopy (SEM), and Orientation Imaging microscopy (OIM). Different mechanical tests have been conducted such as hardness tests, tensile tests, fatigue tests etc... In terms of the

material of interest; most of the researches focused on aluminium alloy while some have done some work on steel, titanium, copper and magnesium [22-35]. For example; Itharaju and Khraisheh [25] investigated the effect of process parameters of FSP of 5052 aluminum alloys. Mishra et al [11, 13, 17, 20, and 21] showed that FSP of different aluminum alloys; 7075, 2024 and cast A356 produces finer grain structure. Sutton et al [26] used scanning electron microscope (SEM) and energy dispersive X-ray spectroscopy (EDX) to analyze the microstructure and chemical compositions of the material. **Chapter Four** includes more detailed literature review about investigations of microstructure and the mechanical properties of FS processed materials.

The fact that **thermal** aspects are very critical to control the process motivated many scientists to conduct researches which focused on the thermal aspects of FSP. Some of them took the experimental path to measure the thermal fields cooling and heating curves and etc. Others focused on thermal modeling of the process, they used different approaches and methodologies: analytical, computational fluid dynamic, finite element simulation and etc. For example; Lambarkos et al. [36] used the inverse problem approach to generate the thermal profiles during FSW using thermocouple measurements. Askari et al. [37] developed a three dimensional analysis scheme to predict the temperature fields and used thermocouples to validate the model. Song et al. [38] used an explicit central differential scheme, to calculate the heat transfer during the tool penetration, welding, and removal. More literature review about the thermal aspects of the process can be found in **Chapter Five**.

In terms of *modeling*, most of the works that have been done were focused on thermal modeling of the process [36-42]; some attempts have been done to develop a mechanical or thermomechanical model. But there are limited numbers of work that have attempted to connect thermomechanical model with the microstructure. And still there is a great need for a comprehensive and accurate model to predict the resulting microstructure from the process parameter. Some of the previous works that have been done in modeling field are briefly discussed in the following paragraph. Ulysse [43] proposed a 3-D viscoplastic model for friction stir welding to determine the effect of tool speed on temperature. Chang et al. [44] attempted to develop a relation between grain size and Zener-Holloman parameter for friction stir processed AZ31 Mg alloy. Heurtier et al. [45] proposed a thermomechanical analysis of FSW, in which a model for material flow pattern was proposed. They divided the weld zone into two and used classical fluid mechanics to determine the velocity fields assuming incompressible and kinematically-admissible flow. Schmidt et al. [46] proposed an analytical model for heat generation in friction stir welding and studied different contact conditions between the tool and the weld; sliding, sticking and partial sliding/sticking. Arbegast [47] proposed a simple model based on metalworking processes and presented relationships to calculate the extrusion zone width, strain rate and pressure. Schneider et al. [48] described in their mathematical model the material flow path in friction stir welds and proposed three incompressible flow fields that together describe the material flow in friction stir welds. Nandan et al [49] solved the equations of conservation of mass, momentum and energy numerically and computed the spatial variation of the non-Newtonian viscosity. Buffa et al. [50] used a Finite Element model, which was calibrated experimentally, to investigate

the temperature and strain distributions. Fratini et al. [51] proposed a numerical model that aimed at the determination of the average grain size due to continuous dynamic recrystallization phenomena in friction stir welding of AA6082 T6 aluminum alloy. See *Chapter Six: Analytical Mechanical Model*, for more detailed literature review of the previous modeling works that had been done in the FSP and FSW fields.

Chapter Three

EXPERIMENTAL SETUP

3. EXPERIMENTAL SETUP

In this chapter all of the following are discussed; the material used, the experimental setup and the basic equipment required to conduct FSP, the tool designs, the experimental procedures and the process parameters used to conduct FSP.

3.1 Material

Different materials have been investigated in this work. Commercial aluminium alloy 5052 in the form of 3.22 mm thick sheet has been investigated via FSP, the nominal composition of AA5052 (weight percentage) is shown in Table 3-1. The motivations for choosing AA5052 are: it is a commercially available alloy that has a potential in automotive and aerospace industries, it is found to exhibit superplastic behavior at certain conditions and by refining the grain structure which is believed to enhance its superplastic behavior.

Table 3- 1 composition of AA5052 alloy [52]

| Component | Wt. % | Component | Wt. % | Component | Wt. % |
|-----------|-------------|-------------|-----------|--------------|----------|
| Al | 95.7 - 97.7 | Mg | 2.2 - 2.8 | Other, total | Max 0.15 |
| Cr | 0.15 - 0.35 | Mn | Max 0.1 | Si | Max 0.25 |
| Cu | Max 0.1 | Other, each | Max 0.05 | Zn | Max 0.1 |
| Fe | Max 0.4 | | | | |

Another important material that has been investigated is magnesium. Magnesium offers a great potential for weight reduction by replacing steel and aluminum, if proper design considerations are made. Until now most of the successfully produced magnesium parts are cast-components, however significant weight reduction cannot be achieved unless magnesium usage is expanded to cover other areas, mainly sheet metal forming. The metal's inferior ductility at room temperature still hinders its widespread uses. Magnesium alloy AZ31 is commercially available in sheet form, and offers good mechanical properties. Unfortunately, the alloy exhibits very limited ductility accompanied by brittle-like behavior at room temperature. Recent results however indicated that it is possible to form AZ31 sheets at elevated temperatures under certain conditions, and even achieve superplastic-like behavior [53, 54]. The results also suggest that improved ductility and formability can be achieved by refining and homogenizing the grain structure of the sheet. In this work commercial magnesium alloy AZ31B in the form of 3.22 mm thick sheets with different heat treatment conditions (H24 and O-temper) have been investigated. The nominal composition of the Magnesium AZ31B alloy (weight percentage) is shown in Table 3-2.

Table 3- 2 composition of Mg AZ31 alloy [52]

| Component | Wt. % | Component | Wt. % | Component | Wt. % |
|-----------|-----------|-----------|-----------|-----------|-----------|
| Al | 2.5 - 3.5 | Fe | Max 0.005 | Ni | Max 0.005 |
| Ca | Max 0.04 | Mg | 97 | Si | Max 0.1 |
| Cu | Max 0.05 | Mn | Min 0.2 | Zn | 0.6 - 1.4 |

3.2 Tools and Equipments

One of the great advantages of FSP are; available machines such as a milling machine can be used to conduct the experiments, and simple and inexpensive FSP tool can be used to conduct the process.

The FSP tool is a very critical aspect which highly affects and controls the process. Both tool's geometry and material have to be carefully selected to successfully FSP different materials and thicknesses. The tool assembly consists of a shoulder and concentric pin. The tools which are used in this work are made of H13 tool steel. Different tool configurations were used; shoulder diameter of $\frac{1}{2}$ " and $\frac{3}{4}$ ", and shoulder with and without concavity are used. The pin diameter is $\frac{1}{4}$ " and the height of it is slightly shorter than the thickness of the sheet which is $\frac{1}{8}$ ". Threaded and non-threaded pin are used. *Figure 3-1* shows the different FSP tool configurations that have been used.

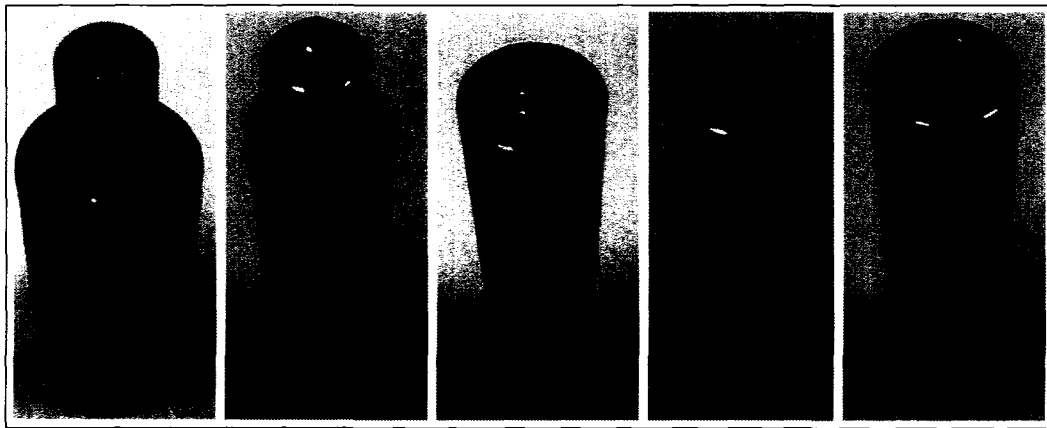


Figure 3- 1 Different FSP tool configurations [55].

To conduct FSP, HAAS VF-0F CNC vertical milling machine (shown in *Figure 3-2*) have been used. Different backing plates, holding fixture have been designed and

used through out this work. Different setups have been used for: simple single pass setup, multi passes setup, rigid setup that can adapt to different sheet thickness and higher loads and also its base is equipped with cooling system to apply different cooling conditions. These setups are illustrated in *Figures 3-3 to 3-5*.

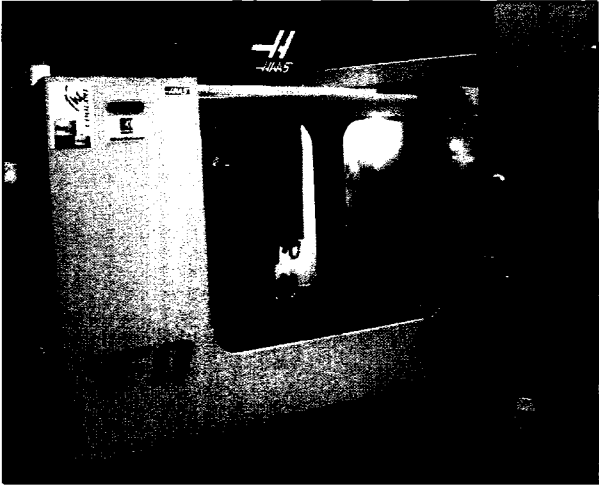


Figure 3- 2 HAAS VF-0F CNC vertical milling machine.

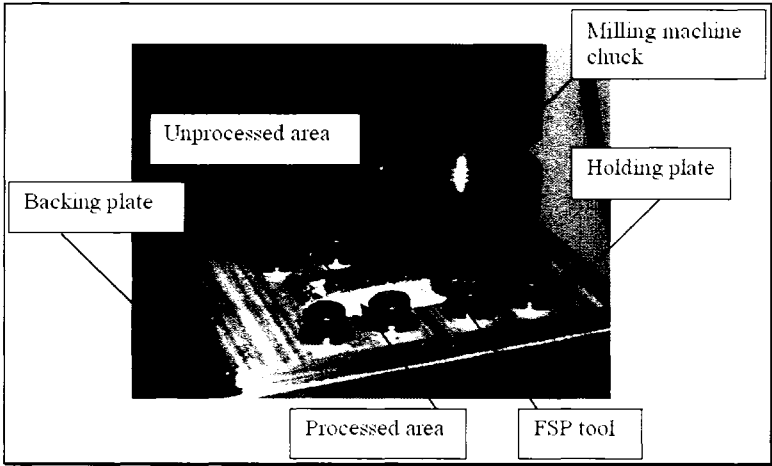


Figure 3- 3 Single pass setup[55].

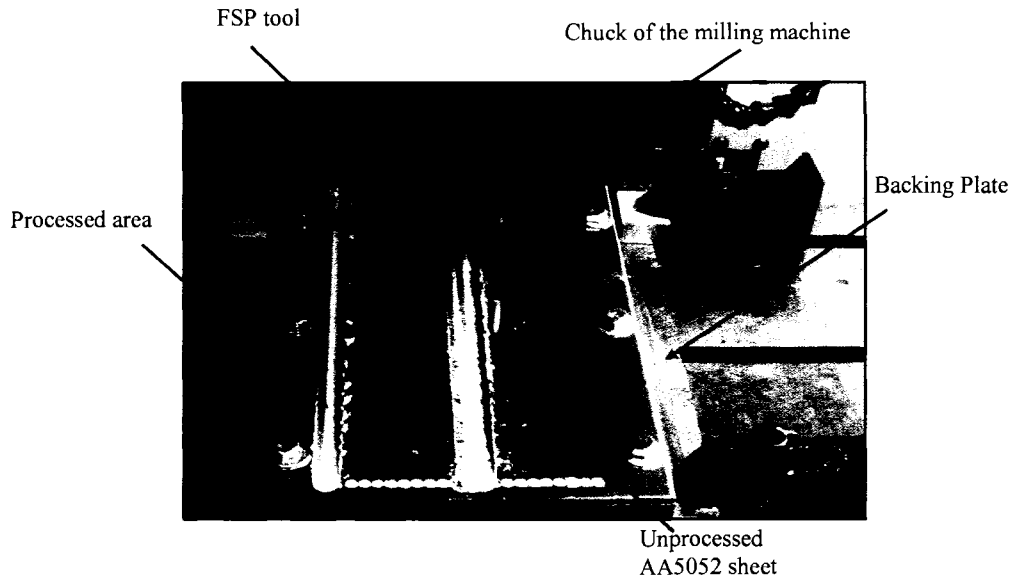


Figure 3- 4 Multi passes setup.

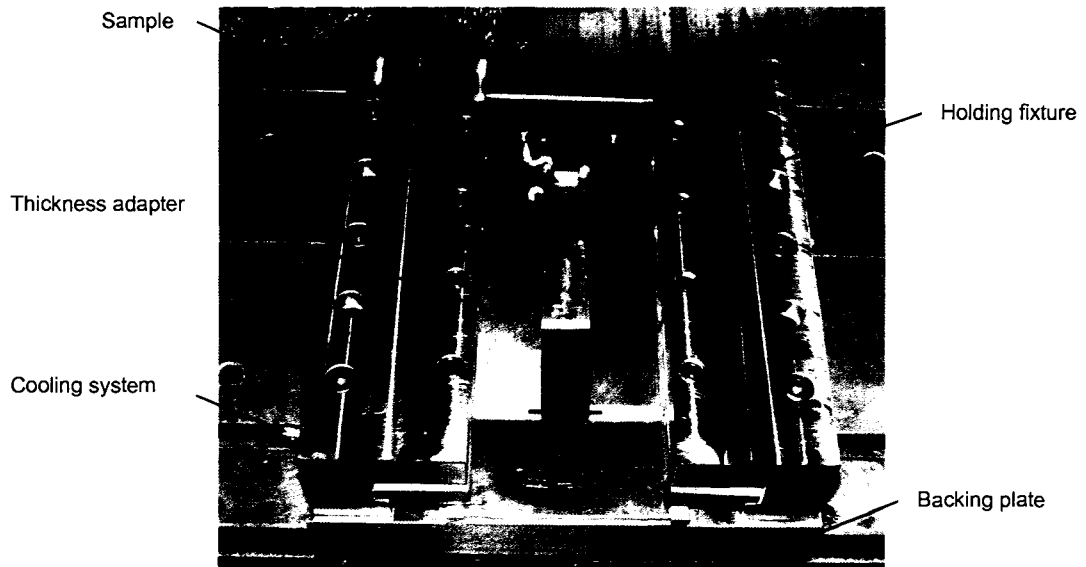


Figure 3- 5 Different sheet thicknesses and higher load setup which is equipped with a cooling system.

3.3 Experimental Procedures

The sample that needs to be friction stir processed has to be clamped firmly before the processing starts, and has to be fixed and stable during the processing. Then a small hole with a diameter that equals the pin diameter is drilled, instead of using the pin of the tool to start penetrating the workpiece, this drilled hole avoid the significantly unnecessary loading on the tool for penetrating. Then the pin of the FSP tool is forced into the workpiece while it is rotating at the desired rotational speed, and the shoulder becomes in contact with the surface of the workpiece. The rotating FSP tool is then transverses along the desired direction with specific translational speed. The simple procedures are illustrated in *Figure 3-6*.

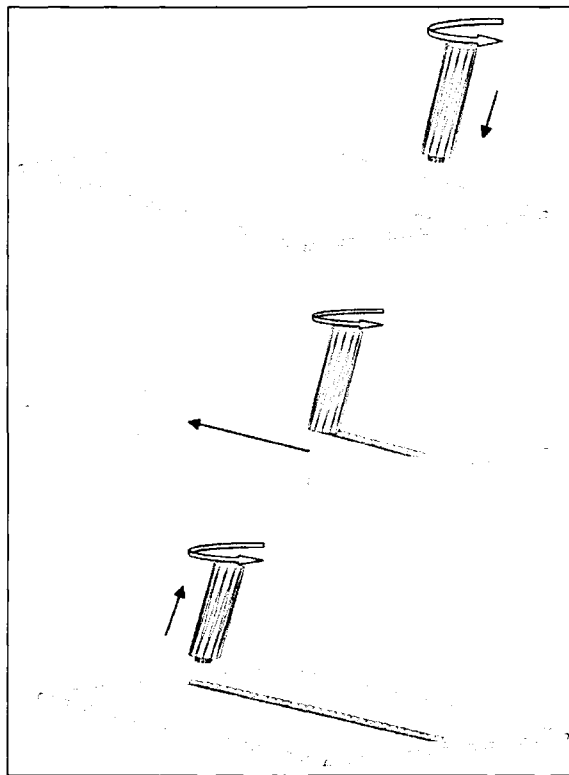


Figure 3- 6 Schematics of the stages of friction stir processing (FSP)[55].

3.4 Process Parameters

Choosing the suitable process parameters (rotational and translational speeds) that can successfully FSP a certain material is very important. Usually for aluminum alloys, rotational speeds of 300-800 rpm and translational speeds of 1.0-3.0 in. /min. are used. To conduct FSP on AA5052 sheets combinations of 400-1000 rpm and 1.0-3.0 in/min have been used in this work. It is found, however, that these conditions do not work for magnesium alloys. The rotational and translational speeds that have been used for FSP of AZ31 Mg alloys are different than those used for Aluminum alloy. For FSP of magnesium alloys, higher rotational speed and much higher translational speed have to be used. Several samples were FS processed at different combinations of rotational (1000-2500 rpm) and translational (8.0-30.0 in/min.) speeds. *Figure 3-7 to 3-11* show some successfully FS processed and other defective samples which were processed using different tool geometries. Table 3-3 summarizes the rotational and translational speeds used for FSP the different materials.

Table 3- 3 Rotational and translational speeds used for FSP different materials

| Material | Rotational Speed (rpm) | Translational speed (in/min.) |
|--------------|------------------------|-------------------------------|
| AA5052 | 400-1000 | 1.0-3.0 |
| Mg AZ31B-H24 | 1200-2000 | 20.0-30.0 |
| Mg AZ31B-O | 1000-2500 | 8.0-20.0 |

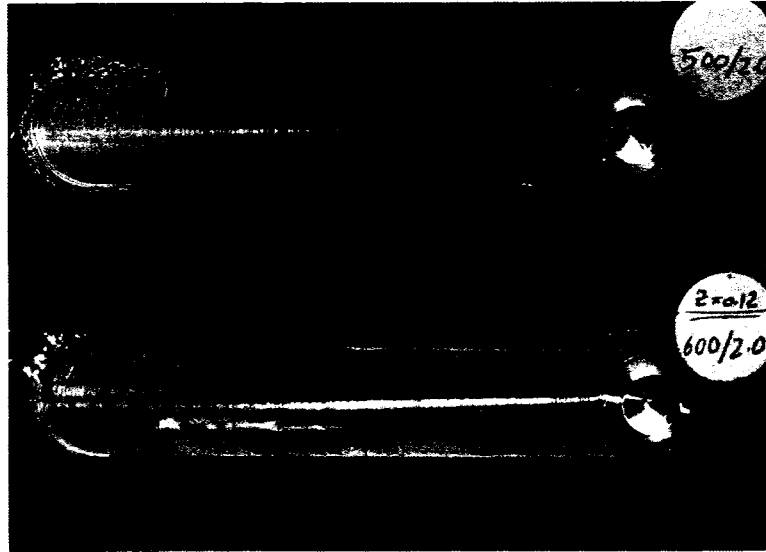


Figure 3- 7 Successfully FS processed AA5052 samples at a) 500 rpm and 2.0 in. /min. and b) 600 rpm and 2.0 in. /min. (Tool is 0.5" shoulder diameter, flat pin and flat shoulder).



Figure 3- 8 Defective FS processed Mg AZ31 samples, processed at typical Aluminum alloys FSP conditions. a) 800 rpm and 2.0 in. /min. and b) 400 rpm and 2.0 in. /min. (Tool is 0.5" shoulder diameter, flat pin and flat shoulder).

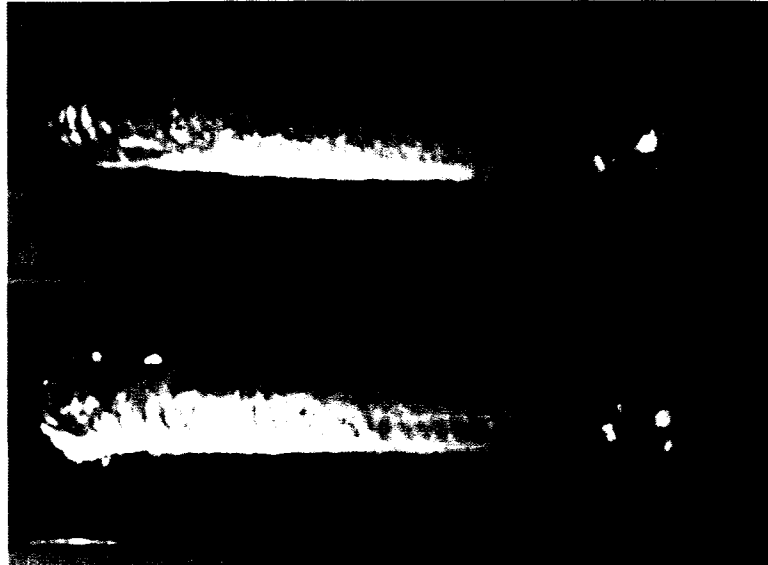


Figure 3- 9 Successfully FS processed Mg AZ31B-H24 samples at a) 1200 rpm and 22 in. /min. And b) 1200 rpm and 25 in. /min. (Tool is 0.5" shoulder diameter, flat pin and flat shoulder).

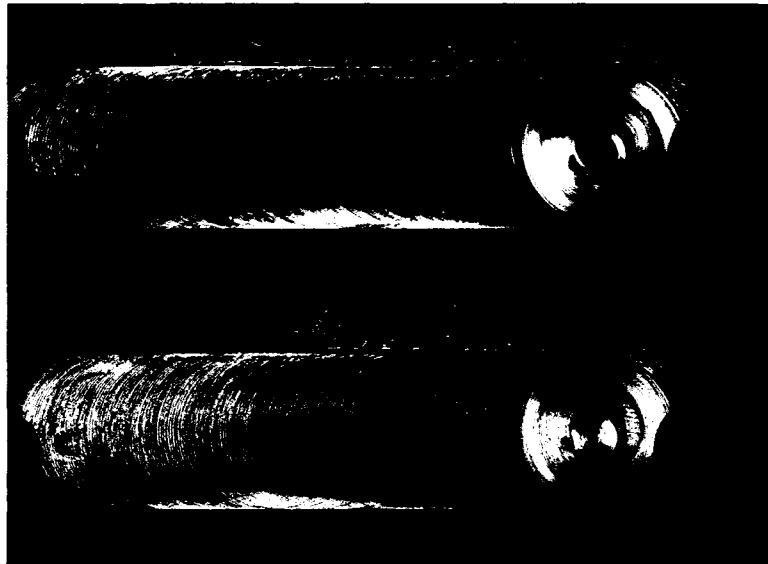


Figure 3- 10 Mg AZ31B-H24 samples processed at a) 1200 rpm and 15.0 in. /min., and b) 1500 rpm and 18.0 in. /min. (Tool is 0.75" shoulder diameter, flat pin and concave shoulder).

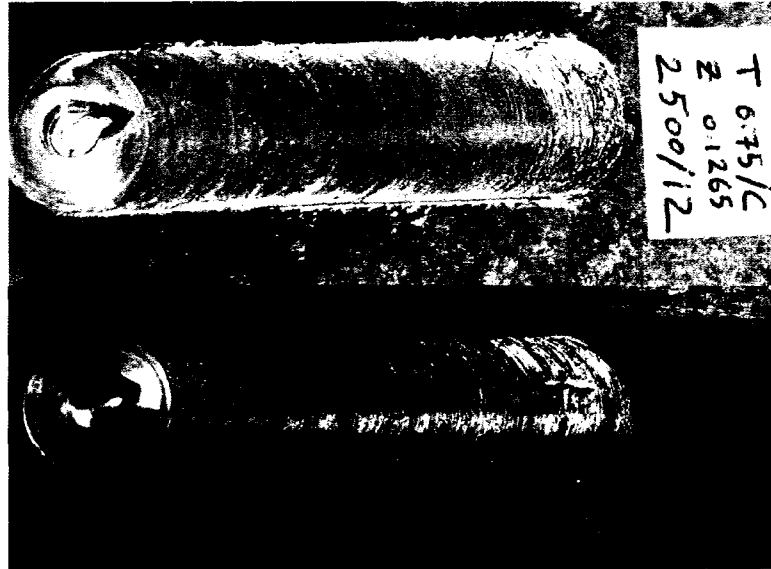


Figure 3- 11 Mg AZ31B-O samples processed at a) 2500 rpm and 12.0 in. /min., and b) 1750 rpm and 12.0 in. /min. (Tool is 0.75" shoulder diameter, flat pin and concave shoulder).

Chapter Four

MICROSTRUCTURE AND HARDNESS CHARACTERIZATION

4. MICROSTRUCTURE AND HARDNESS CHARACTERIZATION

This Chapter focuses on the microstructure and hardness characterization of the FS processed area. The chapter discusses the previous works that have been done in these fields. Then the experimental setups used and the procedures followed to conduct microstructural and hardness investigations are presented. Microstructural and hardness results for magnesium AZ31 are discussed. And finally the chapter is concluded with the concluding remarks.

4.1 Previous Work

Many researchers used different techniques and methodologies to investigate the effect of FSP on the microstructure and mechanical properties of the processed material. In this section some of the work which had been done in this field is discussed.

Su et al. [56] used optical, transmission electron and orientation image microscopy to investigate grain refinement obtained by FSP of AA7075 associated with rapid cooling. Their results showed that small grains of 100-500 nm can be obtained using such technique. In their work, Scialpi et al. [57] investigated the effect of tool geometry on the microstructure and mechanical properties of AA6082. They noticed small influence of the shoulder geometry on the resulting microstructure, and as the shoulder contact surface decreased more grain refinement was obtained, this due to different heat generated from different shoulder geometry. Kang et al. [58] studied the

effect of FSP without a stirring pin on the microstructure and consequently the formability of Al alloy sheet. Su et al. [10] studied the resulting microstructure of friction stir processed commercial 7075 Al alloy. The grain structure of FS processed area was examined by TEM. Su et al. observed that the microstructure of FS processed area did not have a uniform grain size distribution. The average grain size slightly decreases from top to bottom. Also diffraction rings were observed, which according to them confirm that there are large misorientations between the individual grains. Generally the dislocation density was not uniform within the stir zone even with similar grain size; this observation suggested that non-uniform plastic deformation was introduced in the recrystallized grains during FSP. Sutton et al. [25] studied the microstructure of friction stir welds in 2024-T3 aluminum. Optical microscope and scanning electron microscope (SEM) were used to capture the microstructure. Their results showed that more grain refinement occurred within the nugget, and that grain size decreased as traveled from top to bottom, most likely due to higher heat input on the top causing additional grain growth. The results from metallurgical, hardness and quantitative EDX measurements showed that FSW can create a segregated banded microstructure consisting of alternating hard particle-rich and hard particle-poor regions. Peel et al. [59] in their work on FSW of AA5083 presented microstructural, mechanical properties and residual stresses results. They suggested that heat input is more dominant than the mechanical deformation on the resulting mechanical properties of the FS welds. Jata et al. [22] used optical and TEM microscopy to examine the microstructures of friction stir welds of Al-Li alloy and they establish the mechanism of the evolution of microstructure in the dynamically recrystallized region of FSW welds. Their results showed that many of the grain

boundary misorientations created in the dynamically recrystallized region were observed to be between 15° to 35° , which means; the recrystallized grains in that region are caused by continuous dynamic recrystallization mechanism. Itharaju and Khraisheh [25] studied the effect of rotational and translational speeds on the microstructure and the generated forces in FS processed AA5052 sheets. They observed significant grain refinement; the resulting average grain sizes attained were between 1.5 and 3.5 μm compared to 37.5 μm for the as-received material. They also concluded that, in general, that as the rotational speed increases the plunging force increases and it is almost independent of the translational speed. Bensavides et al. [60] investigated the microstructures of Al 2024 friction stir welds and compared the grain size of friction stir welding at room temperature and at low temperature (-30°C). Their results showed that there was an increase in the weld zone equiaxed grain size from bottom to top at room temperature, but at low temperature there is a smaller difference. Furthermore, the grain size is considerably smaller in the low-temperature weld. Kwon et al. [61] investigated the hardness and tensile strength of the friction stir-processed AA1050. They observed that the hardness and tensile strength increased significantly with decreased tool rotation speed.

Cavaliere and Marco [62] investigated the microstructure and mechanical properties of AM60B magnesium alloy. Their results showed that FSP leads to grain refinement in AM60B magnesium alloy, and that hardness dropped dramatically in the heat affected zone. Hung et al. [63] studied the effect of FSP on the microstructure and mechanical properties of AZ31 Mg alloy. They showed in their work that finer grains were obtained at lower rotational speeds. Santella et al. [27] investigated the effects of

FSP on the mechanical properties of cast aluminum alloys A319 and A356, they showed that in contrast to the as-cast conditions, microstructures within the stir zones were relatively uniform. The porosity and dendritic microstructures were also eliminated. Microhardness distributions were more uniform. The ultimate tensile strength, ductility, and fatigue life were increased by friction stir processing. Chang et al. [64] in their work noticed that grain size between 100-300 nm when FSP Mg-Al-Zn alloy with controlled thermal history, and that such ultrafine grain structure can significantly increase the microhardness. Mahoney et al. [24] investigated the microstructure of friction stir processed NiAl Bronze alloy, they reported the initial microstructural evolution and resultant mechanical properties for the variety of the microstructures created by FSP, which include Widmanstätten, equiaxed fine grains and banded or lamellar structure. The results reported by them showed that all the FSP microstructures have significantly superior mechanical properties compared to the as-cast microstructure. The reason for this is that FSP eliminates casting defects and causes significant refinement of the microstructure.

In general; most of the researchers focused on investigating the microstructure and mechanical properties of FS processed aluminum alloys. Other light weight alloys such as magnesium alloys need more studies to systematically investigate the effect of various process parameters on the resulting microstructure and mechanical properties. There is still no clear correlation that can accurately relate the resulting microstructure to the process parameters. In this chapter, microstructure and hardness investigations of FS

processed AZ31B Mg alloy with different heat treatment conditions have been conducted. The results are also compared with those for AA5052.

4.2 Experimental Setup and Procedures

Optical microscopy is used to capture the microstructure of the as-received and FS processed magnesium samples. Various samples, FS processed at different combinations of rotational and translational speeds at different traverse and longitudinal positions, have been investigated. The sample preparation for the microscopic investigation includes cutting, mounting, grinding and polishing. All microstructural samples were taken from the transverse section of the processed area at the middle of the sheet thickness as shown in *Figure 4-1*.

For the AA5052 samples; the microstructural investigations are done in collaboration with the Department of Mechanical Engineering, Florida State University (FAMU-FSU) using Orientation Imaging Microscopy (OIM). (More details about the microstructural investigations of AA5052 sheets can be found in the author's Master Thesis [55]).

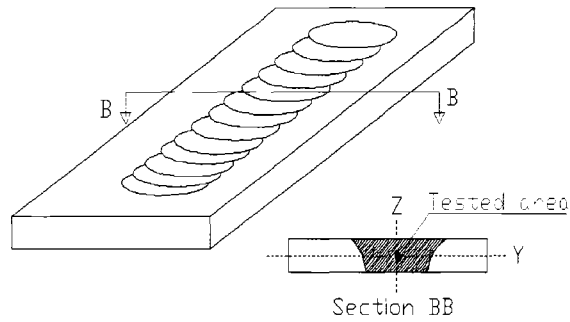


Figure 4- 1 Schematic shows the tested area within the FS processed area.

Vickers microhardness tester is used to measure the Vickers microhardness values of friction stir processed samples. The test load applied was 200 gf, and the dwell time was 5 seconds. Various samples FS processed at different rotational and translational speed were tested at different traverse and longitudinal positions. The average of five values of hardness within each tested area was considered. All samples were taken from the transverse section of the processed area at the middle of the sheet thickness; the same as the samples for microstructural investigation (see *Figure 1*). Same setup, procedures and conditions are used for both aluminum and magnesium samples.

4.3 Microstructure

The microstructural investigations presented in this work include; grain size distribution through the thickness of the processed sheet as well as along the FS

processed pass at different process parameters. The effects of rotational speed, translational speed, temperature, and tool geometry are also investigated.

The microstructural results of FS processed AZ31B-H24 Mg sheets show some grain refinement; but more important, FSP produced a more homogenous microstructure. *Figure 4-2* shows the grain structure of the as-received material and FS processed samples, at 1200 rpm rotational speed and 22 & 25 in/min. translational speeds, respectively. The as-received sheet has a fine microstructure with an average grain size of about 6 microns. It is observed that although there is not significant grain refinement after FSP, the grain structure is clearly more equiaxed and homogeneous. It is clearly illustrated that FSP refined the microstructure from an average grain size of about 6 microns to an average grain size of about 4 microns. More important, the distribution of grain size is clearly shifted and concentrated to the left indicating more refinement and more homogenous equiaxed structure. The as-received structure exhibits a combination of large and small grains while the structure of the processed samples show that the majority of grains have almost the same grain size. The finer and more homogenous grain structure produced by FSP is expected to improve ductility and formability of the material at elevated temperatures, and improve its superplastic behavior.

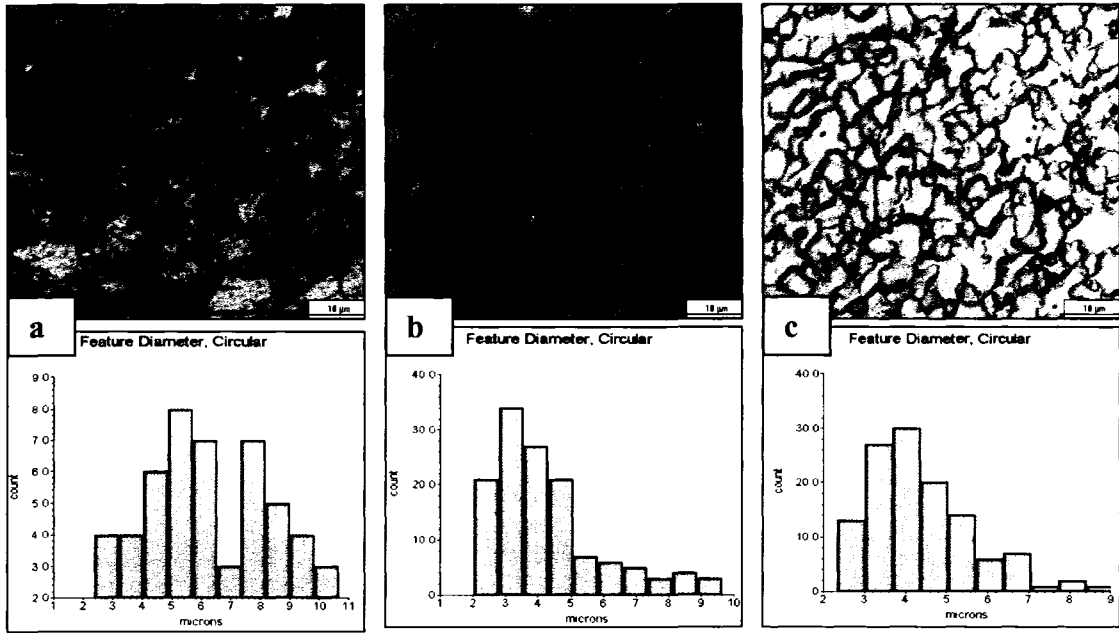


Figure 4- 2 Microstructure of AZ31B-H24 Mg a) as-received, b) FS processed sample at 1200 rpm and 22 in. /min., and c) FS processed sample at 1200 rpm and 25 in. /min.

Since the as-received AZ31B-H24 Mg sheet is considered to be relatively fine-grained, and in order to quantify the grain refinement achieved with FSP; AZ31B-O Mg alloy sheet, with a coarser as-received average grain size of 8.9 μm , has been FS processed using different process parameters. The results show again that significant grain refinement can be achieved using FSP (average grain size as small as 4.7 μm is achieved). Figures 4-3 to 4-10 show the microstructure of the FS processed samples, and Table 4-1 summarizes the average grain sizes for each condition.

Figure 4-11 shows the effect of rotational speed on the resulting grain size. It is clearly shown that as the rotational speed decreases, the resulting grain size decreases; which agree with what was observed by other researchers for magnesium and even other

materials. This is believed to be related to the thermal histories associated with the process at different rotational speeds; more heat is generated at higher rotational speed and so more grain growth is taking place (more details can be found in *Chapter Five*). *Figure 4-12* shows the effect of translational speed, and again the trend is clear; as the translational speed increases smaller grain size can be achieved. And this is again explained by the fact that at lower translational speed the processed sheet is exposed to the heat source for longer time, which gives more time and higher temperature for the grain to grow.

Interestingly, it is also observed that at certain conditions (high rotational and low translational speeds), grain size is even larger than that for the as-received material. This suggests that controlling the process parameters can dramatically change the resulting properties, and it can even reverse the process from a grain refinement process to a grain coarsening process.

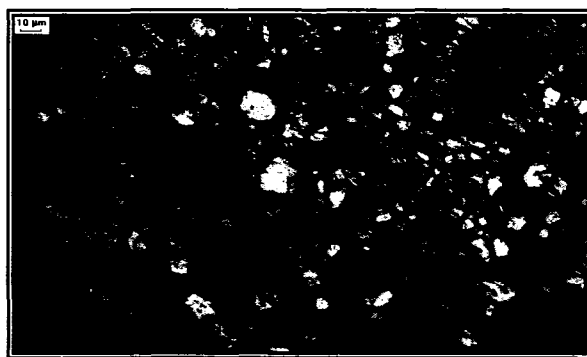


Figure 4- 3 Microstructure of an as-received Mg AZ31B-O sample (Average grain size is 8.9 μm).

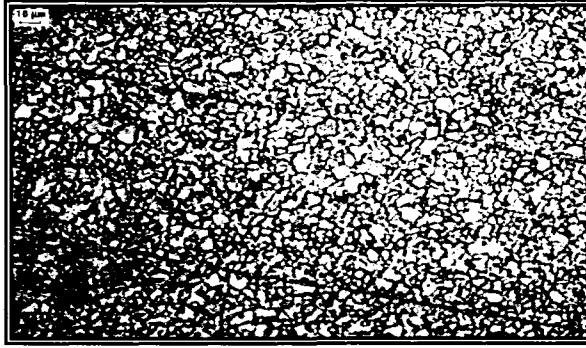


Figure 4- 4 Microstructure of Mg AZ31B-O sample FS processed at 1000 rpm and 12 in/min (Average grain size is 5.2 μm).



Figure 4- 5 Microstructure of Mg AZ31B-O sample FS processed at 1200 rpm and 12 in/min (Average grain size is 6.1 μm).

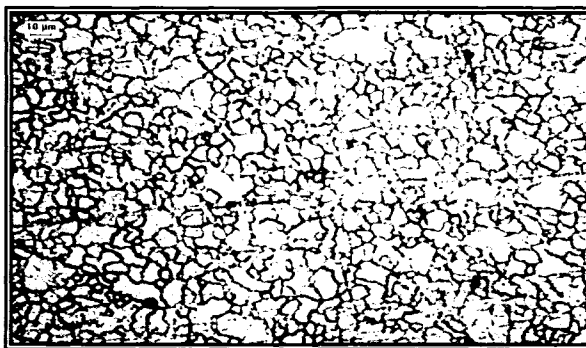


Figure 4- 6 Microstructure of Mg AZ31B-O sample FS processed at 1750 rpm and 12 in/min (Average grain size is 8.1 μm).



Figure 4- 7 Microstructure of Mg AZ31B-O sample FS processed at 2500 rpm and 12 in/min (Average grain size is 14.4 μm).

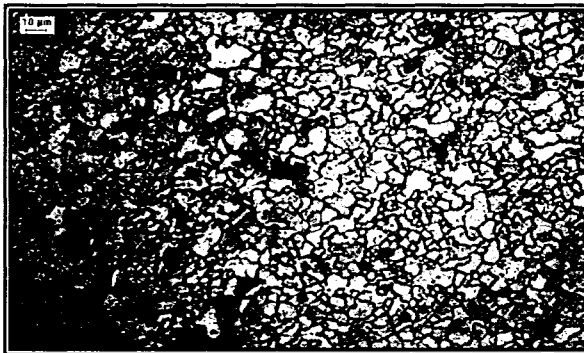


Figure 4- 8 Microstructure of Mg AZ31B-O sample FS processed at 1200 rpm and 8 in/min (Average grain size is 5.8 μm).



Figure 4- 9 Microstructure of Mg AZ31B-O sample FS processed at 1200 rpm and 15 in/min (Average grain size is 5.4 μm).

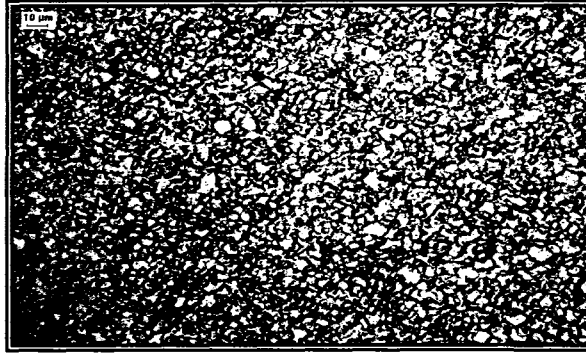


Figure 4- 10 Microstructure of Mg AZ31B-O sample FS processed at 1200 rpm and 20 in/min (Average grain size is 4.7 μm).

Table 4- 1 Average grain size for Mg AZ31B-O alloy, as-received and FS processed samples

| Sample | | Average grain size (μm) |
|-----------------|--------|-------------------------|
| As-received | | 8.9 |
| FS processed at | | |
| rpm | in/min | |
| 1000 | 12 | 5.2 |
| 1200 | 12 | 6.1 |
| 1750 | 12 | 8.1 |
| 2500 | 12 | 14.4 |
| 1200 | 8 | 5.8 |
| 1200 | 15 | 5.4 |
| 1200 | 20 | 4.7 |

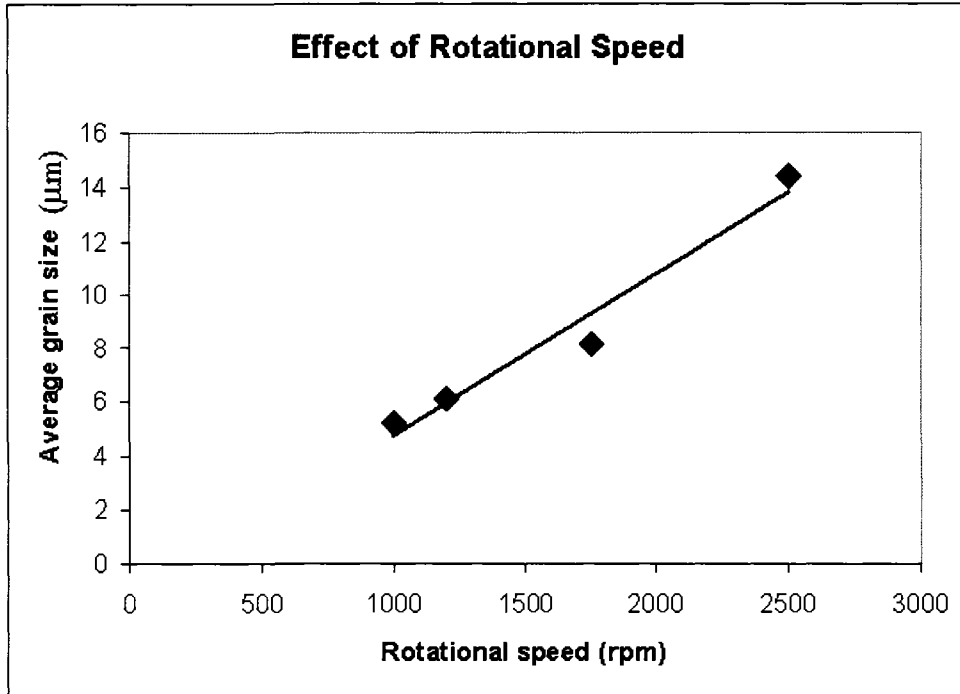


Figure 4- 11 Effect of rotational speed on the resulting grain size of FS processed Mg AZ31B-O sample (translational speed is 12 in/min).

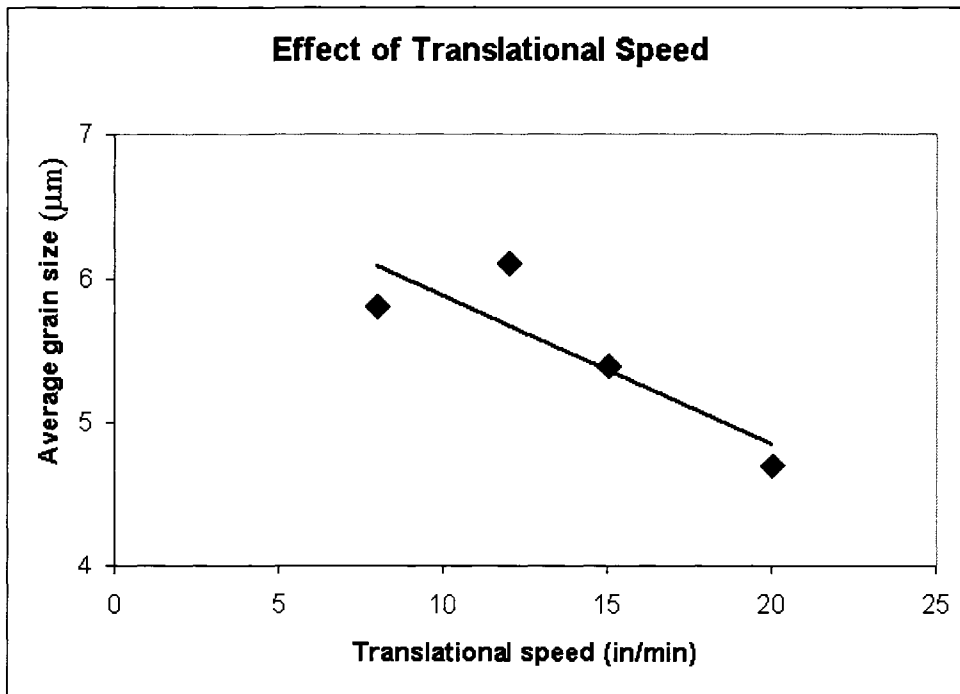


Figure 4- 12 Effect of translational speed on the resulting grain size of FS processed Mg AZ31B-O samples (rotational speed is 1200 rpm).

For the sake of material comparison; some of the microstructural results for FS processed AA5052 which was included in the author's master thesis are shown in this work. The trends and observations which are noticed for the AZ31 magnesium alloy are similar to those for the AA5052 alloys; see for example *Figures 4-13 and 4-14*. (For more details about microstructural investigations of AA5052 see author's master thesis [55]).

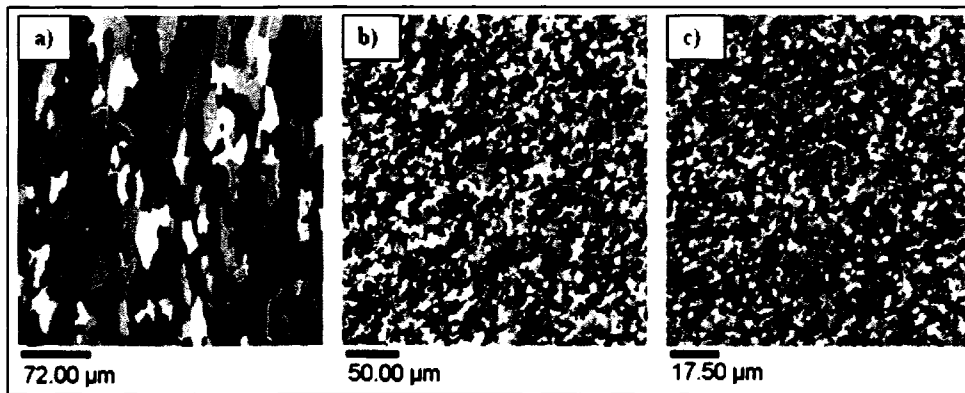


Figure 4- 13 OIM maps for the grain structure of AA5052 sheet; as-received (13.4 μm), b) FSP @ 1000 rpm and 2.5 in/min (4.5 μm) and c) FSP @ 600 rpm and 2.5 in/min (1.7 μm) (In collaboration with Department of Mechanical Engineering, FAMU-FSU) [12,55]

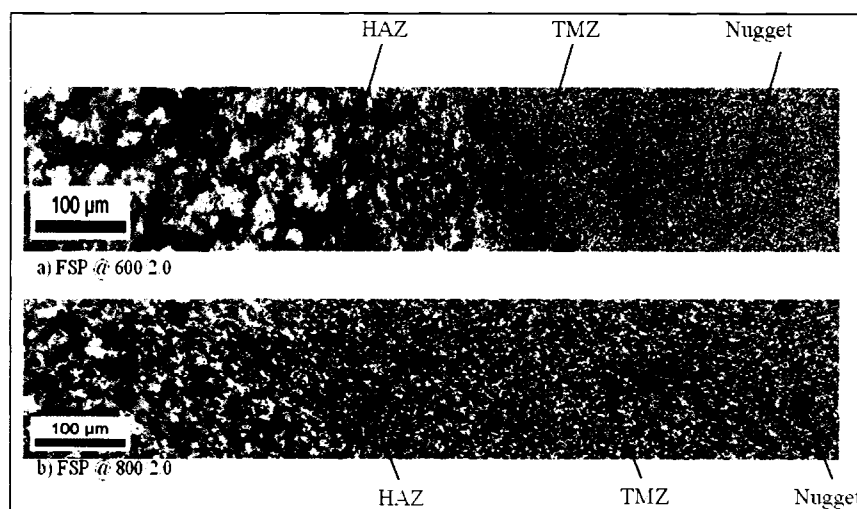


Figure 4- 14 grain structure at different locations of the FS processed AA5052 sheet, at two different conditions using OIM (In collaboration with Department of Mechanical Engineering, FAMU-FSU) [55]

4.4 Hardness

The results clearly show that hardness values and distributions of the processed sheets are extremely sensitive to the processing parameters. Higher microhardness values (up to 72.0 HV) than the hardness of the original material (68.0 HV) can be achieved at certain combinations of rotational and translational speeds. The effect of rotational speed on the resulting hardness is shown in *Figures 4-15*, where it is observed that increasing the rotational speed tends to decrease the resulting hardness. This result is in agreement with the results reported by Sato et al. [65] on aluminum alloys. This result is expected, since the temperature reached during processing increases with rotational speed, leading to more softening. According to the well-known Hall-Petch relationship, hardness is inversely proportional to grain size. Therefore, more refinement can be achieved at lower rotational speeds. The challenge, however, is to reduce rotational speed to allow more refinement, while achieving enough heat to soften the material and allow the pin to impose large plastic deformation. The effect of translational speed on hardness is opposite to that of rotational speed, as shown in *Figure 4-16*. By increasing translational speed, exposure time of the processed area to the temperature generated from rotating the tool is reduced, which limits the amount of grain growth. Therefore, it is expected that more refinement can be achieved by increasing the translational speed.

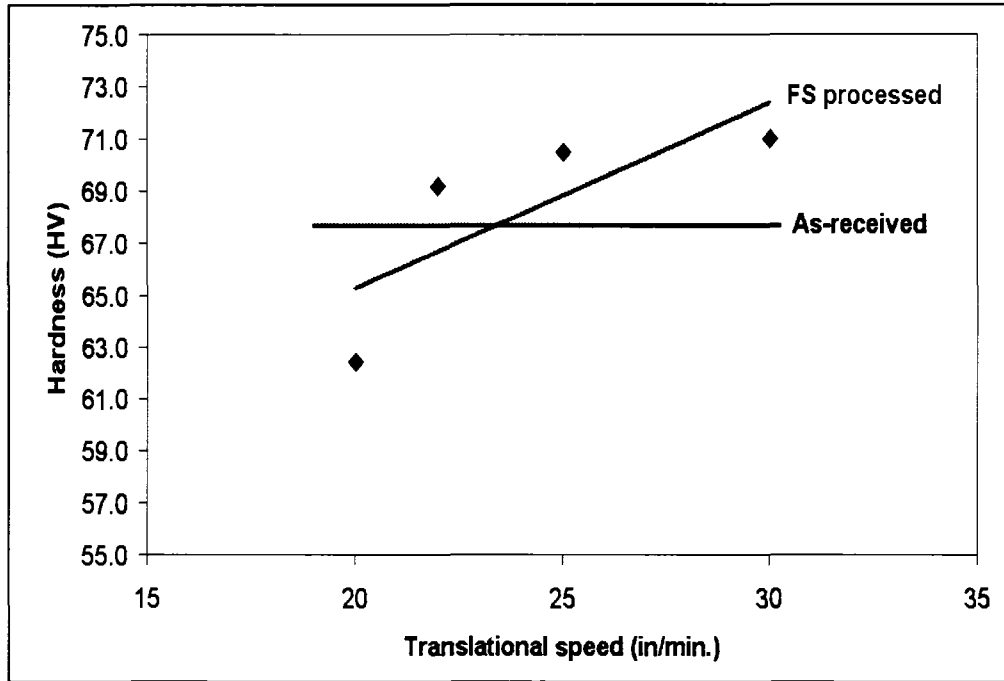


Figure 4- 15 Variation of hardness of FS processed AZ31B-H24 magnesium sample with translational speed (rotational speed is 1200 rpm.).

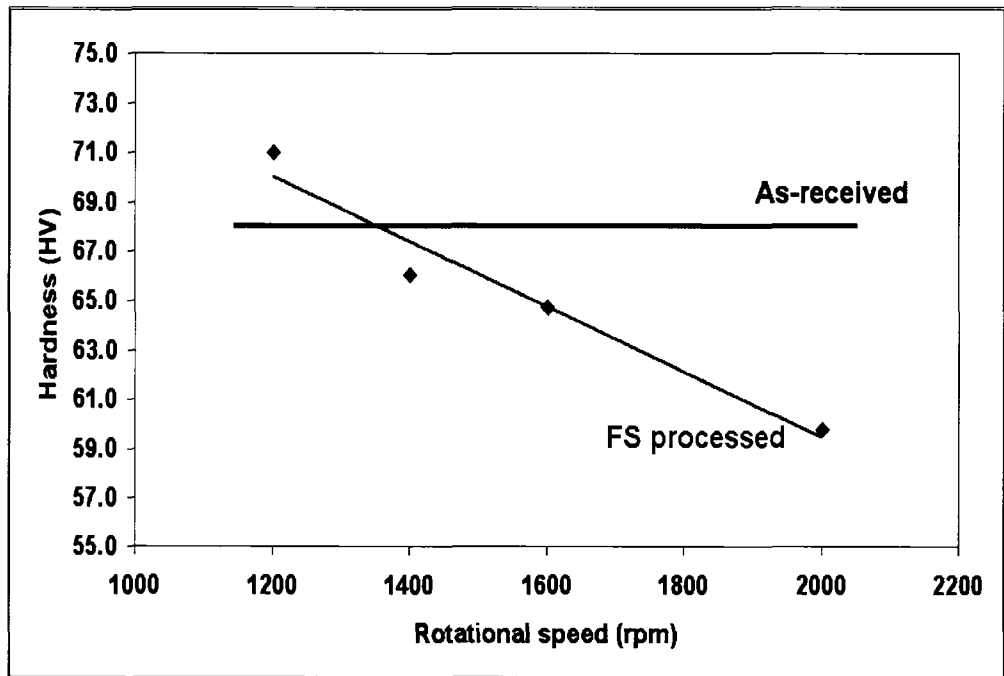


Figure 4- 16 Variation of the hardness of FS processed AZ31B-H24 magnesium sample with rotational speed (translational speed is 30.0 in. /min.).

Hardness distribution through the thickness of the processed zone is shown in *Figure 4-17*. Hardness variation can be explained on the basis of the temperature reached at different depths. As temperature decreases from the surface towards the bottom of the sheet, hardness increases. Higher temperature leads to more softening and more grain growth. This result is supported by the smaller grain size at the bottom of the processed zone, which was observed by Sutton et al. [66]. *Figure 4-18* shows the hardness profile at a transverse section of the processed sample. The hardness profile shows that maximum hardness occurs at the center of the deformation zone (nugget). An interesting result is also illustrated in *Figure 8*; minimum hardness values are taking place at the interface between the thermomechanical affected zone (TMAZ) and the heat affected zone (HAZ); hardness there is even smaller than that of the base material. Hardness drop in the heat affected zone is because there is no mechanical deformation taking place there; however the peak temperature reached is enough to soften the material. This result is in agreement with previously reported results for different aluminum alloys [39, 67].

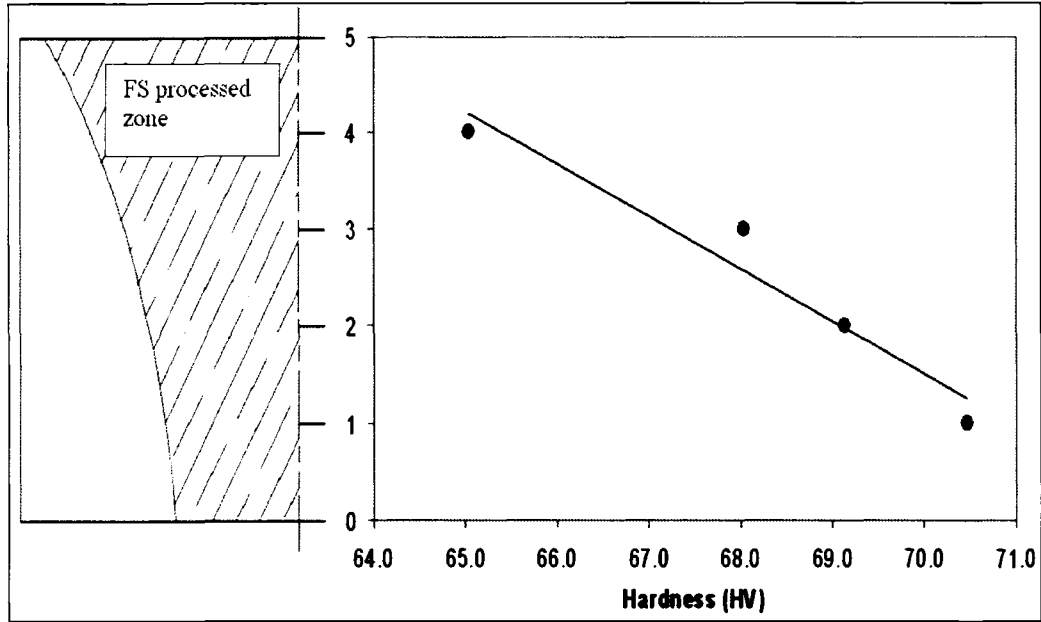


Figure 4- 17 Hardness variation within the thickness of FS processed AZ31B-H24 magnesium sample (1200 rpm and 22 in /min).

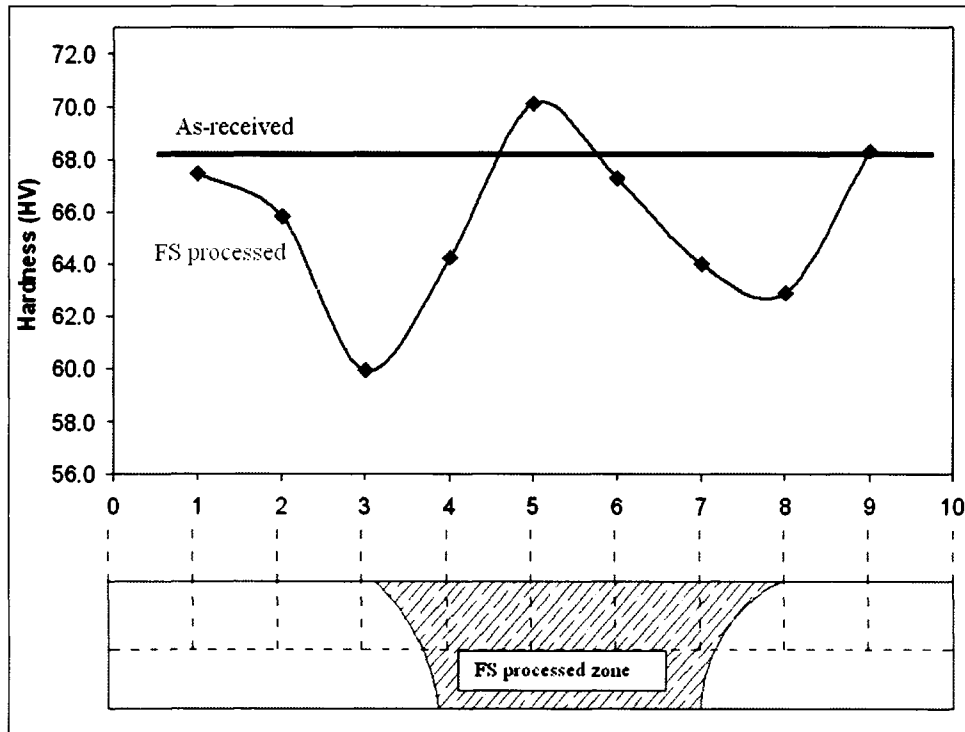


Figure 4- 18 Transverse hardness profile of FS processed AZ31B-H24 magnesium sample (1200 rpm and 30 in /min).

4.5 Conclusions

- Choosing the rotational and the translational speeds under which FSP is conducted is very important, and highly affects the resulting microstructure and consequently the hardness distribution for the FS processed material.
- Finer grain structures are obtained at lower rotational and higher translational speeds, which results in higher hardness values.
- Hardness variations are observed through thickness and transverse section of the FS processed area.
- Similar trends have been observed for both AZ31 magnesium alloys, and 5052 aluminum alloy.

Chapter Five

EXPERIMENTAL THERMAL INVESTIGATION

5. EXPERIMENTAL THERMAL INVESTIGATION

The Friction stir process is found to be very sensitive to thermal fields associated with the process. There are different thermal aspects which are critical to control and optimize the process. Temperature distribution is one important aspect; cooling and heating rates during FSP curves are also very important to determine the resulting microstructure and properties of the processed material. This motivated many researchers to investigate the different thermal aspects of the process using different methods and techniques.

In this chapter; the previous work that has been done in this field is discussed. And the experimental setup that has been used in this work is explained. Results that show thermal histories and distributions for both FS processed aluminium 5052 and magnesium AZ31B sheets are also discussed.

5.1 Previous Work

This section discusses some of the experimental thermal investigations that have been done by different researchers using different approaches and techniques.

Hofmann & Vecchio [68] measured the temperature for submerged FS processed Al-6061 sheet using thermocouples; their results showed that the maximum temperature reached in the sample is about 480°C, and that the heat input at the sample/weld interface

is high. Oh-ishi et al. [69] inserted thermocouples into the bottom center of a NiAl bronze plate and measured the peak temperature at the bottom of the nugget, and they found it to be between 940 °C and 1020 °C. Lambarkos et al. [36] used the inverse problem approach to generate the thermal profiles during FSW using thermocouple measurements. Song and Kovacevic [38] used an explicit central differential scheme to calculate the heat transfer during tool penetration, welding, and removal; and used thermocouples to measure the temperature fields. Song & Kovacevic [70] used infrared camera and thermocouples to validate their model; the measured peak temperature reached during FSW Al 6061/T6 sheet was around 820 K (~ 547°C). Reynolds et al. [71] presented the maximum FS weld temperature for Aluminium alloys as a function of RPM/(in/min.) ratio, and they found that the peak temperature is sensitive to the alloy composition. Xu et al. [72] studied temperature distribution during FSW using infrared camera and thermocouples; shoulder and pin contributions to the generated heat were investigated. Zettler et al. [73] investigated the effect of changing the tool geometry on FSW Mg alloys. They used thermocouples to measure the temperature, and they reported that temperature at the retreating side is slightly higher than the one at the advancing side, and that the peak temperature reached when FSW AZ31 alloy is higher than that for AZ61 alloy. In their work, Vilaca et al. [74] used thermocouples to measure the thermal fields at different points on both sides of the FSW weld. Frigaard et al. [75] used thermocouple measurements to determine the thermal cycles during FSW of different aluminum alloys with different heat treatment conditions, and then they used the experimental results to validate their model.

In general, thermocouples are positioned outside the deformation zone; and although they provide accurate temperature readings, their spatial resolution is limited by their junction diameter. Despite the many studies on thermal fields during FSW and FSP, an accurate correlation between temperature fields and process parameters that may explain the resulting microstructure does not currently exist.

In this work a dual-band thermographic approach is used to measure thermal fields during FSP. Different thermal aspects such as maximum temperature attained, temperature histories for a single point, line segment and tool/sheet contact point have been investigated and analyzed for different sheet materials (AA5052 and Mg-AZ31) processed at different combination of rotational and translational speeds.

5.2 Experimental Setup

A vertical CNC milling machine (HAAS VF-0F) is used to conduct the FSP. The tool used throughout this chapter is a simple cylindrical tool, with ½”-diameter flat shoulder and ¼”-diameter flat pin, and its height is ⅛”. The tool is made from H13 tool steel. Two different materials have been investigated (commercial 5052 aluminum alloy and AZ31B-H24 magnesium alloy) both in ⅛”-thickness sheet form. The AA5052 sheets were FS processed at 400-800 rpm and 1-3 in/min; 1200-2000 rpm and 20-30 in/min. were used for FSP the AZ31 Mg sheets. (For more information about the experimental setup, see *Chapter Three*).

Infrared thermography (IRT) provides accurate two-dimensional thermal maps of in-situ processes in non-invasive fashion (see *Figure 5-1*), and in real time acquisition rates. These inherent attributes motivated the wide acceptance of thermography in several industrial products monitoring and process control applications [76, 77]. Thermographic detectors scan the emitted radiation from surfaces and convert it into temperature values, utilizing Planck's law, which require a known emissivity value to provide an accurate conversion. The emissivity deviates from the unity value (black-body behavior) as a strong function of the material's facial status and the operating temperatures. Therefore, determining the emissivity becomes more critical when dealing with mirror-like surfaces involved in high temperature ranges (as the case during FSP). For this reason, a dual-band thermographic approach is used. *Figure 5-2* shows the experimental setup used in this work.



Figure 5- 12 Two-dimensional thermal map obtained using infrared camera.

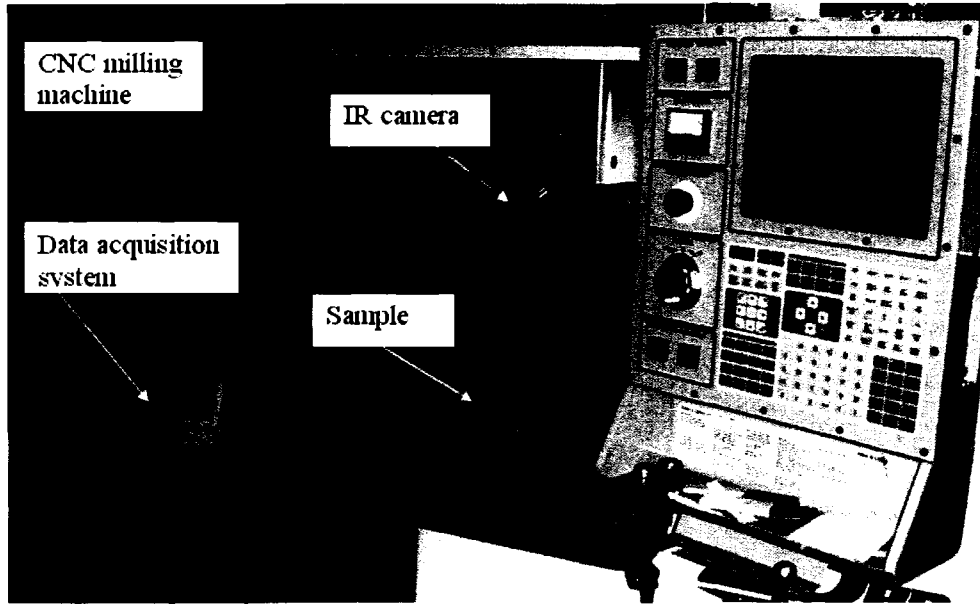


Figure 5- 13 Experimental setup

5.3 Results & Discussion

Results suggest that thermal fields have a critical role in determining the resulting microstructure and properties of the FS processed material. It is very important to choose the optimal process parameters that ensure the generation of enough heat to soften the material while limiting significant grain growth.

Thermal history of the interface point between the tool and the FS processed AA5052 sheet surface (see *Figure 5-3*), for different translational speeds (1.0 in/min. to 3.0 in/min.) and a fixed rotational speed (500 rpm), are shown in *Figure 5-4*. The maximum temperature attained was about 550°C (which is less than the melting point for Aluminum) for the 1.0 in/min. condition; and as the translational speed increases lower temperature is achieved during FSP, this due to the fact that translational speed controls

the duration of the rotating-tool at a certain affected zone of the base material, leading to different levels of heat generation.

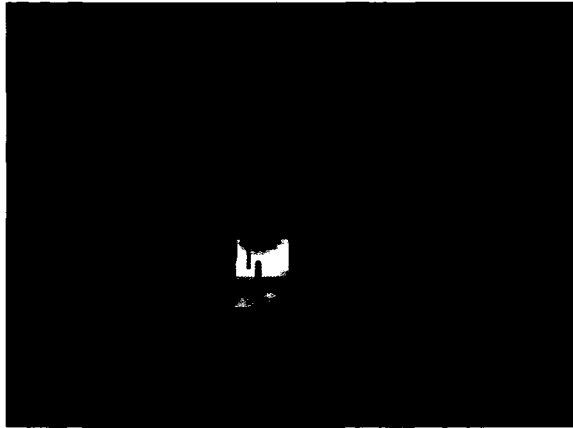


Figure 5- 14 Two-dimensional thermal map obtained using infrared camera, which shows the measured contact point.

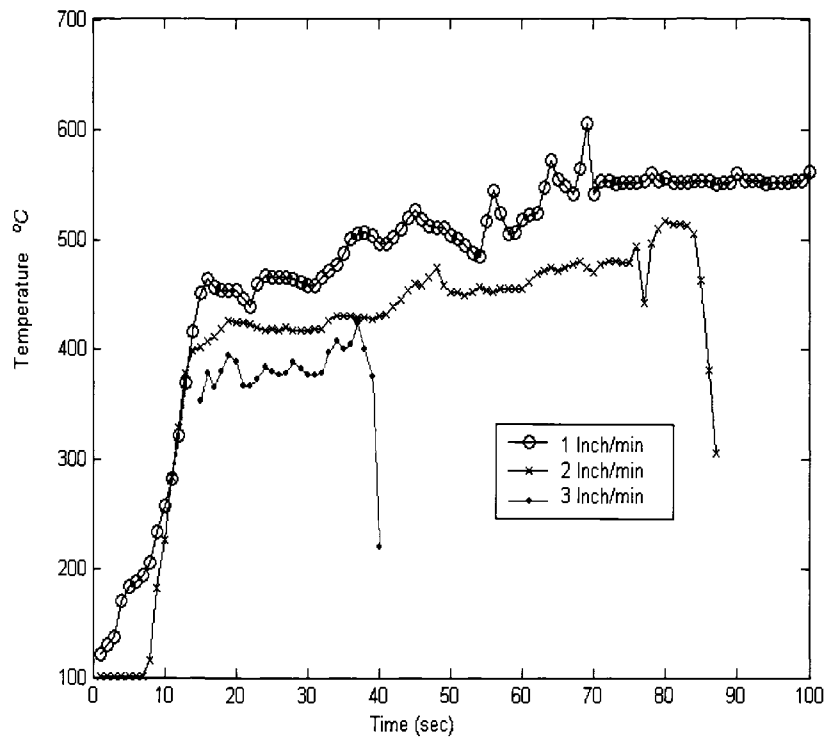


Figure 5- 15 Effect of Translational speed on the contact point temperature (fixed rotational speed 500 rpm) (AA5052 samples).

Similarly *Figure 5-5* shows the effect of rotational speeds by varying the rotational speeds from 400 rpm to 800 rpm while keeping the translational speed fixed at 2.0 in/min., again the temperature-time curve for the contact point (in situ) is displayed. The maximum temperature attained is for the higher rotational speeds and it is about 580°C (which is still less than the melting point of Aluminum), and as expected, as rotational speed decreases, the reached temperature decreases; which can be explained by that at higher rotational speeds more frictional heat and more plastic deformation is taking place and consequently higher temperature is reached during FSP.

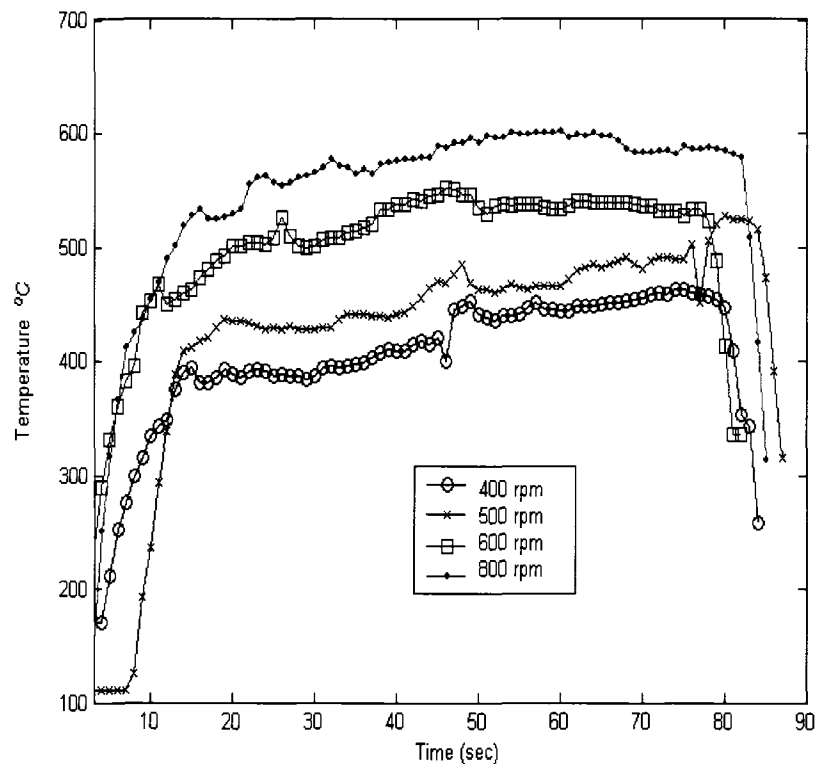


Figure 5- 16 Effect of Rotational speed on the contact point temperature (fixed translational speed 2 inch/min) (AA5052 samples).

So far, it is shown that temperature reached during FSP is sensitive to the process parameters (rotational and translational speeds). And as expected, finer grain size (more details can be found in *Chapter Four*) can be achieved when the maximum induced temperature is reduced (see *Figures 5-6 & 5-7*). The above statement confirms the importance of controlling temperature during processing for the optimization of the FSP induced microstructure. Manipulating the translational and rotational speeds adds to the flexibility of controlling the induced thermal energy.

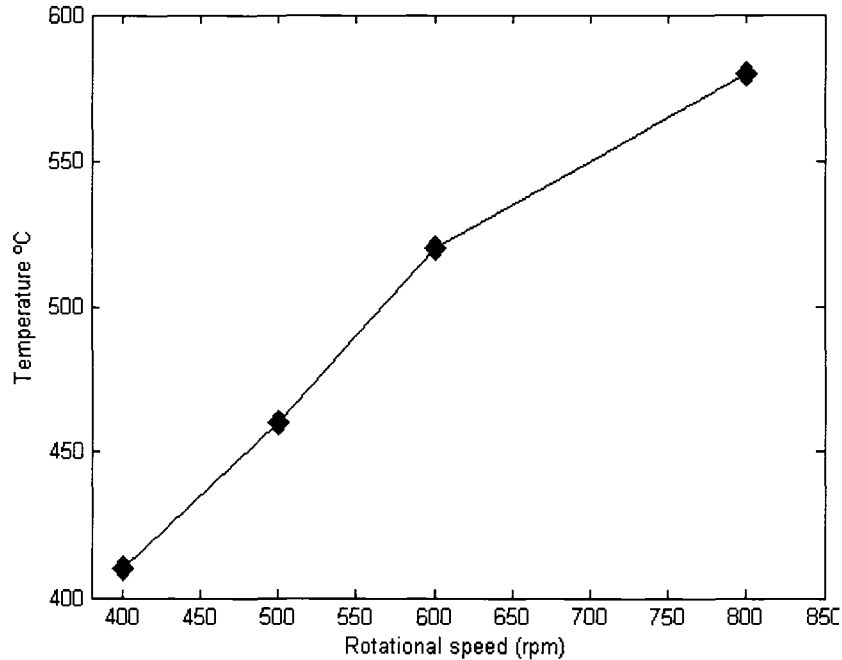


Figure 5- 17 Effect of rotational speed on maximum temperature reached during FSP of AA5052 samples.

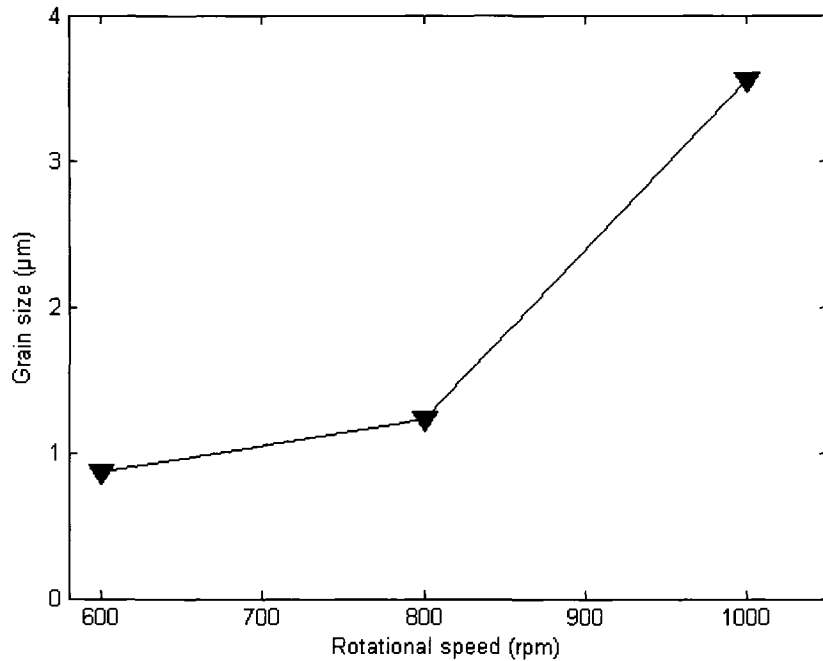


Figure 5- 18 Effect of rotational speed on the resulting grain size of FS processed AA5052 samples.

Figures 5-4 & 5-5 provide other valuable information about the friction-heating boundary condition, generated at the base metal; this could be usefully summarized by noting that the interface-point temperature is not constant as the tool traverses across the material surface, but instead it increases with a slope value of about $1.3^{\circ}\text{C}/\text{sec}$, as shown in *Figure 8* in which a close-up of the steady part of the 600 rpm curve. This increase happens because the points located ahead of the tool tip are affected by lateral conduction, which is boosted by the high thermal conductivity of the Aluminum alloy. Based on this observation, the tool heating performance is not steady across the sample; this affects the uniformity of the induced microstructure and consequently the material properties (see *Figure 5-9*).

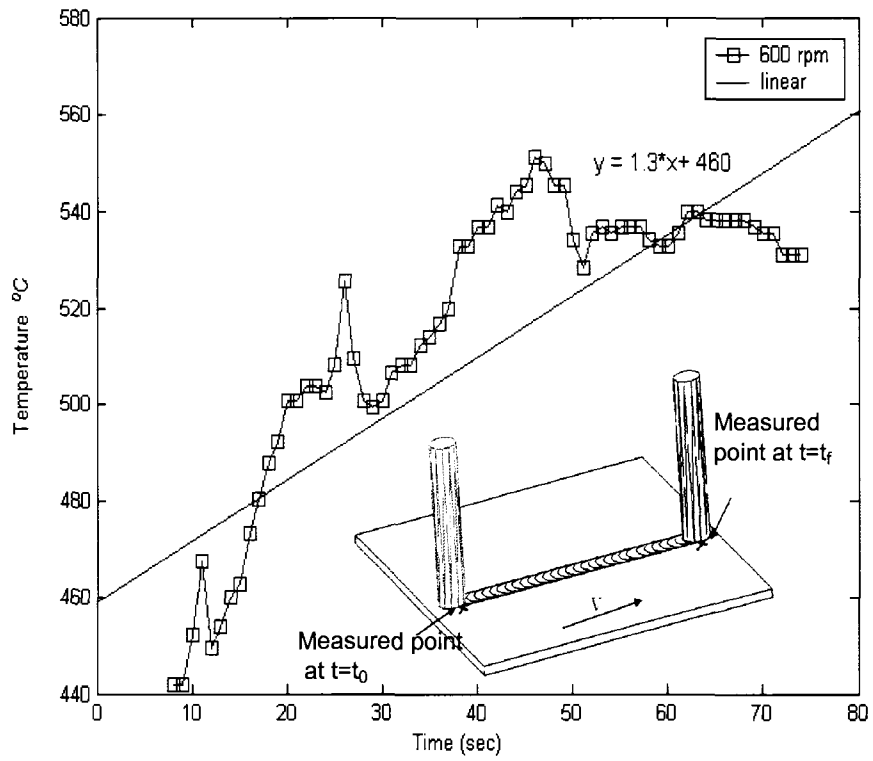


Figure 5- 19 Close-up of the steady part of the 600 rpm curve (AA5052 samples).

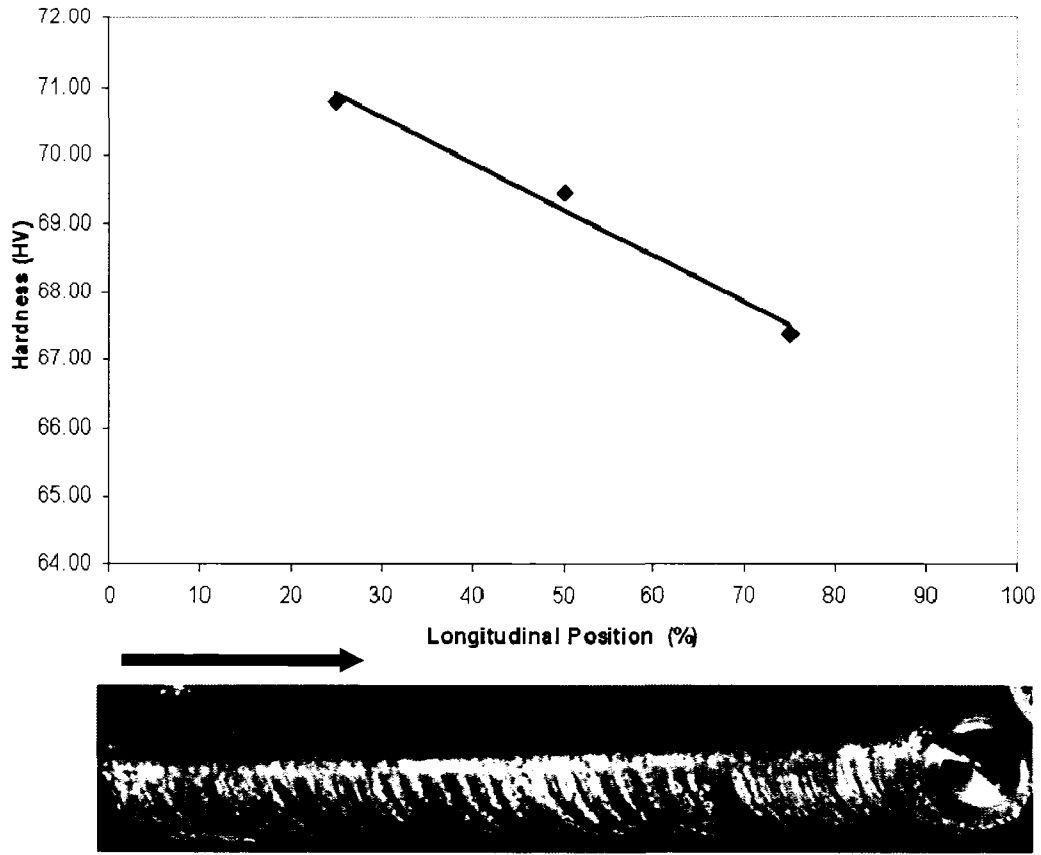


Figure 5- 20 Average hardness (HV) of FS processed AA5052 sample at different longitudinal positions (FSP at 500 rpm and 2 inch/min).

Figures 5-10 and 5-11 show the thermal trace of the tool on the base material (This figure helps predicting the cooling rate of the affected material zone). Controlling cooling rate enables a control over grain growth process by locking (freezing) the required size via a quick cooling rate; this could incorporate the addition of external cooling fluids or insulative backing materials. Computing the slopes of the curves in *Figure 5-11* quantifies the cooling rates; the obtained slope values are $110^{\circ}\text{C}/\text{inch}$, by observing *Figure 5-12*. It is also important to note that this value is a characteristic of the material undergoing FSP and is independent of the generated temperature, and

consequently independent of rotational and translational speeds. Cooling curves present helpful information about the quantity and the rate of the external coolant needed, and the optimal time for the external coolant to be implemented.

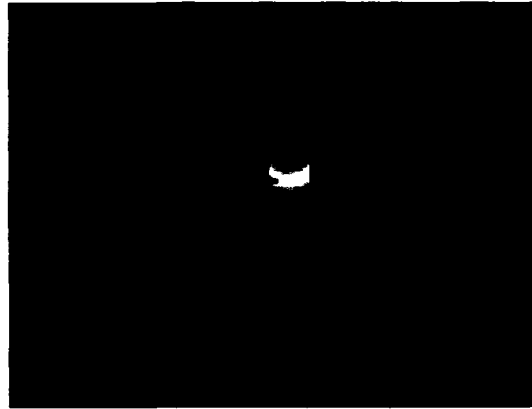


Figure 5- 21 Two-dimensional thermal map obtained using infrared camera, which shows the measured longitudinal segment.

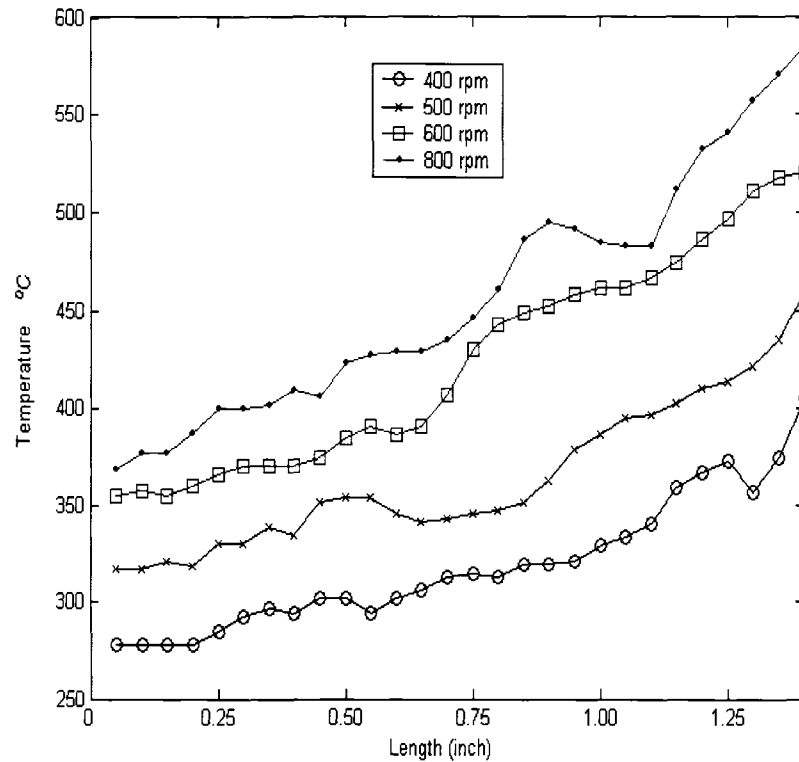


Figure 5- 22 Temperature distribution of a longitudinal segment during FSP at different rotational speeds (fixed translational speed 2 inch/min) (AA5052 samples).

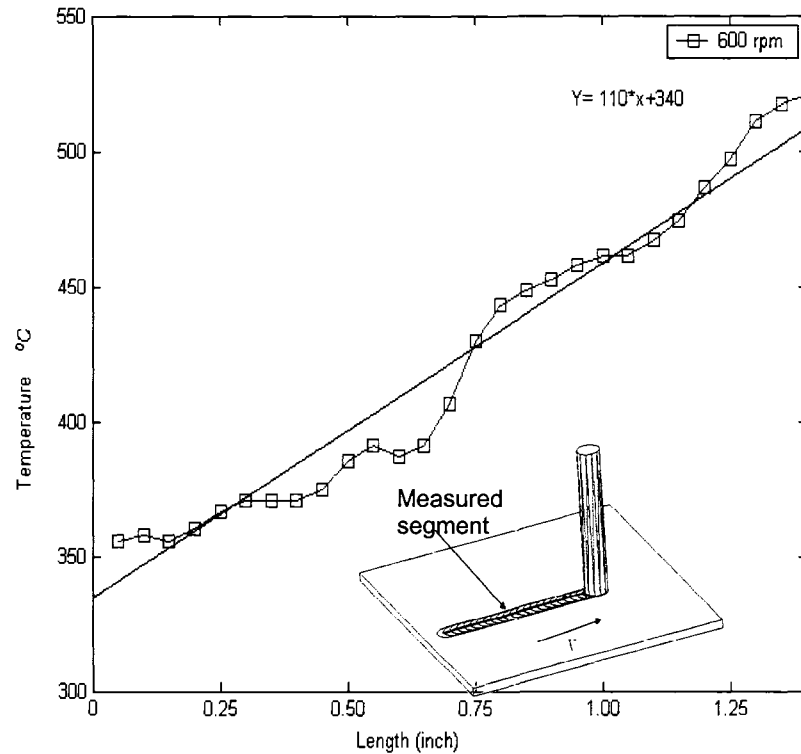


Figure 5- 23 Close-up of the 600 rpm curve (AA5052).

Figure 5-13 shows the temperature histories for a point within the processed area of AZ31B-H24 Mg sheets. The samples were friction stir processed at different rotational speeds (1200 rpm to 2000 rpm) and a fixed translational speed (22 in/min). Again as expected, the results show that the peak temperature is very sensitive to rotational speed; as rotational speed increases, peak temperature increases.

Similarly, Figure 5-14 shows the effects of translational speed; the translational speed here was varied between 20 in/min and 30 in/min while keeping the rotational speed fixed at 1200 rpm. Again the peak temperature is found to be sensitive to the translational speed; the peak temperature increases as the translational speed decreases.

The relations between maximum temperature reached during FSP and the rotational and translational speeds are shown in *Figures 5-15 and 5-16*, and the trends are similar to those observed for AA5052 samples. Very important information, other than the relations between the process parameters and the temperature reached during FSP, can also be obtained from such figures, such as:

- (1) The peak temperature reached during FSP varies between 420-580 °C, which is 0.70-0.90 of the melting point of Magnesium (~ 632 °C [78]); this means no melting is taken place during the process and that the FSP is a hot working process.
- (2) Heating and cooling rates are very important to control grain growth, hence optimize the process.
- (3) The period of time for which the material is exposed to a temperature higher than the recrystallization temperature; this is important because it affects the grain growth associated with the process.

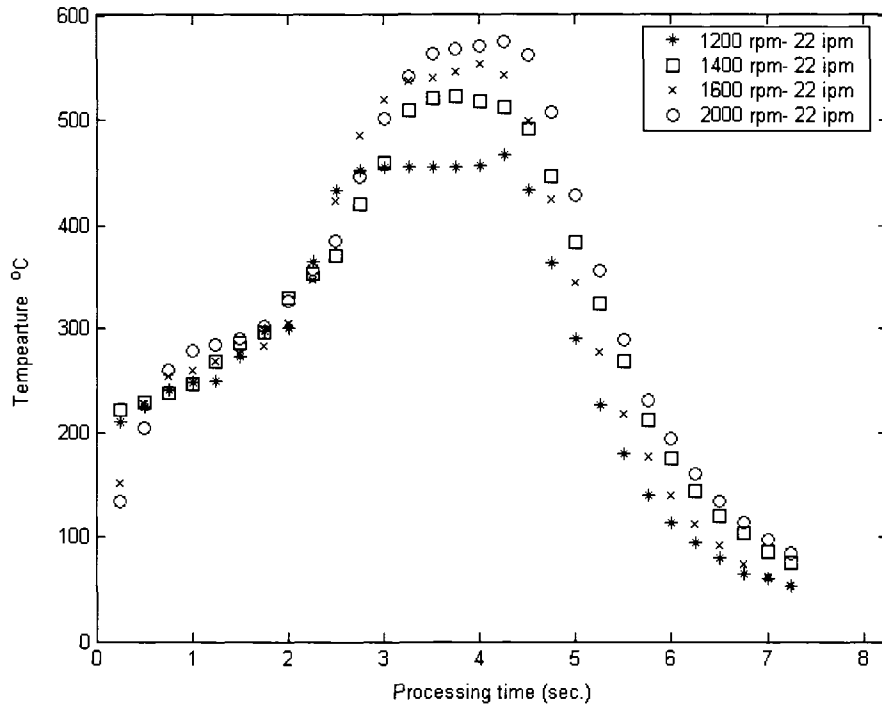


Figure 5- 24 Temperature histories for a point during FSP of Mg AZ31B-H24 sheets at different rotational speeds.

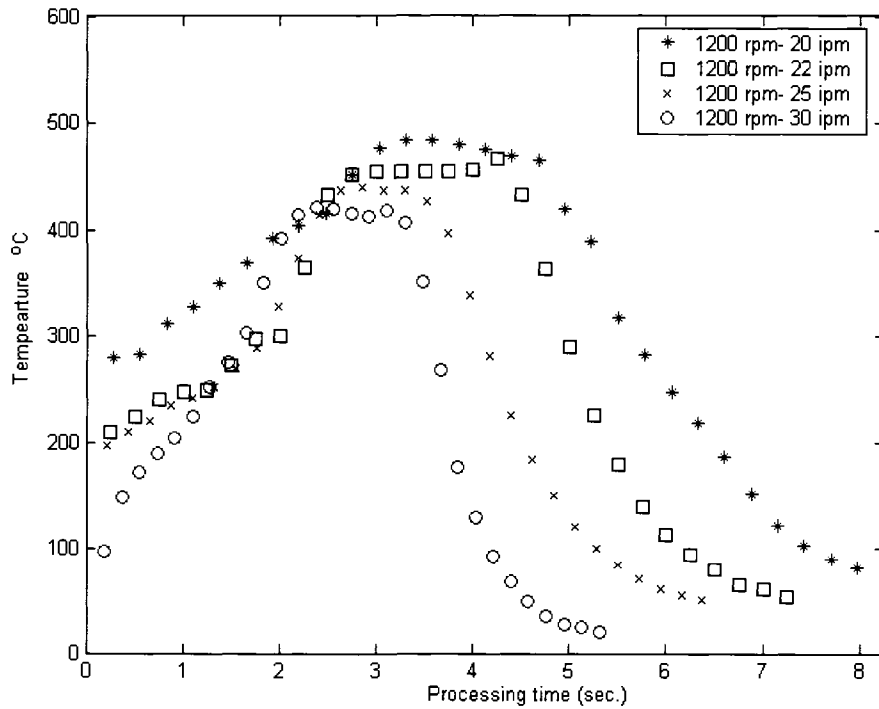


Figure 5- 25 Temperature histories for a point during FSP of Mg AZ31B-H24 sheets at different Translational speeds.

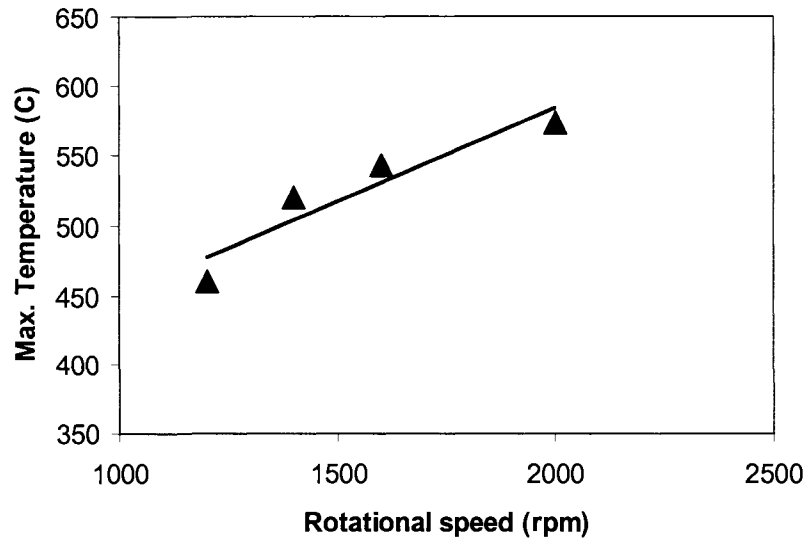


Figure 5- 26 Effect of rotational speed on the maximum temperature reached during FSP of Mg AZ31B-H24 samples (translational speed is 22 in/min).

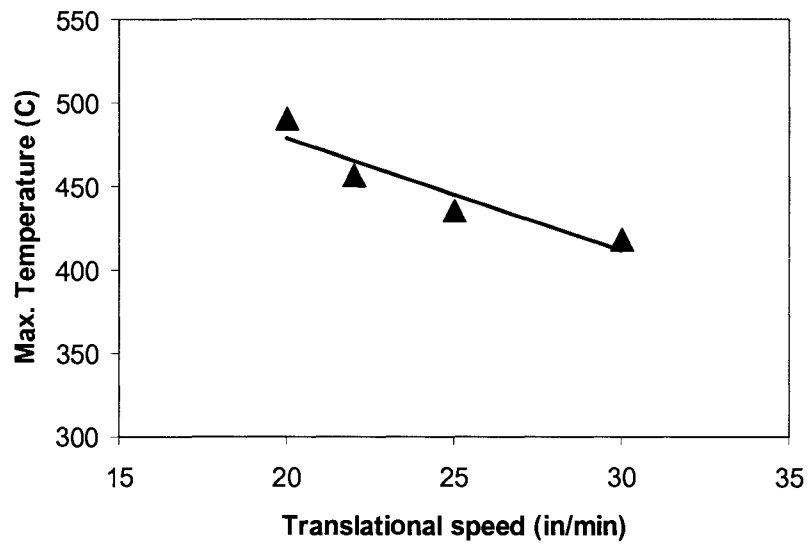


Figure 5- 27 Effect of translational speed on the maximum temperature reached during FSP of Mg AZ31B-H24 samples (rotational speed is 1200 rpm).

5.4 Conclusions

- Temperature distribution during FSP plays a critical role in controlling and optimizing the process.
- Temperature reached during FSP is very sensitive to the process parameters; higher temperature is reached at higher rotational speeds and lower translational speeds.
- Peak temperatures reached during FSP of different material and alloys are less than their melting temperature.
- Tool heating performance is not steady across the FS processed sample; which directly affects the uniformity of the resulting grain structure, and consequently the material properties.

Chapter Six

ANALYTICAL MECHANICAL MODEL

6. ANALYTICAL MECHANICAL MODEL

In order to advance the utilization of FSP in sheet metal processing and fabrication, accurate models are needed to enable process simulation and optimization. In this chapter; previous modeling activities that had been done are discussed, then our new analytical mechanical model is proposed in details. The results show the model's capabilities of predicting velocity fields and strain rate distributions of FS processed material at different process parameters, interfacial conditions and tool geometries.

6.1 Previous Work

Literature review of the modeling activities that took place in the field of FSP/FSW is presented in this section.

Ulysse [43] proposed a 3-D visco-plastic modeling for friction stir welding. Ulysse, in his model, assumed the material to be rigid visco-plastic material where the flow stress is function of temperature and strain rate, and an inverse sine-hyperbolic relation was used. He used standard compression tests and after applying the appropriate boundary conditions to determine the material constants. Then he used the conductive convection steady-state equation to describe his thermal model. The heat generation rate was assumed to be the product of the effective stress and the effective strain rate based on the assumption that about 90% of the plastic deformation is converted into heat. Ulysse

predicted the effect of tool speed and rotational speed on the temperature distribution within the plate. He used thermocouples to experimentally validate his model. In general the predicted temperatures were found to be higher than those obtained experimentally.

Nandan et al. [49] modeled three-dimensional visco plastic flow and temperature fields, by solving the equations of conservation of mass, momentum and energy in three dimensions using spatially variable thermophysical properties and non-Newtonian viscosity. They assumed incompressible viscoplastic material with a constant heat generation. Full sticking at the pin interface was assumed and partial sticking at the shoulder interface that had been adjusted to achieve good agreement with the measured temperature. Near the bottom the maximum strain rate is taken place at the surface of the pin (about 30/sec), however for upper region the maximum is taken place at the outer edge of the shoulder (higher than 100/sec). They computed viscosity as a function of strain rate and temperature. The viscosity distribution was predicted and iso-viscosity surface were predicted, from which the geometry of the TMAZ can be predicted. Nandan et al. calculated the cutoff viscosity above which no significant material flow occurs to be 5 MPa-s.

Fratini et al. [51] proposed a numerical model that aimed at the determination of the average grain size due to continuous dynamic recrystallization phenomena in friction stir welding of AA6082 T6 aluminum alloy. The proposed model took into account the local effects of strain, strain rate and temperature on the average grain size. The final size of the continuously recrystallized grain is influenced by the local value of few field

variables, such as the strain, the strain rate and the temperature levels as well as the considered material.

Chang et al. [44] in their work, proposed a relation between grain size of friction stir processed AZ31 Mg alloys and the Zener-Holloman parameter. Their results showed that the strain rate and the working temperature have a great influence on the resulting grain size in extruded Mg based alloy. So they used the Zener-Holloman parameter to relate the resulting grain size to because it is a function of strain rate, temperature and material constants. In their work a simple linear assumption had been made so the average material flow was assumed to be half the pin rotational speed, based on the fact that the material flow during FSP is related to the pin rotational speed which may be equal or less than the pin rotational speed. Then the torsion type deformation during FSP was calculated, and the temperatures data used were obtained experimentally and the grain sizes were obtained by microstructural characterization using optical microscopy and scanning electron microscopy (SEM). They used the experimental results to quantitatively relate the grain diameter to the Zener-Holloman parameter during FSP of AZ31 Mg alloy.

Heurtier et al. [45] in their work, proposed a model of material flow pattern of friction stir welding process. They considered two zones within the weld area. Using classical fluid mechanics and assuming the flow to be incompressible and kinematically admissible, the velocity fields within each zone were developed. The first zone is located just below the shoulder of the tool, in which the bulk material flowing around the screw

head pin (translation velocity field) is submitted to an additional torsion velocity field. This torsion is imposed by friction of rotating shoulder on surface and partially affects the depth of the metal sheets over a range of 1 or 2 mm. The second zone which is located within the depth of the welded zone (nugget zone and thermomechanically affected zone) is submitted to the translation motion of the pin and the vertical motion of the bulk material, dragged down by the screwing kinematics of the tool. In their work, they expressed the velocity fields as functions of the torsional velocity of the material itself, which linearly extrapolate of the rotation velocity of the tool. The temperature within the weld was predicted with the assumption that the whole plastic power is dissipated into heat, and they also presented the predicted strain map.

Schmidt et al. [46] analytically modeled the heat generation in friction stir welding. They studied different contact conditions between the tool and the weld; sliding, sticking and partial sliding/sticking. They used experimental plunge force and torque measurements to determine the contact condition. Three contact states conditions were defined; sticking condition: where the material of weld stick to the tool surface, and this happens when the friction shear stress exceeds the yield shear stress of the weld and so the material of weld have the tool velocity, sliding condition: which occurs when the contact shear stress is smaller than the yield shear stress of the weld, the weld segment shears slightly to a stationary elastic deformation, where the shear stress equals the dynamic contact shear stress, partial sliding/sticking which is a state between sliding and sticking. Contact state variable was introduced to define the contact condition and to relate the material velocity to the tool velocity.

Schneider et al [48] described the material flow path during FSW using a mathematical model. In their work, they suggested that to describe the material flow in friction stir welds three incompressible flow fields have to be considered. The first field is a rigid-body rotation which is identical to the rotation of the tool spindle and bounded by a cylindrical shear surface. The second field is a homogenous and isotropic velocity field with the velocity equal and opposite to the travel velocity of weld-tool. The third is a ring vortex flow in which the metal moves up and down. They inserted thin tungsten wire inside the FSW seam to investigate the material flow; if the shear stresses were severe then the wire would break, as a result of tension if the wire was flexible and as a result of bending if the wire was stiff. Their experimental results which showed that the wire was broken into uniform segments suggested that a tensile failure mode is occurred. Most of the wire segments were arrayed in a straight line which suggested that a rigid body rotation at the tool superposed by uniform translation would exhibit the same flow pattern of streamlines in the plane view.

Buffa et al. [50, 79] proposed thermomechanical 3D numerical model based on rigid viscoplastic material and continuum assumptions for FSW. Temperature, strain and material flow were predicted. Their simulations showed that the temperature distribution is symmetric however the material flow was not. And then they used their model to design the tool by investigating the effect of pin angle on the process. They concluded that increasing the pin angle enlarges both the heat-affected zone and thermal mechanical zone resulting in a bigger weld nugget, and increases the overall temperature. The plastic deformation in the nugget increases with the pin angle.

Arbegast [47] based his simple model on metalworking process. He attempted to develop relationships for calculating width of extrusion zone, strain rate and pressure. Arbegast presented empirical relations between maximum temperature, material constitutive and process parameters. Arbegast described the material flow during FSW: the material exceeds the critical flow stress due to the heat caused by the forward movement of the, then it is forced upwards into the shoulder zone and downwards into the extrusion zone, there are two more zones: one is the swirl zone which represents the small amount of material captured beneath the pin tip where a vortex flow exists, and the other one is the forging zone where the material from the front of the pin is forced under a hydrostatic pressure conditions into the cavity left by the forward moving pin tool. The maximum temperature during FSW was predicted using a simple thermal model, the results showed that; rotational speed is the dominant factor when it comes to the maximum temperature, and it was observed that temperature was a slightly higher t on the advancing side.

Reynolds et al. [40] used two different approaches to models friction stir welding process. In the input torque based thermal model; they assumed the average shear stress at the workpiece/tool interface, and then they correlated the heat input correlated to the measured torque. The main output of this model was a time/temperature history. In the 2-D fluid dynamics based model, they assumed that the flow past a rotating cylinder with a no slip boundary condition at the tool workpiece interface, the effective deviatoric stress expressed as a function of temperature and strain rate. Prezna's viscoplasticity model

(dynamic viscosity is temperature and strain rate dependent) was used to calculate the dynamic viscosity. The lack of a strain history effect on the flowing material (no strain hardening), and the neglect of elastic deformation on dynamic viscosity were the main limitations of such a model.

Stewart et al. [80] proposed two models using experimental and analytical approach. In the first model which is the Mixed Zone model; they assumed that rotational slip of the material to take place within the whole plastic zone and not only on the tool-workpiece interface, the velocity within the plastic zone flows in vortex pattern to match the angular velocity of the tool at the tool-workpiece interface and dropped to zero at the edge of the plastic zone. For the second model which is the Single Slip Surface model, they assumed the rotation slip to take place at a contracted slip surface outside the tool-workpiece interface, the results of this model showed a good agreement with the experimental measurements of thermal field, forces and shape of the weld region. But this model did not account for the three dimensional effects.

Song et al. [81] proposed a three-dimensional heat transfer model. They considered both the heat generated by the tool pin and shoulder, and they were assumed to be frictional heat. Finite different method was used to solve the control equations. To verify their model Song et al. temperature history obtained experimentally using thermocouples and infrared camera. Song et al concluded that using moving coordinate instead of moving heat source can facilitate applying a coupled heat-transfer process for both the tool and workpiece during FSW.

Askari et al. [37] proposed a three-dimensional analysis; the aim of their work is to capture the coupling between tool geometry, heat generation and plastic flow of the material. In their model they solved; the steady-state continuity and momentum balance equations and the steady-state energy equation. Their results showed the predicted the temperature, flow stress, vertical velocity and the plastic strain rate, and they used experimental data obtained by thermocouples and marking experiments to validate their model.

More work has to be done in order to understand the physics behind the process. The complex coupled mechanical and thermal aspects of the process have not yet been well understood, and require an integrated multidisciplinary approach including mechanics, microstructure and thermal sciences, which is the main approach followed in this research. And yet in order to optimize the process and in order to reach a point where we can design a material with desired properties, a comprehensive and accurate model that can predict the resulting microstructure (and consequently the material's properties) is very much needed to advance widespread use of FSP.

6.2 Current Model

The current work presents a model that estimates the strain rate distribution within the friction stir processed zone in terms of process parameters. In this model, the velocity fields within the processed zone are determined by considering the effects of both the

shoulder and the pin of the tool on the material flow. State variables are introduced to relate the material velocity in the processed zone to the velocity of the tool (the shoulder and the pin). In addition, weight functions are used to determine the contribution of the shoulder and the pin on the material flow within the processed zone. From the velocity fields, the strain rate distribution in the processed zone can then be estimated. Different scenarios are considered to investigate the effects of both the pin and the shoulder on the material flow and consequently on the strain rate distribution. The effects of contact conditions at the tool/sheet interfaces and process parameters (rotational and translational speeds) are also investigated.

Table 6- 1 Nomenclature

| <u>Nomenclature</u> | |
|----------------------------|--|
| r | Radial distance from the tool center (m) |
| r_p | Pin radius (m) |
| r_s | Shoulder radius (m) |
| z | Distance from top to bottom in the thickness direction (m) |
| z_o | Pin height (m) |
| θ | The angle from the radial axis at the middle section of the tool (moving clockwise when looking from the top)(radians) |
| ω | Rotational speed o the tool (rad/s) |
| v | Translational speed of the tool (m/s) |
| $V_{material}$ | FS processed material resultant velocity(m/s) |
| $V_{shoulder}$ | Shoulder resultant velocity(m/s) |
| V_{pin} | Pin resultant velocity (m/s) |
| η | Material/pin state variable |
| λ | Material/shoulder state variable |
| $u_{(s)\theta}$ | Material velocity component caused by shoulder in the θ direction (m/s) |
| $u_{(s)r}$ | Material velocity component caused by shoulder in the r direction (m/s) |
| $u_{(p)\theta}$ | Material velocity component caused by pin in the θ direction (m/s) |
| $u_{(p)r}$ | Material velocity component caused by pin in the r direction (m/s) |
| $w_{(s)\theta}$ | Shoulder weight function in the θ direction |
| $w_{(s)r}$ | Shoulder weight function in the r direction |
| $w_{(p)\theta}$ | Pin weight function in the θ direction |
| $w_{(p)r}$ | Pin weight function in the r direction |
| u_{θ} | Material resultant velocity component in the θ direction (m/s) |
| u_r | Material resultant velocity component in the r direction (m/s) |
| u_z | Material resultant velocity component in the z direction (m/s) |
| $\dot{\epsilon}_{eff}$ | Effective strain rate (1/s) |

6.2-1 Model Development

The ultimate goal is to develop a physics-based model that can accurately predict the resulting microstructure of FS processed material in terms of process parameters. The model presented below serves as a first step towards that goal in order to enable FSP to “design” a certain microstructure for optimum performance.

FSP is considered a hot working process where the flow stress is highly dependent on temperature and the strain rate. The resulting grain structure in the processed zone mainly depends on the resulting strain rate and temperature distributions. In order to be able to achieve a desired microstructure, the strain rate and temperature distributions must be controlled and related to the grain structure and process parameters.

This work attempts to develop an analytical model to predict the strain rate distribution during FSP. The framework of this model is as follows:

- State variables that relate the material velocity to the tool velocity (shoulder and pin) are first introduced.
- Weight functions are also introduced to determine how much the tool shoulder and the tool pin contribute the net flow of material in the processed zone.
- The velocity fields in the processed zone are then determined as a function of process parameters.
- Finally, the strain rate distribution in the deformed (processed) zone is calculated from the velocity fields.

For convenience, a table of nomenclature is included for easy reference to the different terms and symbols used in the following equations. A schematic of the proposed model is shown in *Figure 6-1* illustrating the tool/sheet interfaces and the proposed geometry of the deformation zone. In this work, the dimensions of the radii of the pin and the shoulder are $r_p = 3.175$ mm and $r_s = 6.350$ mm, respectively. These numbers are the actual dimensions of the tool currently used in our laboratory to conduct FSP experiments [4, 5, and 14]. A flat shoulder and a flat cylindrical pin are considered in this analysis. The sheet thickness is $z_0 = 3.175$ mm (see *Figure 6-1*). In this work different rotational speeds (400 - 600 rpm) and translational speeds (0.847 – 2.540 mm/s) are covered. These values are typical of speeds used in FSP of aluminum alloys [12, 17 and 82].

The main assumptions that have been made for developing the model include:

- Two incompressible flow fields are combined to describe the material flow; rigid body rotation and uniform translation.
- No material movement in the thickness direction is considered.
- The contact condition is constant along each interface; however, different contact conditions can be used.
- The overall velocity field in the processed zone is determined by combining the velocity fields based on the movements of the tool shoulder and the tool pin independently using weight functions.

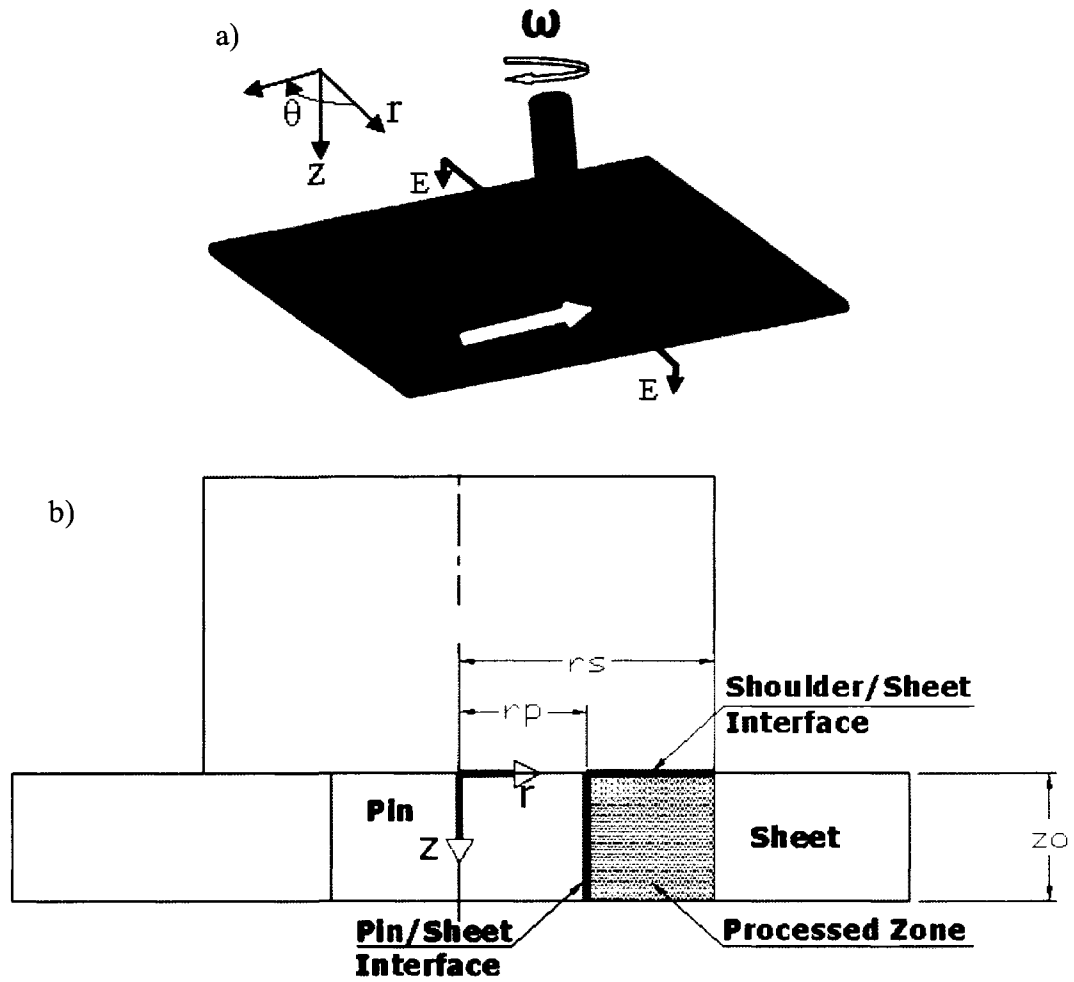


Figure 6- 1 Model's geometry a) 3-D and b) cross section EE

6.2-2 State-variables

The first step is to define how the material velocity is related to the tool velocity. There are several factors that control this relation including contact condition at the tool/sheet interfaces, tool geometry, sheet clamping force, material properties, temperature and pressure. In order to consider these effects, state-variables are introduced. There are two interfaces between the tool and the sheet; one is at the shoulder

and the other is at the pin (as shown in *Figure 6-1*). The material flow and movement is influenced by both the shoulder and the pin in different ways; the shoulder is mainly responsible for material flow near the sheet surface while the pin is responsible for stirring the material through the sheet thickness. For this reason, two state-variables are needed. The first one is denoted η (see Equations 6.1-6.2), which relates the material velocity to the shoulder velocity, and it is defined as a function of z (the distance from top to bottom in the thickness direction). Two other parameters are used to define η ; the first one is A which represents the contact state at the shoulder/material interface. The value of A varies between 0 and 1; 1 for full sticking, 0 for full slipping and $0 < A < 1$ for combined sticking-slipping contact condition. The second parameter used to define η is B which accounts for the effect of material properties, temperature and pressure. The same approach is followed to define the second state variable λ (see Equations 6.3-6.4), which relates the material velocity to the pin velocity. The state variable λ is defined in terms of r (the radial distance from the tool center), and the two parameter C and D (C is equivalent to A and D is equivalent to B). Mathematically, the state variables are given by:

$$\eta = \frac{V_{material}}{V_{Shoulder}} \quad (6.1)$$

$$\eta = A \exp\left(-B \frac{z}{z_o}\right) \quad (6.2)$$

$$\lambda = \frac{V_{material}}{V_{pin}} \quad (6.3)$$

$$\lambda = C \exp \left(-D \frac{(r - r_p)}{(r_s - r_p)} \right) \quad (6.4)$$

To explain the physical meaning of these state variables, consider the state variable, η relating the material velocity resulting from the shoulder movement to the shoulder velocity. At the sheet surface ($z = 0$), the state variable (η) equals the parameter A . For full sticking condition, A equals 1, which result in a material velocity equals to the shoulder velocity. For full slipping condition ($A = 0$), the material is stagnant at the sheet surface. The physical meaning of the state variable relating the material velocity resulting from the pin movement to the pin velocity is analogous to the one described above.

6.2-3 Weight functions

The shoulder and the pin both affect the material movement within the processed zone. To account for how much each of them is responsible for the material flow; weight functions are introduced. The main idea is to assume as if the two act independently and then combine their effect. First it is assumed that the shoulder is only responsible for the material flow (and no material movement is resulted from the pin) and the velocity field from this scenario is determined. Second the velocity field is determined assuming the material movement and flow is only caused by the pin. Finally, the two velocity fields are combined using the weight functions to yield the overall velocity field. The weight functions for the shoulder and the pin are defined in both r and θ coordinates (θ is the

angle from the radial axis at the middle section of the tool as shown in *Figure 6-1a*) as given below in Equations 6.5-6.8.

$$w_{(s)\theta} = \frac{u_{(s)\theta}}{u_{(s)\theta} + u_{(p)\theta}} \quad (6.5)$$

$$w_{(p)\theta} = \frac{u_{(p)\theta}}{u_{(s)\theta} + u_{(p)\theta}} \quad (6.6)$$

$$w_{(s)r} = \frac{u_{(s)r}}{u_{(s)r} + u_{(p)r}} \quad (6.7)$$

$$w_{(p)r} = \frac{u_{(p)r}}{u_{(s)r} + u_{(p)r}} \quad (6.8)$$

6.2-4 Velocity fields

Two incompressible flow fields are combined to describe the material flow in the FS processed zone; rigid body rotation and uniform translation. The material movement in the z direction is not considered in this analysis. The velocities of both the shoulder and the pin are described in terms of the rotational and translational speeds of the tool along with the state variables (Equations 6.9-6.12):

$$u_{(s)\theta} = \eta [\omega r - v \cos(\theta)] \quad (6.9)$$

$$u_{(s)r} = \eta [-v \sin(\theta)] \quad (6.10)$$

$$u_{(p)\theta} = \lambda [\omega r_p - v \cos(\theta)] \quad (6.11)$$

$$u_{(p)r} = \lambda [-v \sin(\theta)] \quad (6.12)$$

Incorporating the weight functions with these velocity fields yields the overall velocity field in the r- θ -z coordinates as given by Equations 6.13-6.15.

$$u_\theta = w_{(s)\theta} u_{(s)\theta} + w_{(p)\theta} u_{(p)\theta} \quad (6.13)$$

$$u_r = w_{(s)r} u_{(s)r} + w_{(p)r} u_{(p)r} \quad (6.14)$$

$$u_z = 0 \quad (6.15)$$

6.2-5 Strain rate

The velocity-strain rate relations in cylindrical coordinate are used to find the strain rate components (Equations' set 6.16) [83]. The effective strain rate distribution within the FS processed zone can be determined assuming von Mises according to Equation 6.17.

$$\left. \begin{aligned} \dot{\epsilon}_{rr} &= \frac{\partial u_r}{\partial r} \\ \dot{\epsilon}_{\theta\theta} &= \frac{1}{r} \frac{\partial u_\theta}{\partial \theta} - \frac{u_r}{r} \\ \dot{\epsilon}_{zz} &= \frac{\partial u_z}{\partial z} \\ \dot{\epsilon}_{r\theta} &= \frac{1}{2} \left[\frac{1}{r} \frac{\partial u_r}{\partial \theta} + \frac{\partial u_\theta}{\partial r} - \frac{u_\theta}{r} \right] \\ \dot{\epsilon}_{\theta z} &= \frac{1}{2} \left[\frac{\partial u_\theta}{\partial z} + \frac{1}{r} \frac{\partial u_z}{\partial \theta} \right] \\ \dot{\epsilon}_{zr} &= \frac{1}{2} \left[\frac{\partial u_z}{\partial r} + \frac{\partial u_r}{\partial z} \right] \end{aligned} \right\} \quad (6.16)$$

$$\dot{\epsilon}_{eff} = \left(\frac{2}{3} \dot{\epsilon}_{ij}^2 \right)^{1/2} \quad (6.17)$$

6.3 Results and Discussion

6.3-1 Shoulder and pin effects

The effects of the shoulder and the pin; separately and combined, on material deformation within the FS processed zone are illustrated by the three velocity fields shown in *Figure 6-2*. It is obvious that when considering the effect of the pin alone (*Figure 6-2a*), the material velocity decreases as the radial distance from the tool's center increases, as illustrated by Equations 6.4 and 6.11. It is important to note that the velocity at a given radius is constant along the thickness (z) direction because the velocity

depends on the radius and the contact condition at the pin/material interface. In this analysis, it is assumed that the contact condition does not change along the pin/material interface. Considering the shoulder effect (*Figure 6-2b*), the results show that the material velocity increases as the radial distance from the tool's center increases and the distance along the thickness from the top surface of the sheet decreases as illustrated by Equations 6.2 and 6.9. *Figure 6-2c* shows the combined effects of the shoulder and the pin on the material velocity. The maximum velocity occurs at the outer edge of the shoulder/sheet interface in agreement with the findings of Nandan et al. [49]. Similar trends are noticed for the strain rate distributions, as shown in *Figure 6-3*. It is very important to note that the obtained strain rate values are in the order of hundreds which are in agreement with reported values in the literature [46, 49]. Schmidt et al. [46] showed in their work that the shear rate was in the order of hundreds, and Nandan et al. [49] predicted the maximum strain rate to be about 160 s^{-1} . The high strain rate values confirm that intense plastic deformation at high rates is taking place during FSP.

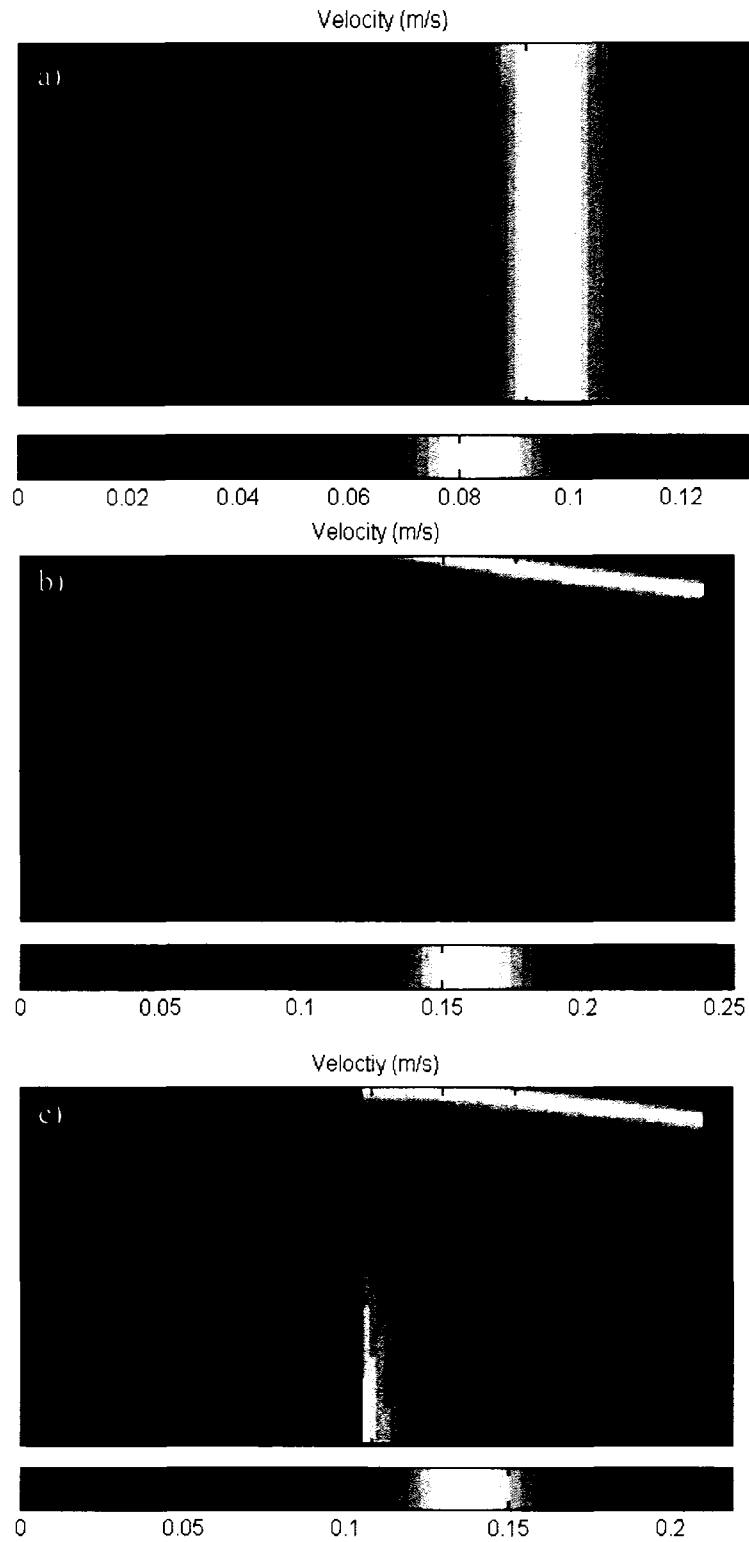


Figure 6- 2 Velocity fields for FSP at 400 rpm and 0.847 mm/s a) pin alone b) shoulder alone c) combined shoulder and pin

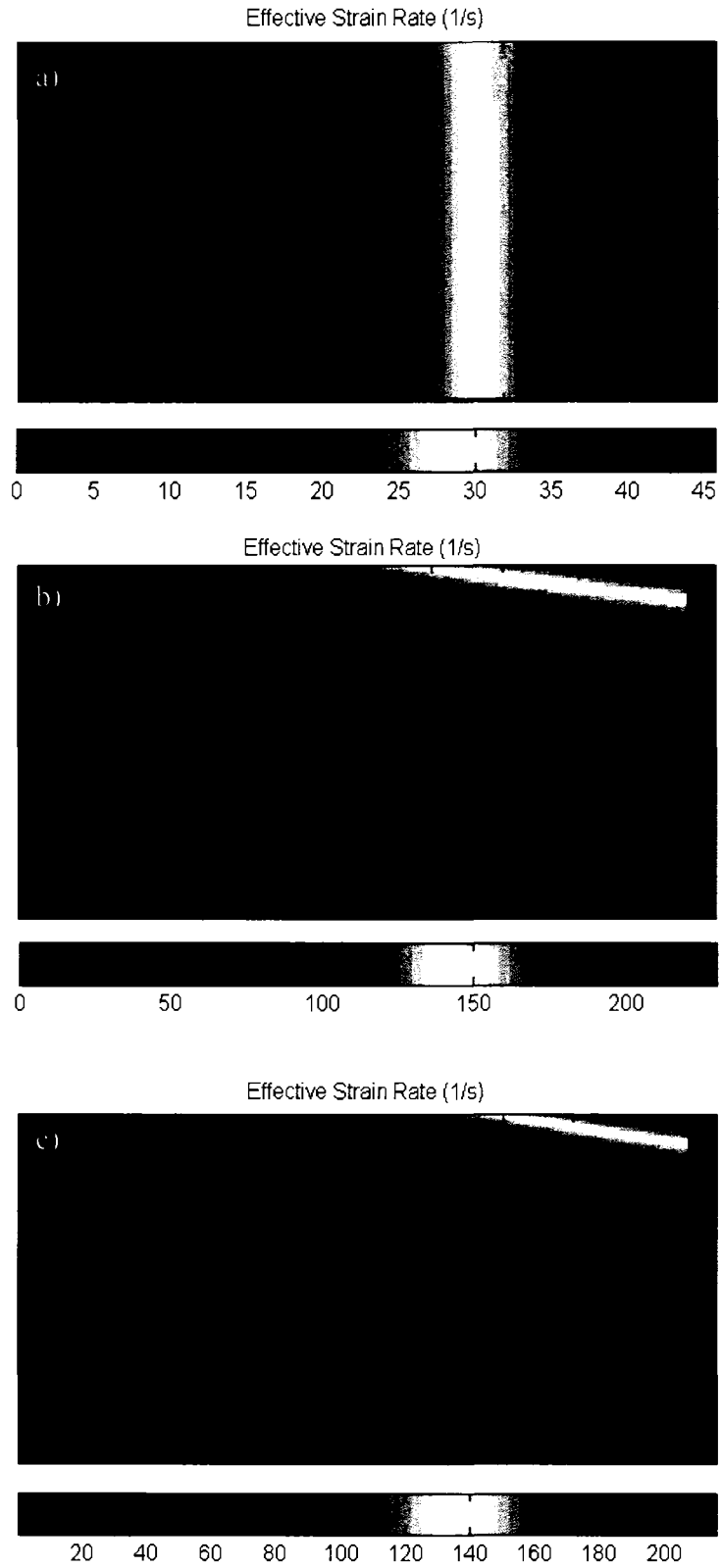


Figure 6- 3 Strain rate distributions for FSP at 400 rpm and 0.847 mm/s a) pin alone b) shoulder alone c) combined shoulder and pin

6.3-2 Rotational and translational speeds effects

The effects of the rotational and translational speeds on the velocity fields and strain rate distributions are shown in *Figures 6-4 and 6-5*. As shown in the figures, the velocity and strain rate increase as the rotational speed increases. The effect of the translational speed however, is negligible, due to the fact that the translational speed is very small compared to the rotational speed. However, this does not mean that the effect of translational speed on the process is negligible. The thermal fields generated during the process were found to be very sensitive to translational as well as rotational speeds [88]. Increasing the rotational speed increases the temperature due to increased heat generation from friction and plastic deformation. On the other hand, increasing the translational speed reduces the exposure time of the material to the generated heat and thus reducing the temperature [82]. Therefore, it is very important to choose the optimal process parameters that ensure generation of enough heat to soften the material in order to achieve large plastic flow while limiting excessive heat to prevent significant grain growth. The current model deals only with the mechanical aspect of the process and must be integrated with a thermal model to accurately describe the process. The development of the thermal model using advanced CFD analysis is currently underway.

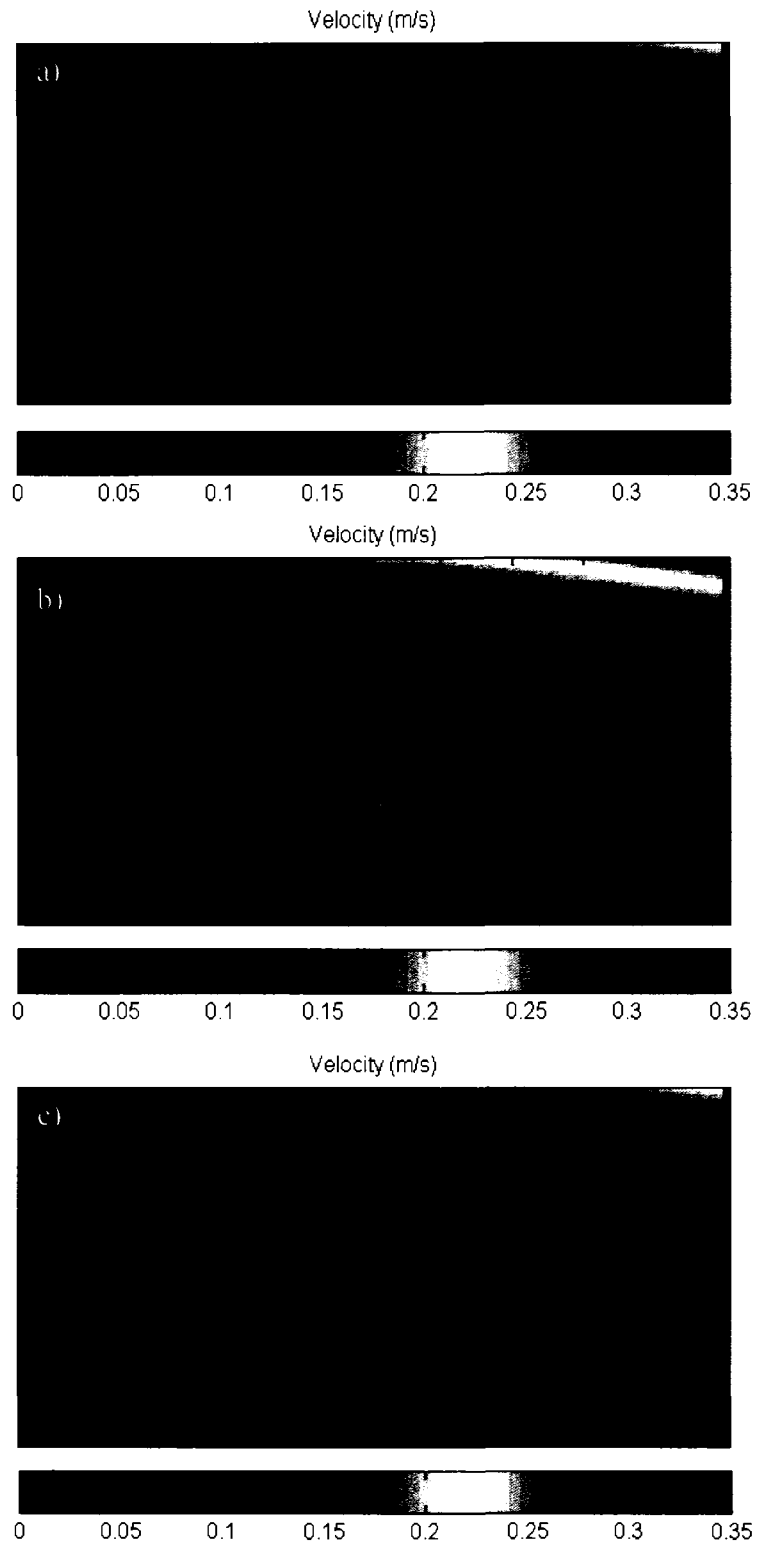


Figure 6- 4 Velocity field for FSP at a) 400 rpm and 0.847 mm/s b) 600 rpm and 0.847 mm/s c) 400 rpm and 2.540 mm/s

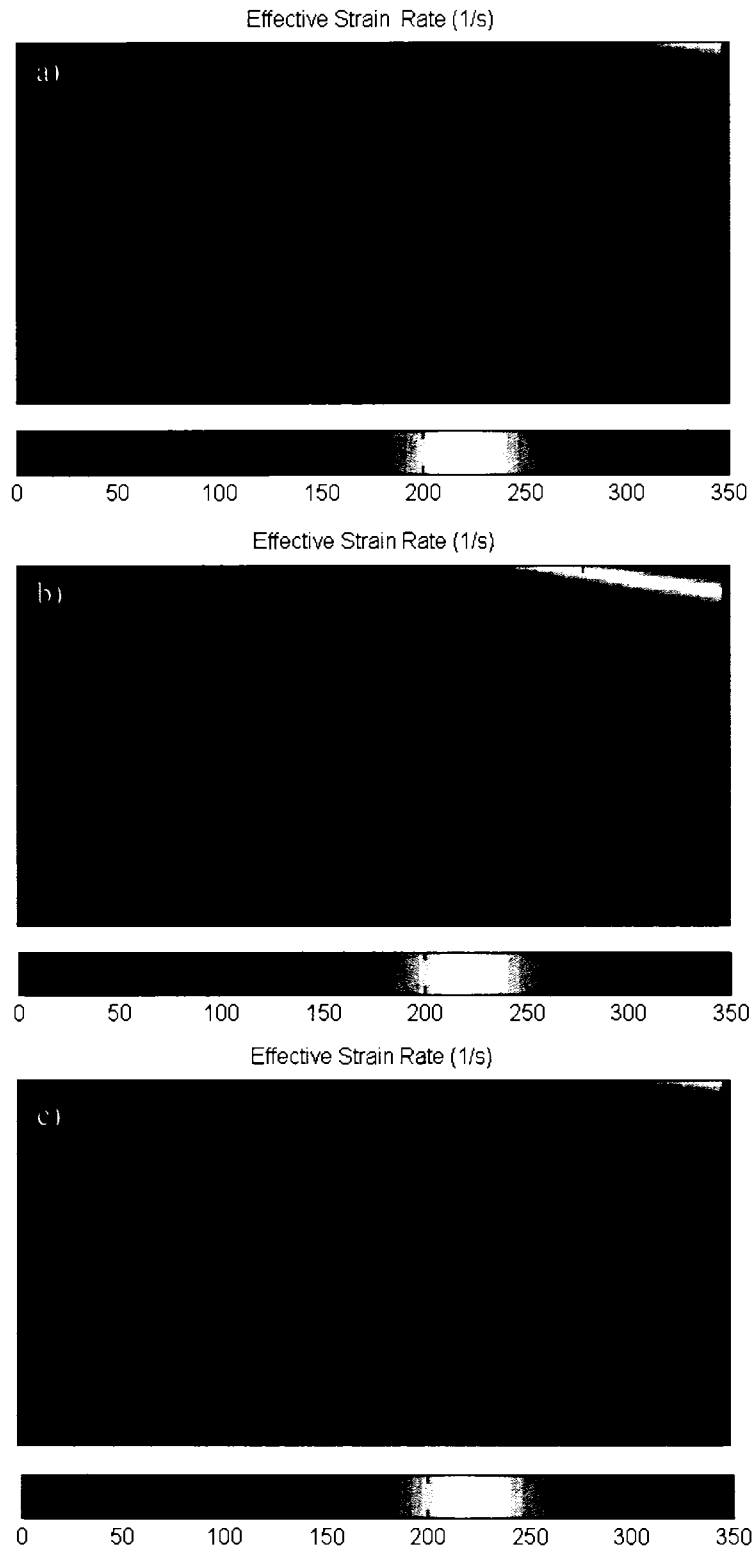


Figure 6- 5 Strain rate distributions for FSP at a) 400 rpm and 0.847 mm/s b) 600 rpm and 0.847 mm/s c) 400 rpm and 2.540 mm/s

6.3-3 Interfacial contact conditions

The contact condition at the shoulder/material and pin/material interfaces (whether they are full sticking, full slipping or partial sticking/slipping) plays a critical role in determining the velocity and strain rate fields. One of the unique features of the proposed model is its ability to accommodate different contact conditions. The contact condition at the interfaces are defined through the constants A and C in the state-variables' equations (Equations 6.1-6.4). *Figures 6-6 and 6-7* show the effect of different contact conditions at the tool/sheet interfaces on the material velocity and strain rate (due to shoulder only). The figures clearly show the ability of the model to capture the actual behavior at different contact conditions. For full sticking, more material flow will result from the shoulder movement when compared to, for example, 50% sticking and 50% slipping. The same results are observed for the effect of contact condition at the pin/material interface on material velocity and strain rate (due to pin only), as illustrated in *Figures 6-8 and 6-9*. *Figures 6-10 and 6-11* show the velocity fields and the strain rate distributions for different combinations of the contact conditions at the two interfaces due to the combined effects of the pin and the shoulder. It is clear that more material flow (more velocity and strain rate) results when the sticking contact conditions exist compared to partial sticking/partial slipping. The results shown in *Figures 6-6 to 6-11* can be very useful in designing the tool and selecting the applied pressure in the thickness direction to control the material flow during FSP.

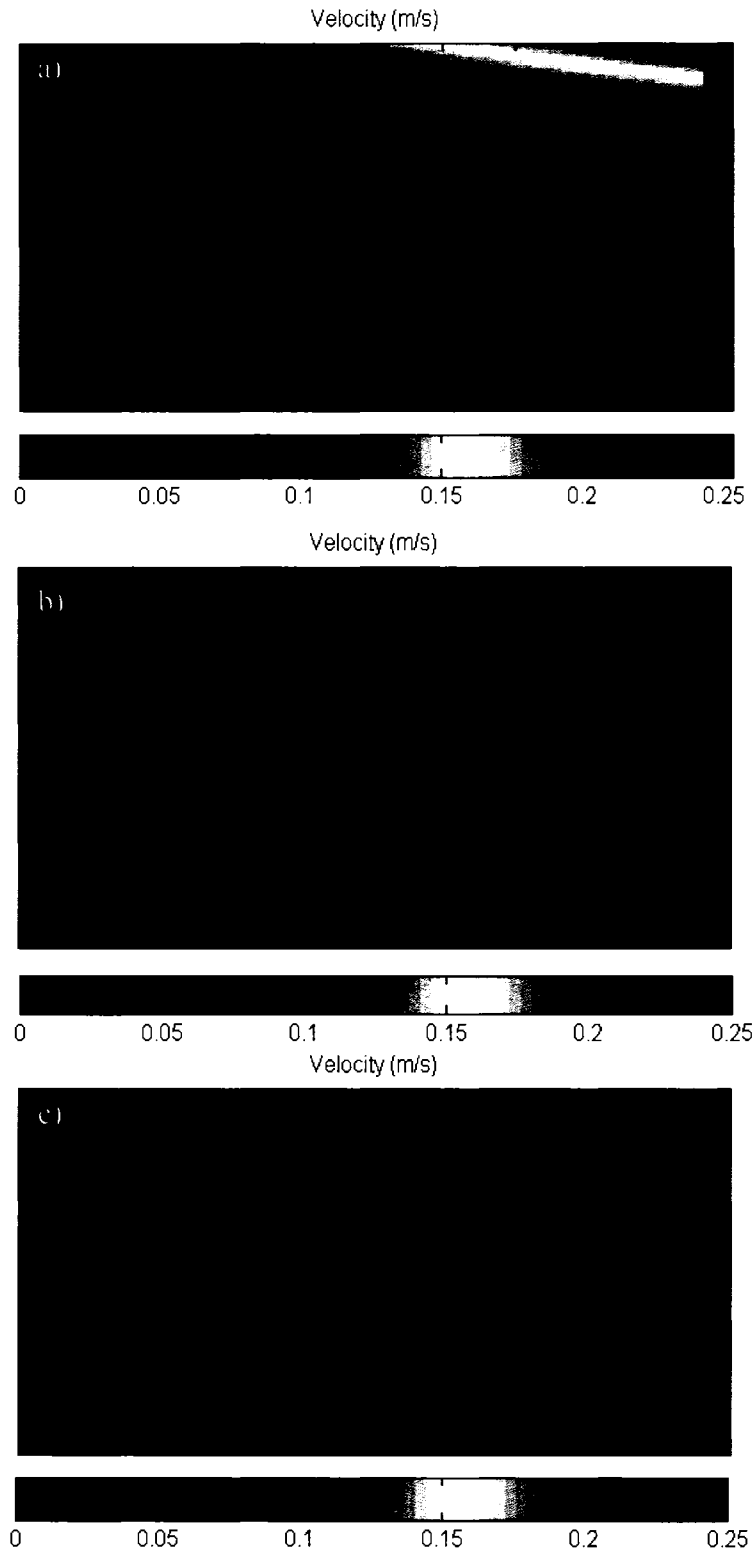


Figure 6- 6 Velocity field for separate shoulder effect scenario (FSP at 400 rpm and 0.847 mm/s) a) full sticking at the shoulder/sheet interface ($A=1.0$), b) 50% sticking at the shoulder/sheet interface ($A=0.5$), and c) 25 % sticking at the shoulder/sheet interface ($A=0.25$)

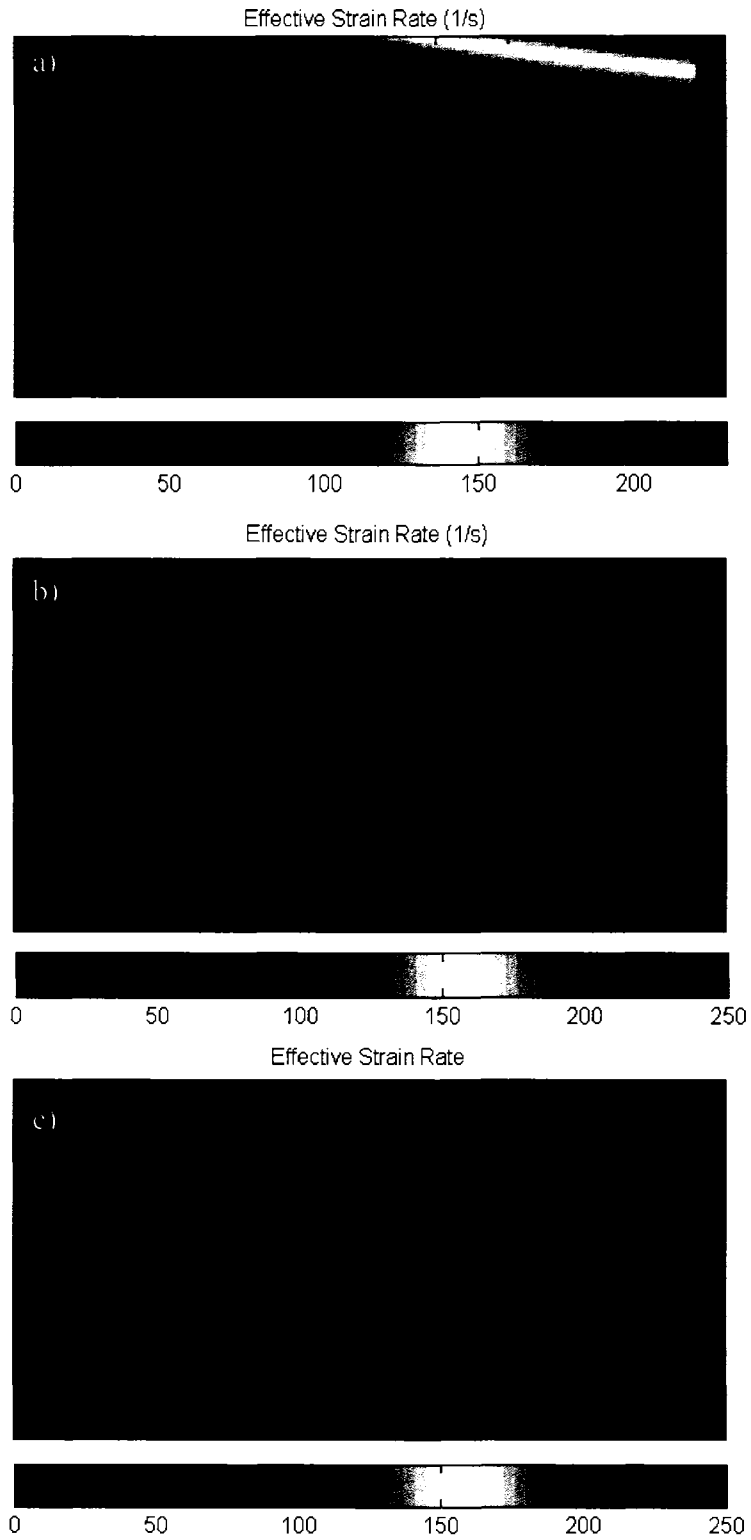


Figure 6- 7 Strain rate distribution for separate shoulder effect scenario (FSP at 400 rpm and 0.847 mm/s) a) full sticking at the shoulder/sheet interface ($A=1.0$), b) 50% at the shoulder/sheet interface sticking ($A=0.5$), and c) 25 % sticking at the shoulder/sheet interface ($A=0.25$)

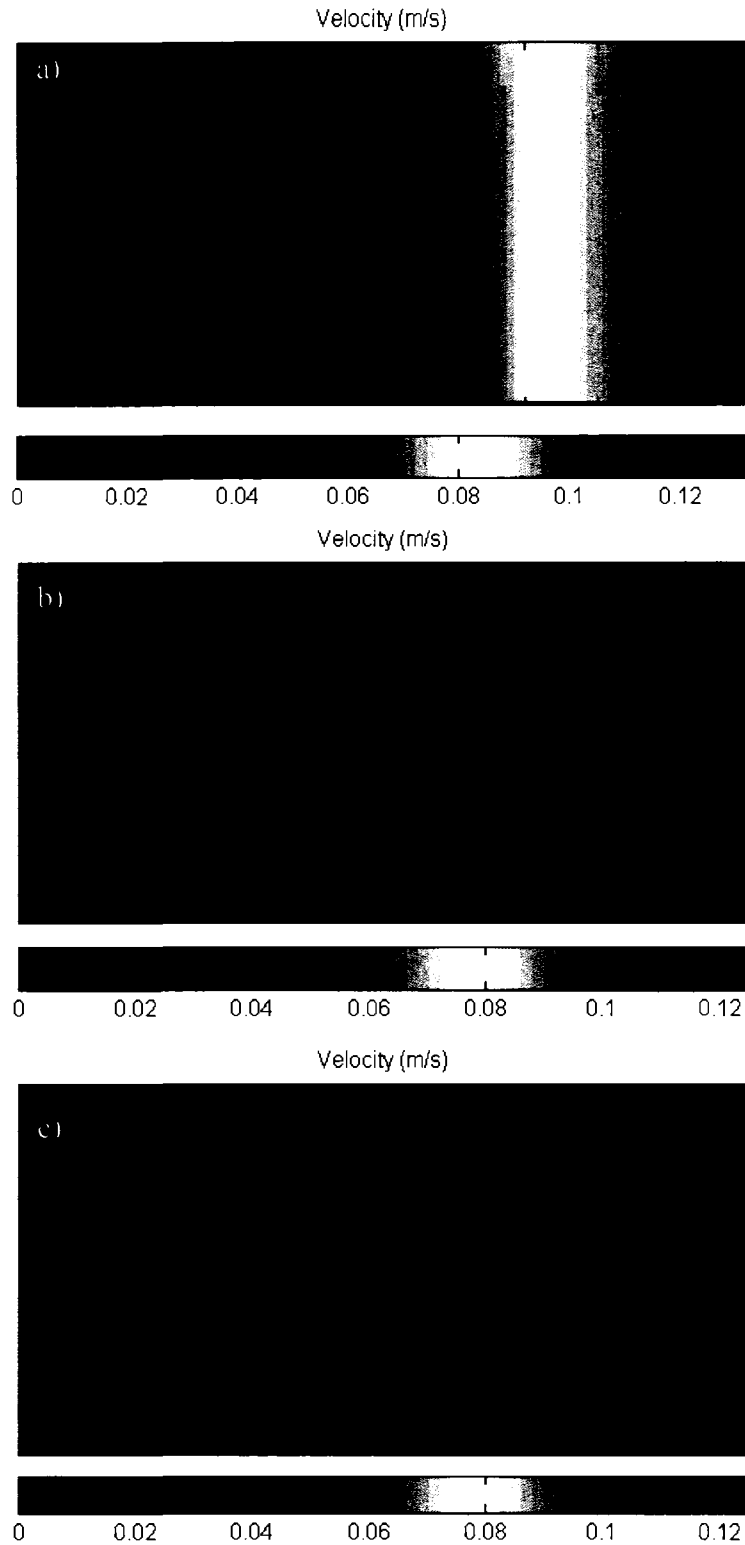


Figure 6- 8 Velocity field for separate pin effect scenario (FSP at 400 rpm and 0.847 mm/s) a) Full sticking at the pin/sheet interface ($C=1.0$), b) 50% sticking at the pin/sheet interface ($C=0.5$), and c) 25 % sticking at the pin/sheet interface ($C=0.25$)

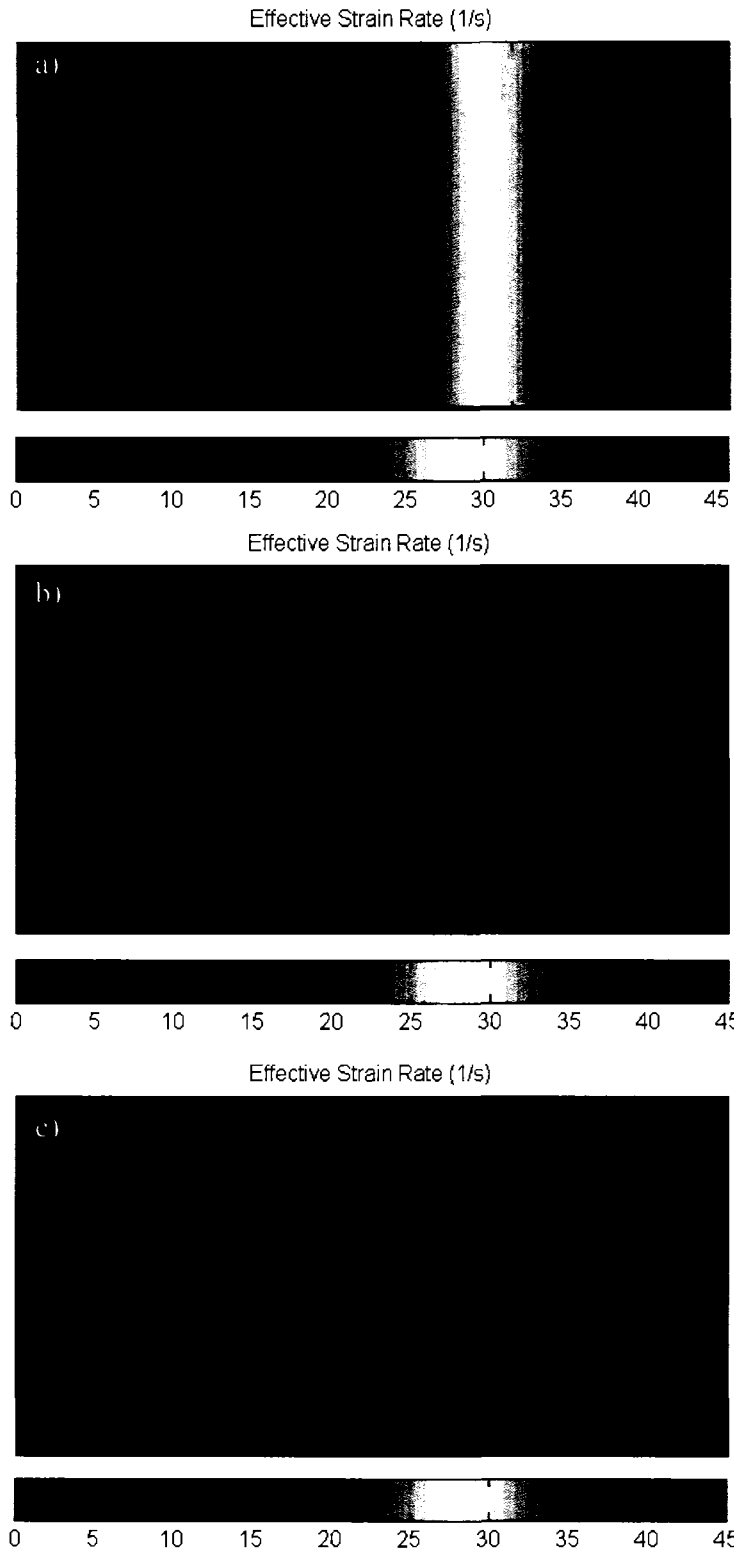
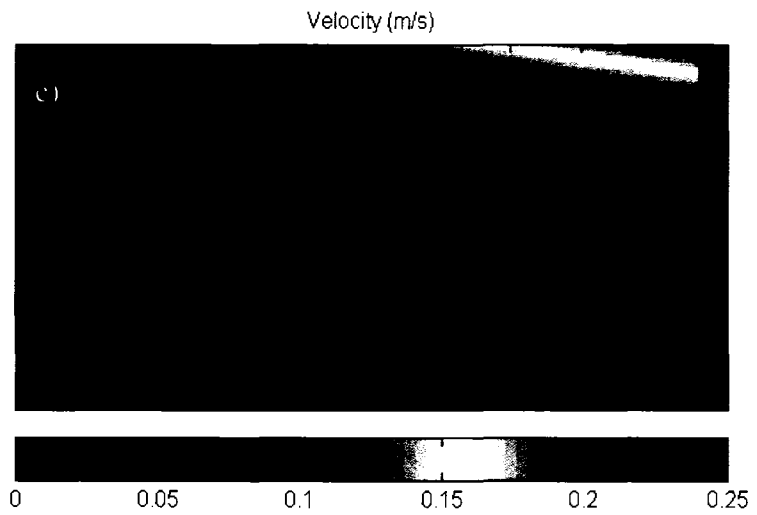
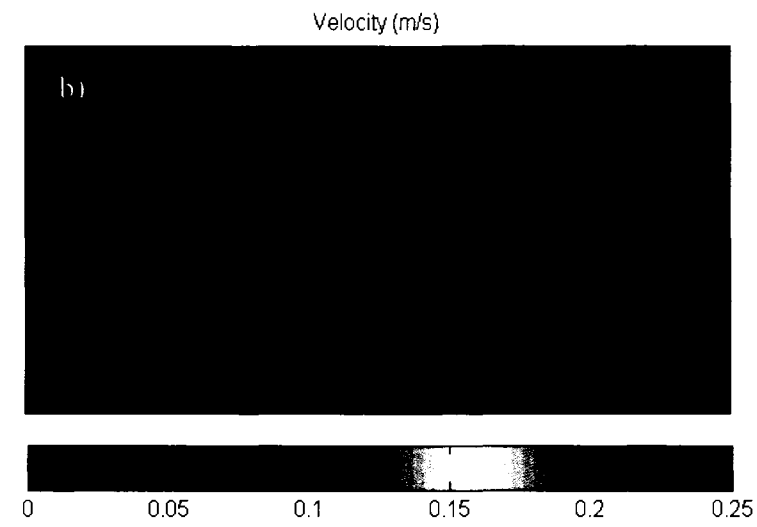
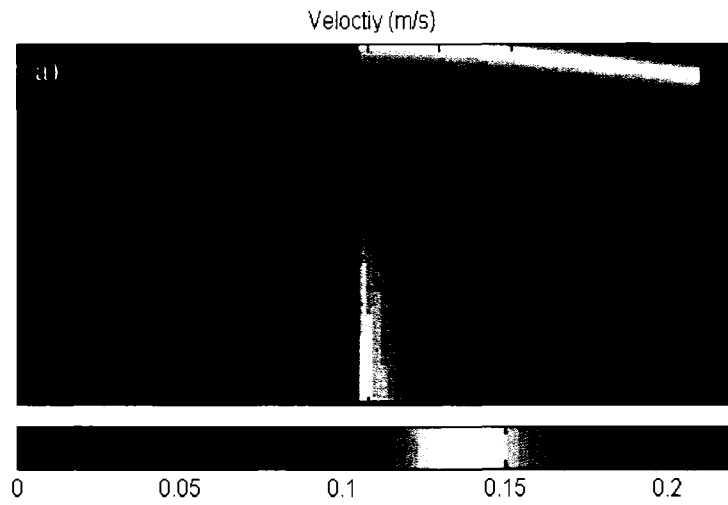


Figure 6-9 Strain rate distribution for separate pin effect scenario (FSP at 400 rpm and 0.847 mm/s) a) full sticking at the pin/sheet interface ($C=1.0$), b) 50% sticking at the pin/sheet interface ($C=0.5$), and c) 25 % sticking at the pin/sheet interface ($C=0.25$)



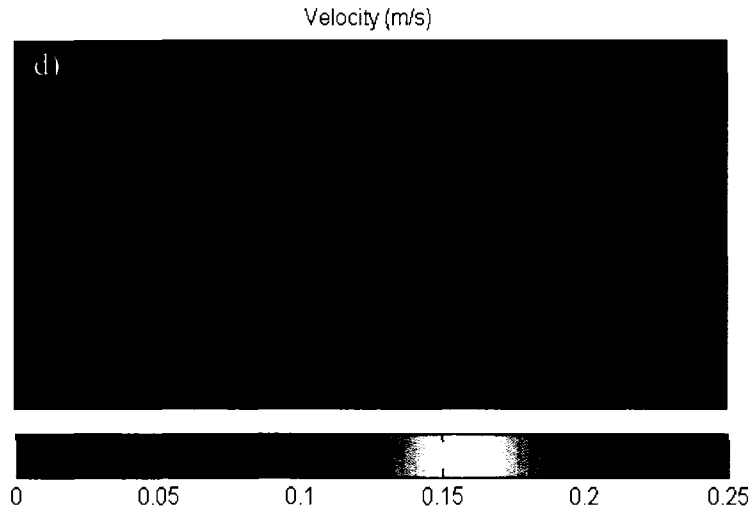
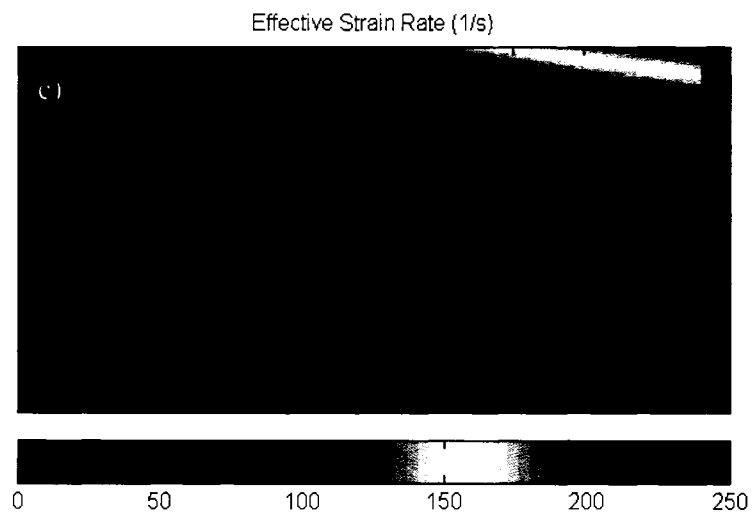
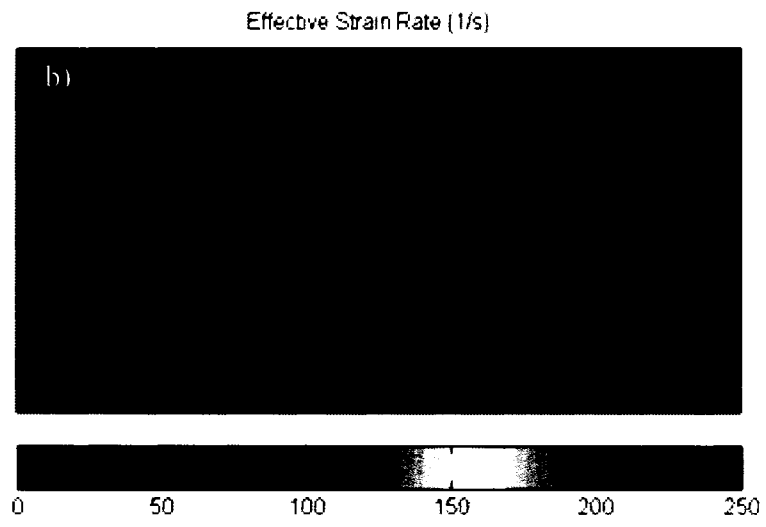
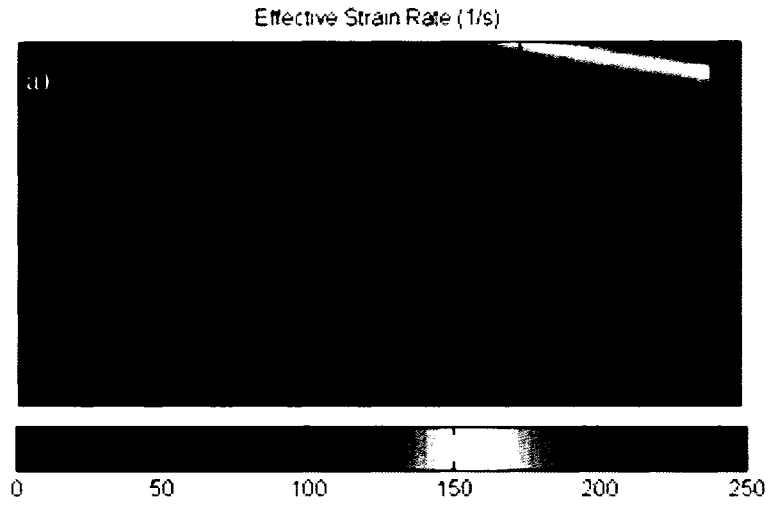


Figure 6- 10 Velocity field for combined shoulder/pin effect scenario (FSP at 400 rpm and 0.847 mm/s) a) full sticking at the shoulder/sheet interface ($A=1.0$) and full sticking at the pin/sheet interface ($C=1.0$), b) 50% at the shoulder/sheet interface sticking ($A=0.5$) and full sticking at the pin/sheet interface ($C=1.0$), c) full sticking at the shoulder/sheet interface ($A=1.0$) and 50% sticking at the pin/sheet interface ($C=0.5$), and d) 50% sticking at the shoulder/sheet interface ($A=0.5$) and 50% sticking at the pin/sheet interface ($C=0.5$)



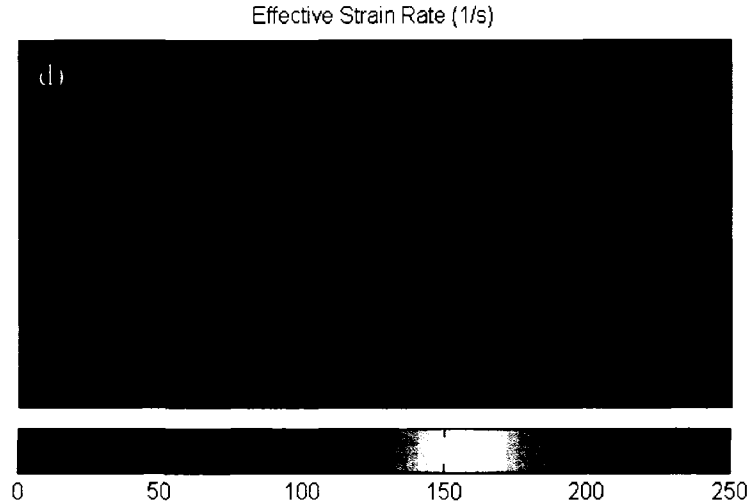


Figure 6- 11 Strain rate distribution for combined shoulder/pin effects scenario (FSP at 400 rpm and 0.847 mm/s) a) full sticking at the shoulder/sheet interface ($A=1.0$) and full sticking at the pin/sheet interface ($C=1.0$), b) 50% at the shoulder/sheet interface sticking ($A=0.5$) and full sticking at the pin/sheet interface ($C=1.0$), c) full sticking at the shoulder/sheet interface ($A=1.0$) and 50% sticking at the pin/sheet interface ($C=0.5$), and d) 50% sticking at the shoulder/sheet interface ($A=0.5$) and 50% sticking at the pin/sheet interface ($C=0.5$)

6.3-4 Tool geometry (Pin diameter/Shoulder diameter ratio)

Tool geometry is a very important aspect of FSP which has to be carefully chosen in order to get the optimum outcomes. The current model can be utilized to investigate the effect of changing the tool geometry on the strain rate distribution and consequently the resulting structure. In this section the effect of pin radius to shoulder radius ratio (r_p/r_s) is investigated using the current model. *Figures 6-12 and 6-13* show the velocity fields and the strain rate distributions for FSP using tools with different (r_p/r_s) ratios.

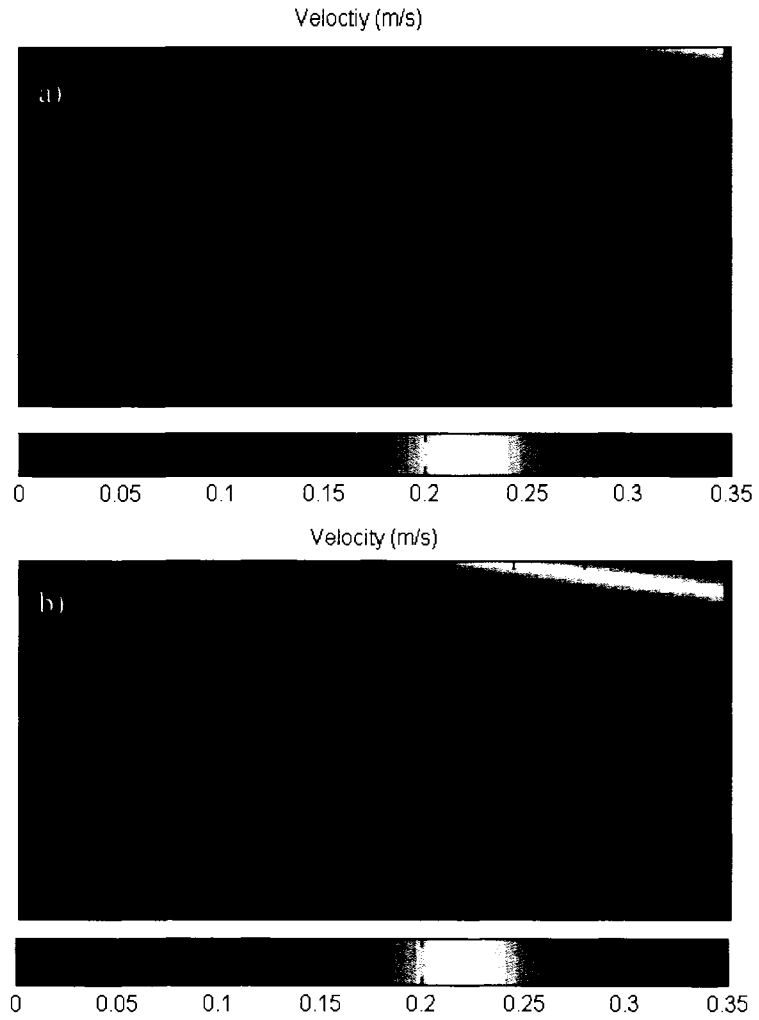


Figure 6- 12 Velocity fields for different (r_p/r_s) ratios (FSP at 400 rpm and 0.847 mm/s)
 a) (r_p/r_s) = 1/2, and b) (r_p/r_s) = 1/3

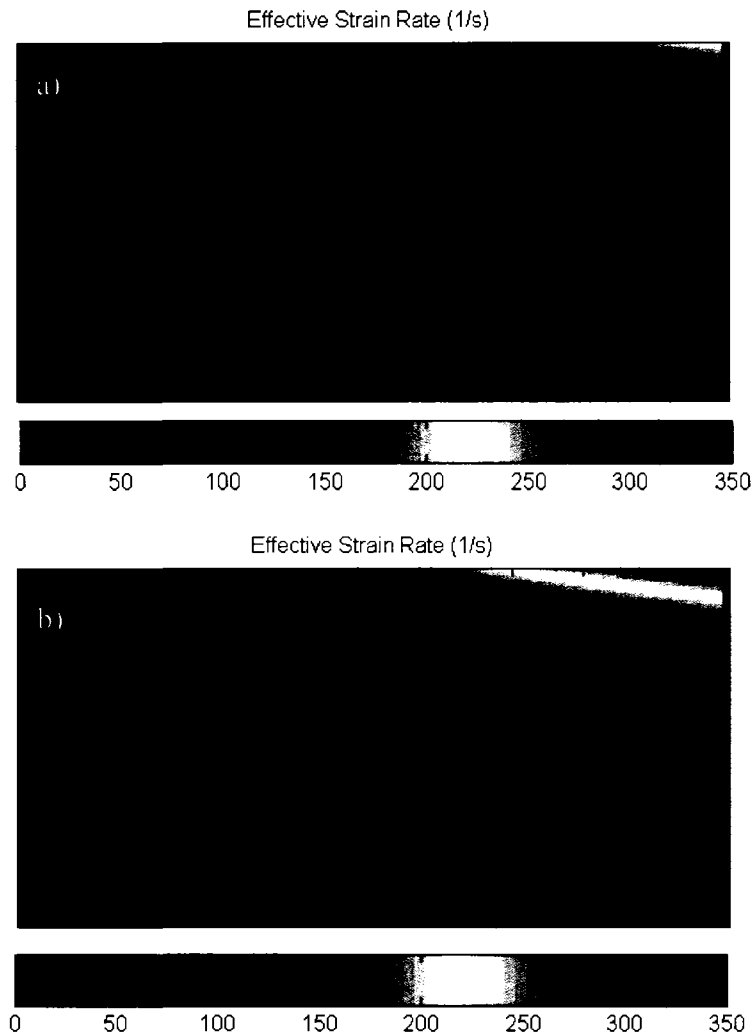


Figure 6- 13 Effective strain rate distribution for different (r_p/r_s) ratios (FSP at 400 rpm and 0.847 mm/s) a) (r_p/r_s) = 1/2, and b) (r_p/r_s) = 1/3

6.3-5 Validation of current results

The preceding paragraphs show that the proposed model is capable of capturing the effects of various process parameters on the material flow during FSP. The shape of the deformation zone is another important piece of information that can be predicted using the proposed model. *Figure 6-14* shows the velocity field in the processed zone. The deformation field is directly related to the velocity field. Hence, one can predict the

shape of the deformation fields from the velocity fields. The shape of the deformation field shown in *Figure 6-14* is in excellent agreement with the shapes of experimentally determined deformation fields reported in the literature (see for example Ericsson et al. [84] and Hassan et al. [85] (*Figure 6-15*)).

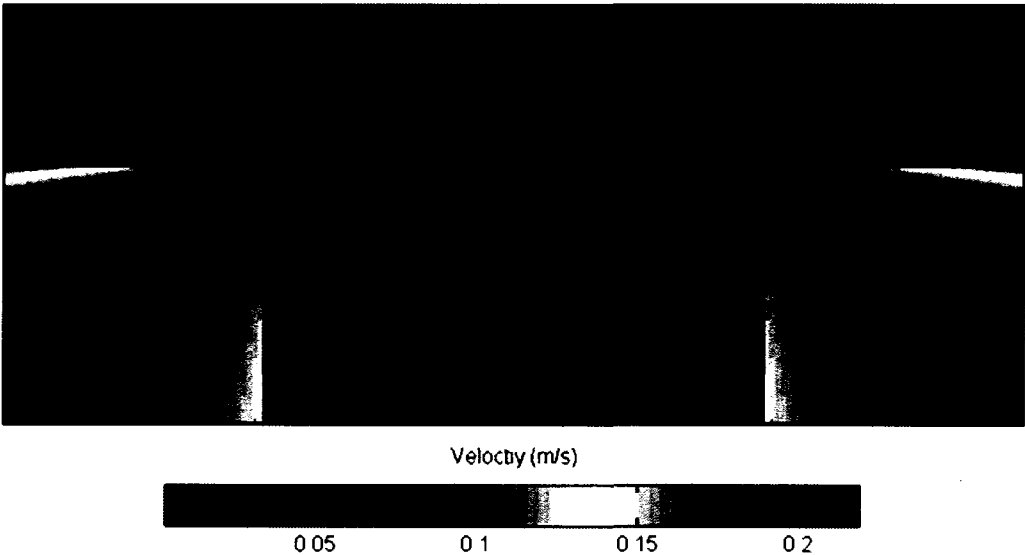


Figure 6- 14 Predicted shape of the deformation zone (Velocity field for FSP at 400 rpm and 0.847 mm/s)

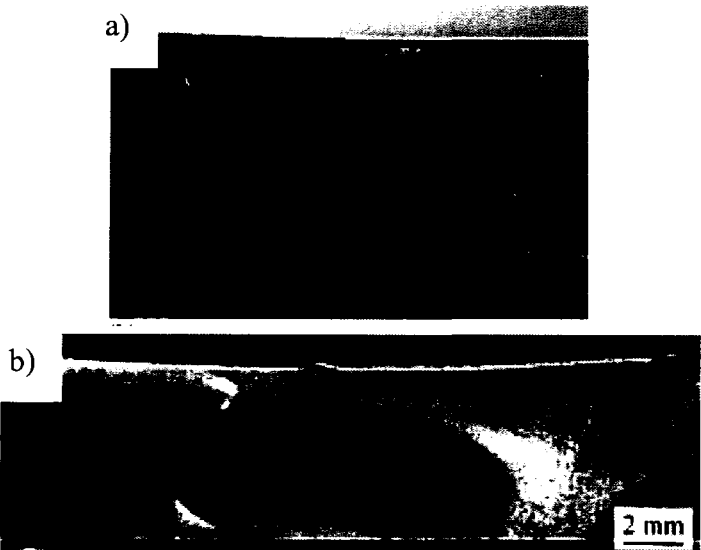


Figure 6- 15 Macrostructure of FS processed zone (a) Ericsson et al. [84] and (b) Hassan et al. [85].

6.4 Conclusions

The proposed model is capable of predicting the velocity fields and the strain rate distributions within the processed zone of a friction stir processed material in terms of the process parameters. The model allows examining the effects of different parameters such as: shoulder and pin, rotational and translational speeds, and different interfacial contact conditions. The obtained velocity and strain rate values are in agreement with reported values in the literature. In addition, the model can successfully capture the shape of the deformation field. The current model deals only with the mechanical aspects of the process and can serve as a first step towards developing a comprehensive model that also includes the thermal aspects of the process. Such a comprehensive model can be used to predict the resulting microstructure during FSP.

Chapter Seven

CFD SIMULATION

7. CFD SIMULATION

This chapter presents numerical simulation of FSP using the CFD code; STAR-CCM+. The chapter starts with an overview of previous publications in the field. The capabilities and special features of the CFD code (STAR-CCM+) are discussed, and the governing equations used by STAR-CCM+ are stated. A detailed description of the current model; geometrical aspects, assumptions, initial and boundary conditions are also discussed. The overall objective of the CFD simulations is to determine the velocity fields during FSP for different rotational and translational speed combinations and compare the results with those determined using the analytical model discussed in Chapter 6.

7.1 Previous Work

Some researchers used computational fluid dynamics to simulate FSP; they assumed the FS processed material to be a fluid, and used different CFD codes to determine velocity fields, material flow and temperature distributions. The following paragraphs review some of the work that has been done in numerical simulation of friction stirred materials (FSW and FSP).

Zhang et al. [86] simulated the material flow during FSW using the finite element method based on nonlinear continuum mechanics. In their work they used Lagrangian-Eulerian formulation and adaptive remeshing. They used both; slipping interface and

frictional contact models. The temperature-dependent material properties are defined explicitly while a rate-independent elastic-plastic material is used. In their work they increased the speeds by 1000 times to accelerate the converging, while keeping the rotational to translational speed ratios the same as the actual ones. Their results showed that the maximum material velocity was increased by increasing the translational and angular velocities, and that a correlation between the equivalent plastic strain and microstructure existed.

Xu et al. [72] used the non-linear FE package ABAQUS to simulate heat generation due to the tool shoulder-workpiece and pin-workpiece interactions, and the heat loss through air and anvil. A half-scale model was used with temperature-dependent thermophysical properties. In their work, they imposed heat flux to simulate the generated heat by the shoulder, while different film coefficients were specified on the outer surface to simulate the heat loss through air and anvil. Their results suggested that both the shoulder and the pin contributed to the heat generated during FSW.

Colegrove and Shercliff [87] used a two dimensional computational fluid dynamics (CFD) code, FLUENT to simulate the flow during FSW. They used a slip model by specifying shear stress at the boundary. They divided the model into two regions; the first one is around the tool and has the same rotational speed as the tool, and the second region is presented as a surrounding stationary region. All boundary walls are modeled to have velocity equal to the welding speed. Their work aimed at comparing the material flow during FSW for different tool profiles (four different tool profiles were

evaluated). The results suggested that using the slip model gave useful information about where the material was likely to stick to the tool, and captured different material flow patterns for different tool profiles.

Schmidt and Hattel [88] used FEMALB FE software to model the process using 2D CFD. Eulerian formulation was used in their flow modeling. They used the power law shear strain rate-shear stress relationship to describe aluminum behavior at high shear rates. The material is described to be an incompressible fluid with a shear rate dependant viscosity. For the sliding condition, the generated heat was due to friction; while for the sticking condition, it was due to plastic or viscous dissipation. Their results suggested that changing the exponent of the power law relation affected the velocity field and the shear layer, and that the streamlines through the shear layer were used to identify the border between the rotation and translation zones.

Long et al. [89] used a simple 2D CFD model to simulate the FSW process. They used the CFD code, FLUENT. Adiabatic tool/fluid boundary assumption was used where the heat conduction by the tool away from the plate is negligible. The effects of viscosity and thermal conductivity on the flow pattern were investigated and they were related to defects formation in FSW. However such simple 2D model was not sufficient to provide predictions for tool design and machine specifications.

In general, most of the CFD work that has been done to simulate FSP or FSW use two dimensional models, and neglect the dependency of material properties on either

temperature or strain rate or both. Still there is a great need for a comprehensive 3D model which can accurately simulate the actual FSP/FSW process where: the material properties are temperature and strain rate dependent, both rotational and translational movements are specified at the same time, different interfacial contact conditions are considered, and all types of heat generated and losses are considered (frictional heat, heat generated due to plastic deformation, heat losses to air and anvil etc.).

7.2 STAR-CCM+ CFD Code

The CFD simulation code used in this work is STAR-CCM+, which uses computational continuum mechanics algorithms (hence the name Computational Continuum Mechanics, or CCM). Different parts of the solution domain can be linked to fluid or solid continua models. It is different from most other solvers in that it separates the simulation physics from the computational grid. In other words, the grid is used only to define the topology of the problem. Generalized interfaces can be created to join topologically different grids together [90].

STAR-Design Version 4.02 [91] is used for preprocessing of the simulations, which includes creating the geometries required for simulation. Three main bodies are considered; tool shoulder, tool pin and the sheet. Also two interfaces are created; one is the shoulder/material interface, and the other is the pin/material interface

The geometries that have been created using STAR-Design are then imported into STAR-CCM+ code to conduct the simulation. In this stage the continua, regions, interfaces and materials' properties have to be defined. One of the great features of this code is the ability to define both rotational and translational motions at the same time. In this work two types of rigid body motions have been defined; one is the rotation of the tool around its axis, and the other one is the translational motion of the sheet with reference to the tool.

After that, initial and boundary conditions have to be defined, based on experiments and some simplifying assumptions. Another important feature of STAR-CCM+ code is the ability to define boundary conditions and the material properties through user-defined functions, which allows for greater flexibility.

The simulation is based on solving the continuity, momentum and energy equations. STAR-CCM+ different approaches (segregated or coupled) can be chosen to solve the momentum, continuity and energy equations [90]. Segregated approaches solve the equations separately; however coupled approaches solve them instantaneously. The segregated approach is simpler and uses less memory; however, the coupled algorithm yields more robust and accurate solutions. For this work the segregated approach is used for simplicity. The basic formulation for the segregated algorithms is shown in Equations 7.1-7.3 (momentum, continuity and energy equations in their discrete form) [90]:

$$\frac{\partial}{\partial t}(\rho \mathbf{v} V)_0 + \sum_f [\mathbf{v} \rho (\mathbf{v} - \mathbf{v}_g) \cdot \mathbf{a}]_f = - \sum_f [p \mathbf{I} \cdot \mathbf{a}]_f + \sum_f \mathbf{T} \cdot \mathbf{a} \quad (7.1)$$

$$\sum_f \dot{m}_f = \sum_f [\dot{m}_f^* + \dot{m}_f'] = 0 \quad (7.2)$$

$$\left(\rho C_p V \frac{\partial T}{\partial t} \right)_0 + \sum_f \left[\left\{ \rho H (\mathbf{v} - \mathbf{v}_g) + \dot{\mathbf{q}} \cdot \mathbf{a} - (\mathbf{T} \cdot \mathbf{v}) \right\} \cdot \mathbf{a} \right]_f = 0 \quad (7.3)$$

Where t is the time, ρ is the density, \mathbf{v} is the velocity, V is the cell volume, 0 is the cell-0 quantity, f is the face value, \mathbf{v}_g is the grid velocity, \mathbf{a} is face area vector, p is the pressure, \mathbf{I} is the identity matrix, \mathbf{T} is the viscous stress tensor, \dot{m}_f is the face mass flow, \dot{m}_f^* is the uncorrected face mass flow rate, \dot{m}_f' is the mass flow correction, C_p is the heat capacity, T is the temperature, H is the total enthalpy, and $\dot{\mathbf{q}}$ is the heat flux vector.

7.3 Model Description

The model consists of two bodies; the first one is the tool which is assumed to be a rigid solid body made of steel, the second one is the sheet which is assumed to be liquid that has aluminum properties. The tool is defined to have a rigid body motion where it is rotating around its axis with the desired rotational speed (ω (rpm)). While the sheet is defined to have a moving reference frame motion with the desired translational velocity (v (m/s)). Three-dimensional model with constant density and steady state conditions,

using the segregated solid energy method, is applied to the tool. For the sheet the segregated flow method is used. The assumptions which have been made are: constant density, constant dynamic viscosity, and laminar flow and steady state conditions for the sheet. The current analysis is a simplified one, and more accurate and advanced analysis would require coupling both the mechanical and thermal aspects of the process, and defining the dynamic viscosity and the density as functions of temperature and strain rate as encountered in actual friction stirring of materials.. An interface between the tool and the sheet has been created, and it is assumed that each point on it has the same velocities as its corresponding point on the tool (Figure 7-1 shows the model's geometry).

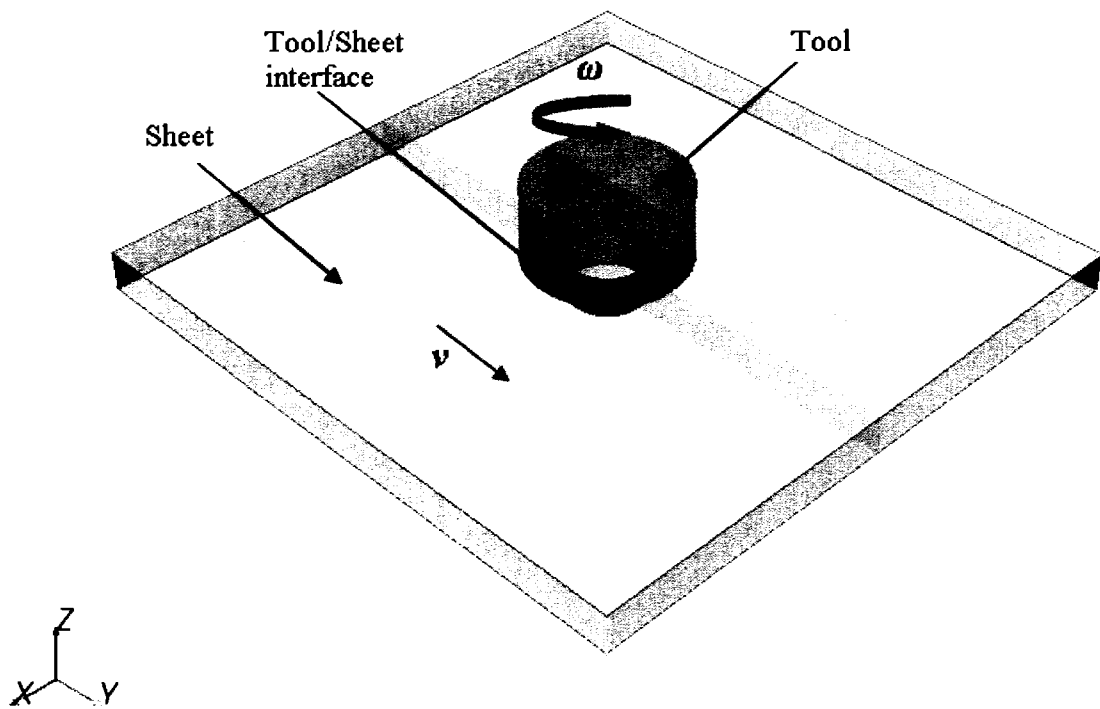


Figure 7- 1 Model's geometry.

Figure 7-2 shows the meshed geometries of the model; polyhedral mesh is used in this work, it provides a balanced solution for complex mesh generation problems. They are relatively easy and efficient to build, requiring no more surface preparation than the equivalent tetrahedral mesh. They also contain approximately five times fewer cells than a tetrahedral mesh for a given starting surface [90]. The polyhedral meshing model utilizes an arbitrary polyhedral cell shape in order to build the core mesh. The polyhedral cells created typically have an average of 14 cell faces [90]. In this simulation the numbers of cells and nodes are as follows: 3002 cells and 18222 nodes for the tool, and 37491 cells and 168662 nodes for the sheet.

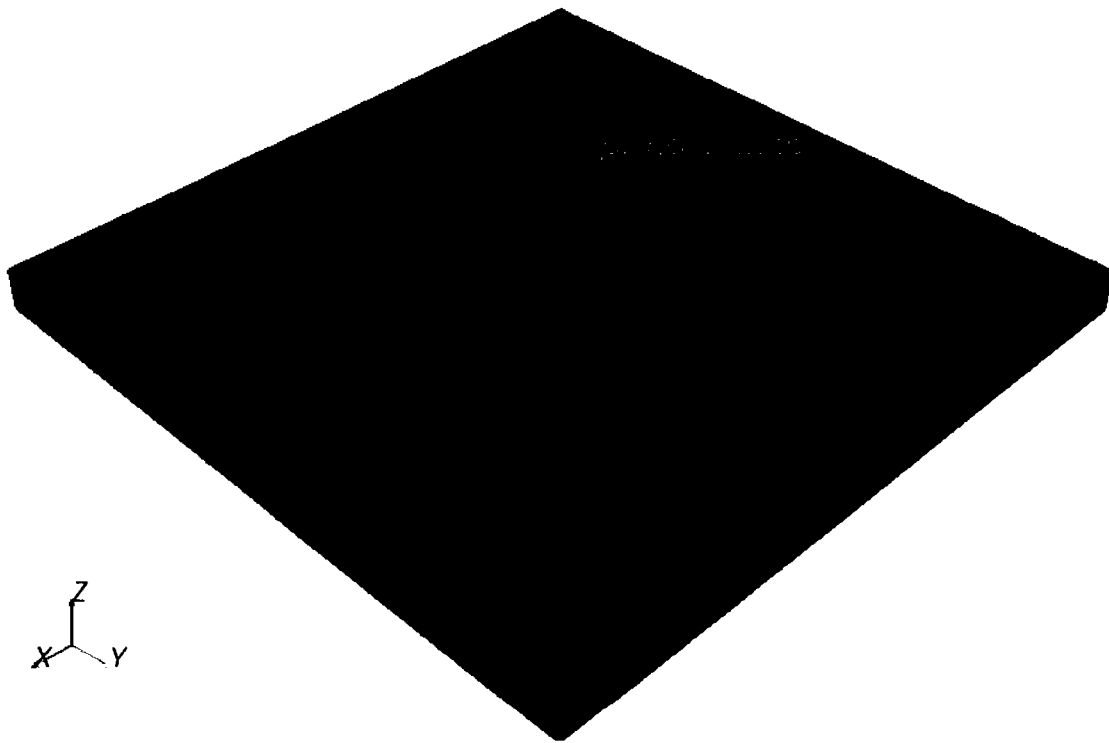
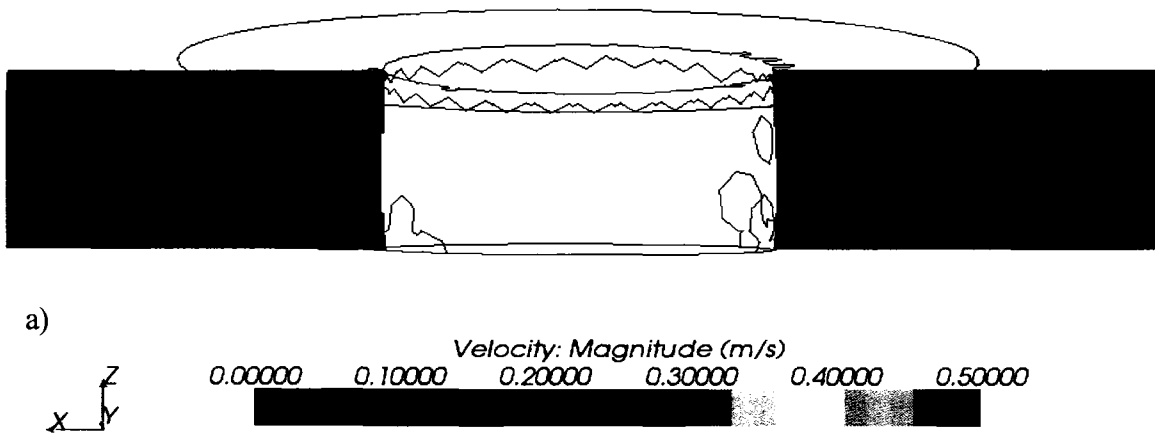


Figure 7- 2 Meshed geometry.

7.4 Results and Discussions

Figure 7-3 shows the velocity fields within a traverse section of the FS processed zone during FSP at different combinations of rotational and translational speeds. To investigate the effect of rotational speeds on velocity fields, FSP at three different rotational speeds (400, 600 and 800 rpm) and at a constant translational speed (0.847 mm/s) have been simulated. As shown in *Figure 7-3*, as the rotational speed increases the material's velocity within the processed zone increases. Such observation is in agreement with the literature [49] and with the results obtained used the analytical model presented in *Chapter Six*.



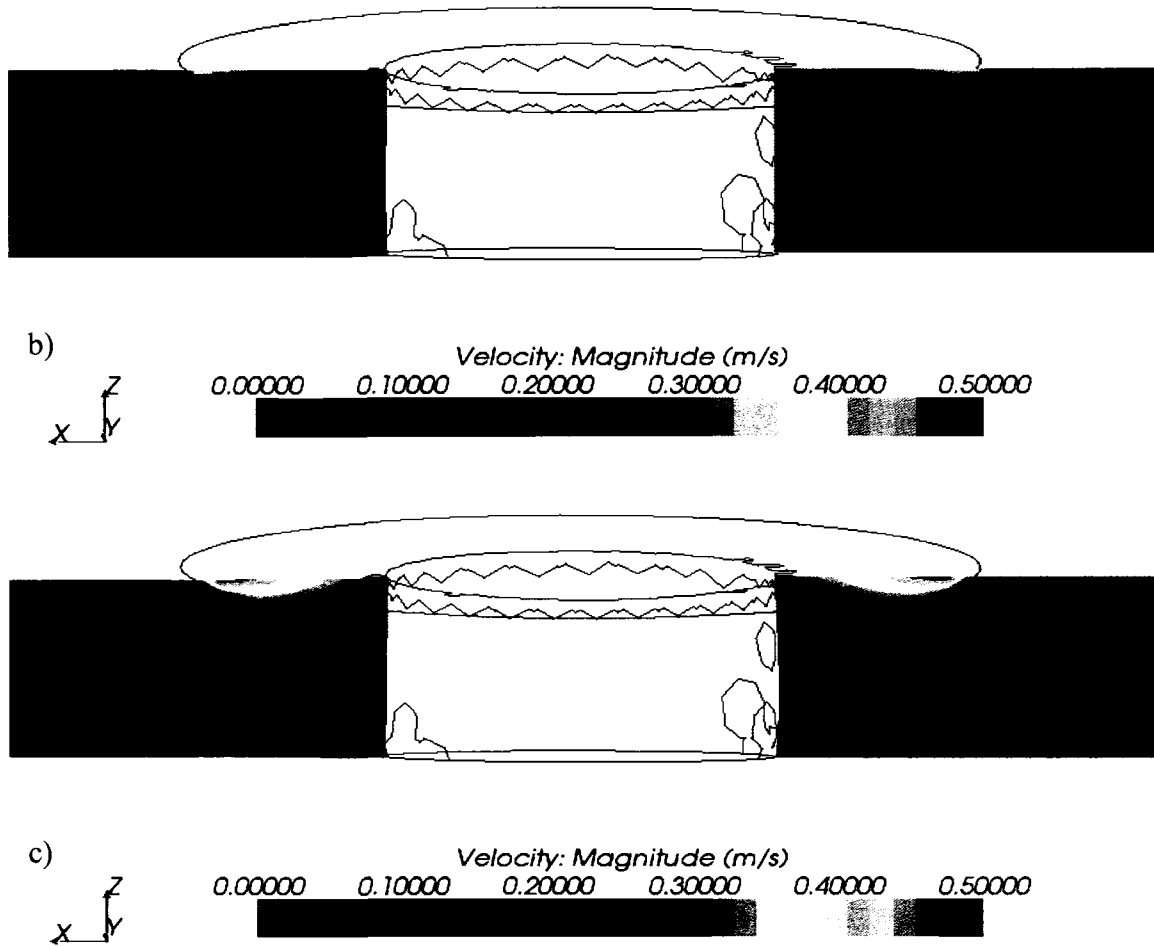


Figure 7- 3 Effect of rotational speed on the velocity field of a traverse section of FS processed zone; a) FSP at 400 rpm and 0.847 mm/s, b) FSP at 600 rpm and 0.847 mm/s, and c) FSP at 800 rpm and 0.847 mm/s).

To investigate the effect of the translational speed, the rotational speed is kept constant (400 rpm) while varying the translational speed (0.847 and 2.541 mm/s). And again as the analytical model results indicated; the effect of translational speed on velocity fields is negligible when it is compared to the rotational speed's effect (see *Figures 7-6 and 7-7*). However, as discussed before in *Chapters Five and Six*, this does not mean that the effect of translational speed on the process is negligible. The thermal fields generated during the process were found to be very sensitive to translational as well

as rotational speeds [88]. So it is very important to integrate the mechanical and thermal aspects to accurately describe the process.

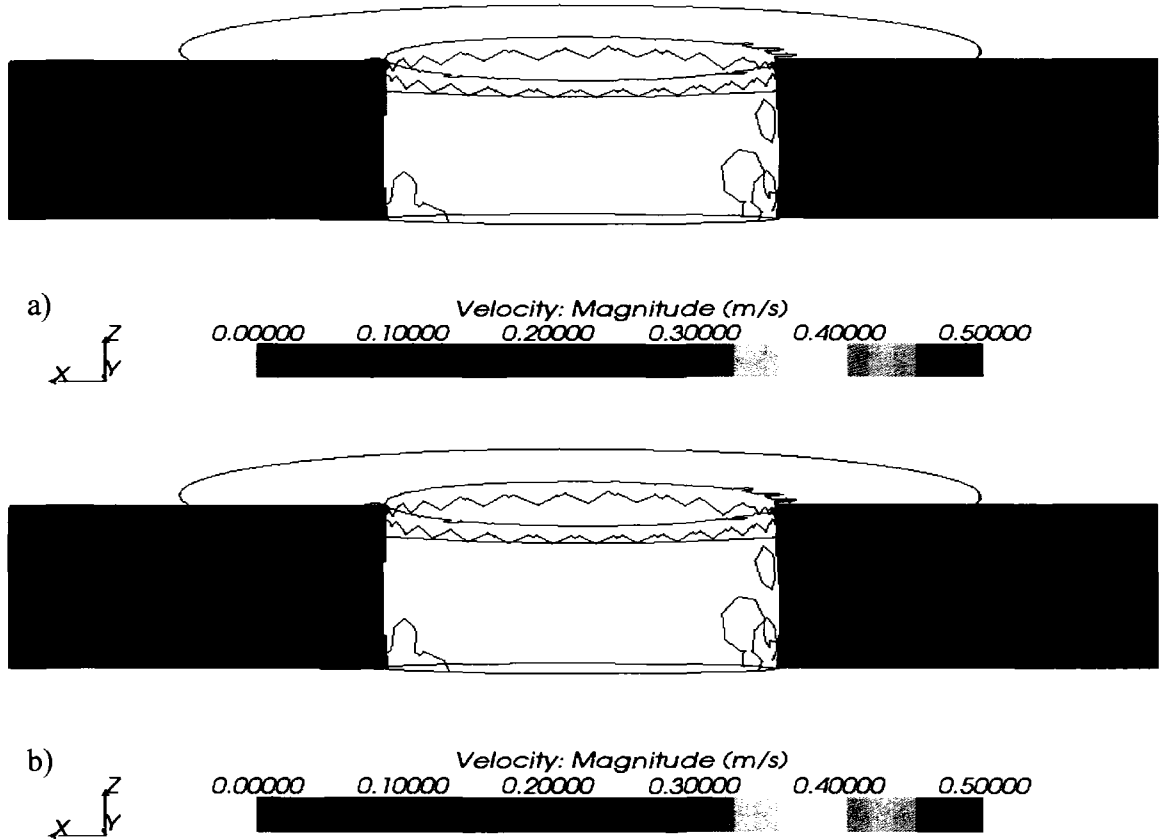


Figure 7- 4 Effect of translational speed on the velocity field of a traverse section of FS processed zone; a) FSP at 400 rpm and 0.847 mm/s and b) FSP at 400 rpm and 0.847 mm/s.

The CFD results show good agreement with those obtained using the analytical model (see *Chapter Six*) in terms of values, location of the maximum velocity (at the contact with the outer edge of the shoulder) and the shape of the deformation zone. *Figure 7-5* shows the velocity fields using both the CFD simulation and the analytical model proposed in *Chapter Six*. *Figure 7-6* shows the relation between the maximum

processed material's velocity and the rotational speed using both CFD analysis and analytical modeling. *Figure 7-7* shows relation between the processed material's velocity and the radial distance at the middle of the sheet thickness within the processed zone using both CFD and analytical model. Again the results show good agreement between the CFD analysis and the analytical model presented in chapter 6.

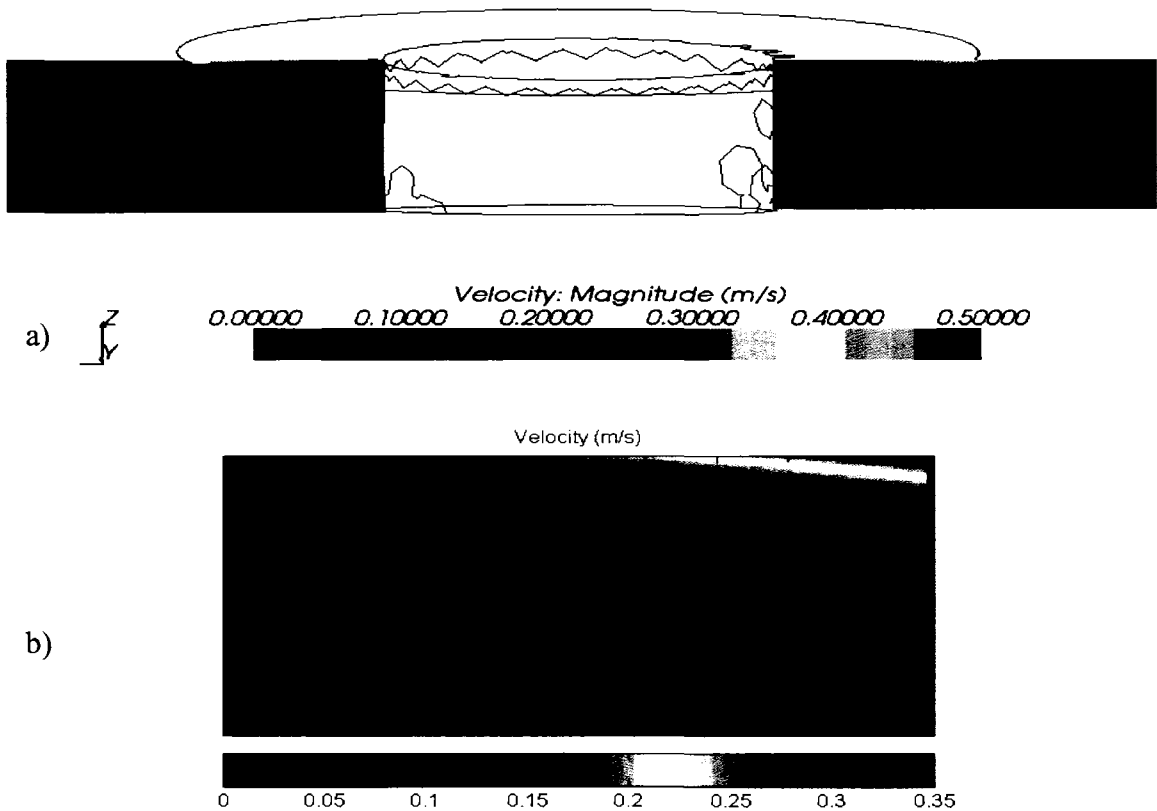


Figure 7- 5 Velocity fields of a traverse section of FS processed zone (FSP at 600 rpm and 0.847 mm/s), using a) CFD analysis, and b) analytical model proposed in Chapter Six).

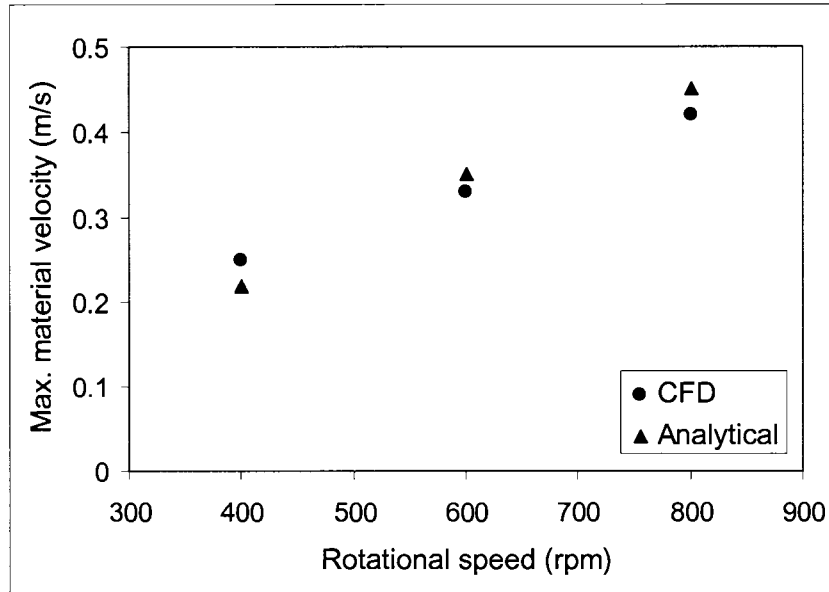


Figure 7- 6 Maximum material's velocity at different rotational speeds using both CFD analysis and analytical model presented in chapter 6.

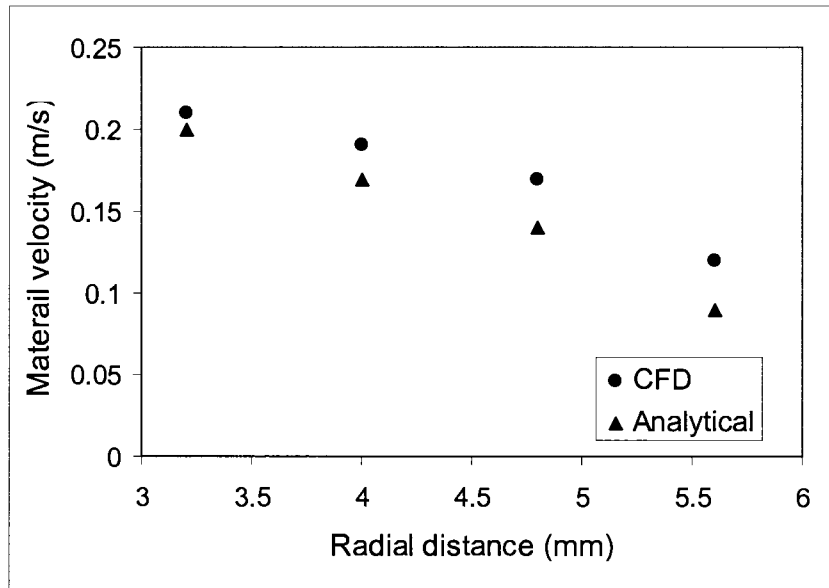
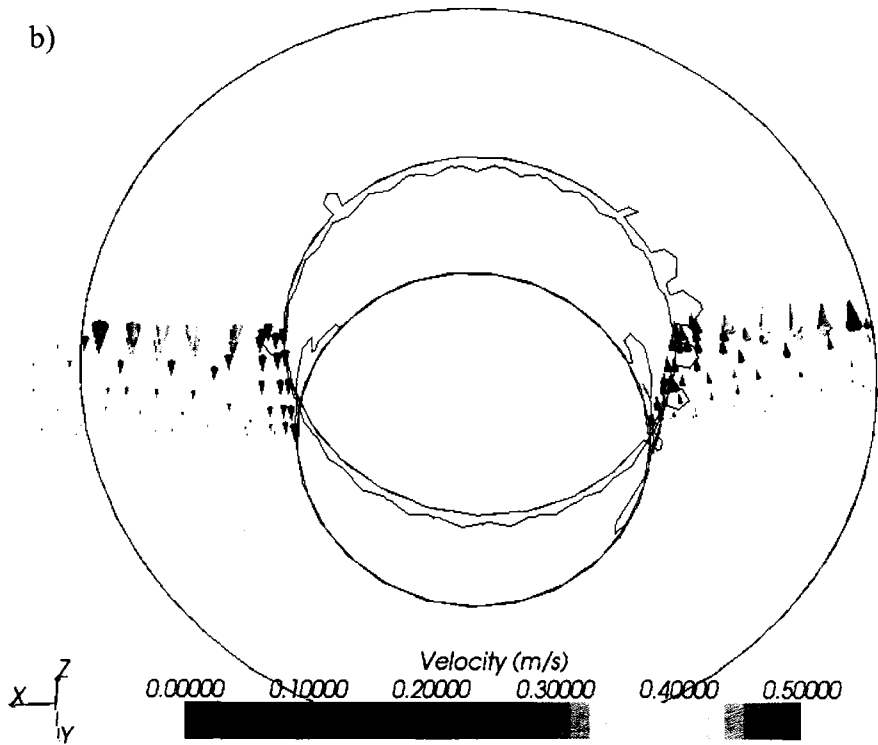
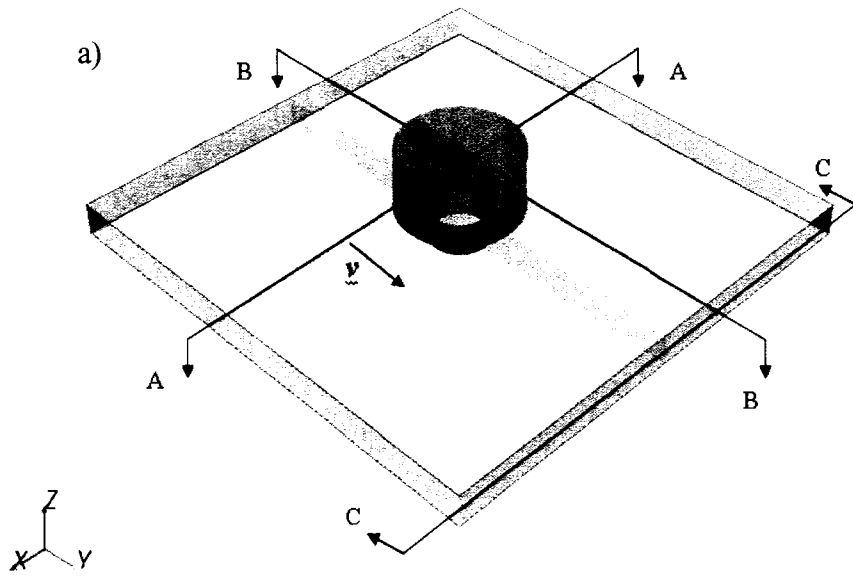


Figure 7- 7 Material's velocity at different radial locations at the middle of the sheet thickness using both CFD analysis and analytical model presented in chapter 6

Figures 7-8 shows the velocity vector fields within the FS processed zone (FS processed at 800 rpm and 0.847 mm/s) for sections taken at different locations; *Figure 7-8(b)* shows a transverse section (section A-A), *Figure 7-8(c)* shows a section taken at the middle of the sheet thickness (section C-C) and *Figure 7-8(d)* shows a section taken along FS processed pass (section B-B). Such figures give useful information about the material flow patterns at different locations within the processed zone, for example *Figures 7-8(b) and 7-8(c)* again show that maximum material velocity is taken place at the outer edge of the shoulder/sheet interface, they also show that within the top region which is close to shoulder; as the radial distance increases the material velocity increases, however this is not the case as going further from the shoulder, *Figure 7-8(d)* shows that at the middle section of the sheet thickness the material velocity decreases as the radial distance increase.



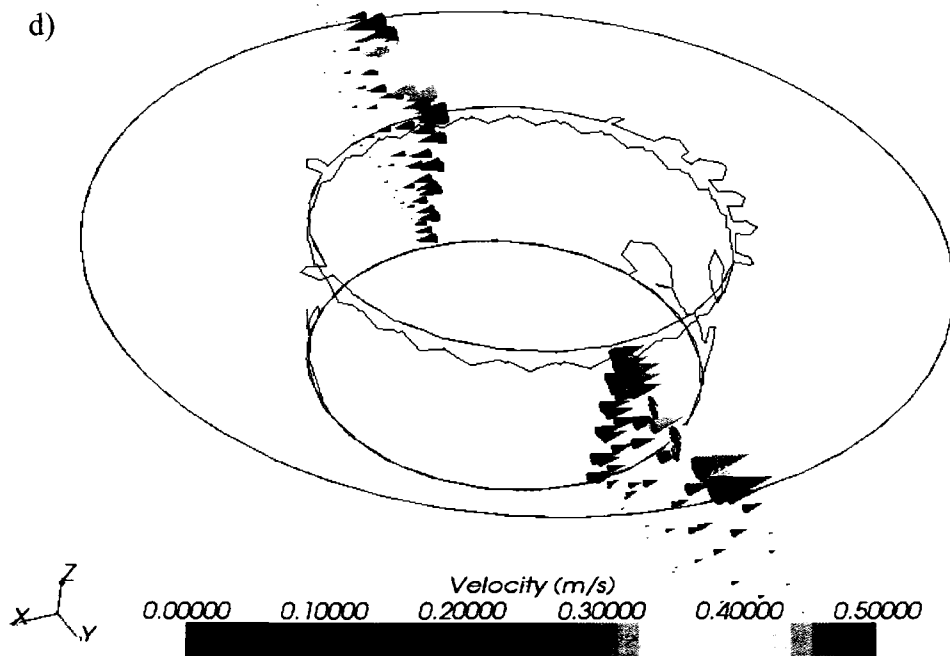
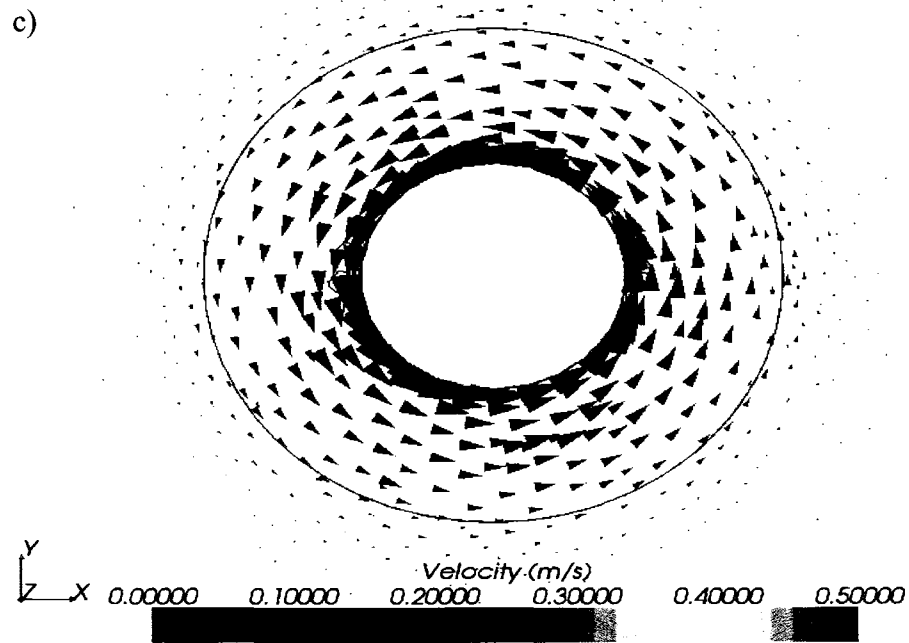


Figure 7- 8 a) Different sections within the model's geometry, b) velocity vector field of a traverse section of FS processed zone (section A-A), c) velocity vector field of a section taken at the middle the sheet thickness (section C-C), and d) velocity vector fields of a section taken along the FS processed pass (section B-B). (FSP at 800 rpm and 0.847 mm/s).

7.5 Conclusions

- The CFD model successfully predicts the velocity fields during FSP and the results are in good agreement with the literature and the results obtained using the analytical model proposed in *Chapter Six*.
- User-defined functions have to be used in order to find the strain rate distributions and to use density and dynamic viscosity as functions of temperature and strain rate, from which a more accurate velocity fields and strain rate distributions can be obtained, in addition to temperature distribution during FSP.
- The mechanical analysis presented in *Chapter Six* and *Seven* have to be coupled with thermal models in order to come up with a comprehensive thermo-mechanical model that can accurately describe the FSP/FSW process.

Chapter Eight

SUMMARY AND RECOMMENDATIONS

8. SUMMARY AND RECOMMENDATIONS

8.1 Concluding Remarks

Integrated multidisciplinary approach has been adapted in this research. Integrated thermo-mechanical and microstructural investigations of friction stir processing of different light weight alloys (5052 aluminium and AZ31 magnesium alloys) have been proposed. The framework of this work involves experimental, numerical and analytical works.

Experimental works have been done to investigate the effect of the process parameter (rotational, translational and tool geometries on resulting microstructure, mechanical properties and thermal distribution during the process. The investigations cover two different materials; 5052 aluminium and AZ31 magnesium alloys. Grain size distributions, hardness distributions and thermal fields during the process have been analyzed.

Analytical mechanical model has been proposed; it successfully predicts velocity fields and strain rate distributions during FSP and it captures the effects of different process parameters (rotational and translational speeds), tool geometry, the interfacial contact conditions at the tool/sheet interfaces. Velocity fields during FSP have also been simulated numerically using CFD code, and the results show good agreement with those obtained analytically.

8.2 Unique Features & Contributions

- ⇒ Friction stir processing is a new innovative microstructural modification technique and lots need to be learned. The first published work in FSP field was in 1998 and since then many researchers have investigated various aspect of the process, however a lot of work have to be done. So any work that helps understand more about the process and its microstructural, mechanical or thermal aspects will contribute to advance FSP.

- ⇒ Integrated multidisciplinary approach is adapted in this work. The framework of this research involves three integrated parts; experimental, numerical and analytical. Experimental; microstructural, mechanical testing in addition to thermal investigations is addressed. Numerical; CFD simulation of the process which shows the material flow during the process is also presented. Analytical modeling work to determine the velocity fields, strain rate is proposed.

- ⇒ Light weight alloy has always been a very hot challenging topic that continuously gains more and more interests especially from automotive and aerospace industries. This research focuses not only on aluminium alloys (which get more attention from the researchers in this field than other metals) but also on magnesium alloys which considered the lightest construction metal on earth, and there is not much work that has been done by other researcher on FSP of magnesium alloys.

8.3 Recommendations for Future Work

- ⇒ Conduction tensile testing to study the effect of FSP on different mechanical properties; ductility, strength etc...

- ⇒ Selectively modifying the microstructure.

- ⇒ Controlling the temperature, cooling and heating rate by coolant during the process.

- ⇒ Using advanced control tools and non-conventional processing protocols in order to control the thermal history along the passes and consequently controlling the microstructure. Such control tools and protocols will utilize using variable speeds during a single pass and applying coolant with controlled rates.

- ⇒ Integrating the thermal fields obtained experimentally and using CFD with the strain rate distribution to correlate them to the resulting grain size through certain parameter such as Zener-Holloman parameter.

- ⇒ Utilizing the current model to design the tool geometry for optimum performance for different materials and applications.

REFERENCES

1. J. Pilling and N. Ridley, "Superplasticity in Crystalline solids", The Institute of Metals, London, UK, (1989).
2. F. K. Abu-Farha, "Integrated Approach to the Superplastic Forming of Magnesium Alloys", Ph.D. dissertation, University of Kentucky, (2007).
3. <http://www.superform-aluminium.com>.
4. <http://www.kcl.ac.uk>.
5. Meyers and Chawla, "Mechanical Metallurgy: Principles and Applications", Prentice Hall, (1984).
6. <http://www2.umist.ac.uk/matsci/research/lap/ECAE.html>.
7. Z. Horita and T. Langdon, "Microstructures and microhardness of an aluminum alloy and pure copper after processing by high-pressure torsion", Material Science and Engineering A, (2005), Vol. 410-411, p. 422-425.
8. W.M. Thomas, E.D. Nicholas, J.C. Needham, M.G. Murch, P Temlesmith, C.J. Dawes, GB Patent Application No. 9125978.8, (December 1991).
9. Mishra, R. S. and M.W. Mahoney, "Friction stir processing: A new grain refinement technique to achieve high strain superplasticity in commercial alloys", Material Science Forum, (2001), Vol. 357-359, p. 2869-2877.
10. Su J., T. W. Nelson and C. J. Sterling, "Friction stir processing of large-area bulk UFG aluminum alloys", Scripta Materialia, (2005), Vol. 52, p. 135-140.
11. Z. Ma, R. Mishra and M. Mahoney, "Superplasticity in cast A356 induced via friction stir processing", Scripta Materialia, (2004), Vol. 50, p. 931-935.

12. M. Khraisheh, B. Darras, P. Kalu, M. Adams-Hughes and N. Chandra, "Correlation between the microstructure and forces generated during friction stir processing of AA5052", *Materials Science Forum*, (2005), Vols. 475-479, p. 3043-3046.
13. A. Dutta, I. Charit, L. Johannes and R. Mishra, "Deep cup forming by superplastic punch stretching of friction stir processed 7075 Al alloy", *Materials Science and Engineering A*, (2005), Vol. 395, p. 173-179.
14. M. Mahoney, A. Barnes, W. Bingel and C. Fuller, "Superplastic forming of 7475 Al sheet after friction stir processing", *Material Science Forum*, (2004) Vol. 447-448, p. 505-512.
15. L. Johannes and R. Mishra, "Multiple passes of friction stir processing for the creating of superplastic 7075 aluminum", *Materials Science and Engineering A*, (2007), Vol. 464, p. 255-260.
16. P. Cavaliere and P. Marco, "Superplastic behaviour of friction stir processed AZ91 magnesium alloy produced by high pressure die casting", *Journal of Materials Processing Technology*, (2007), Vol. 184, p. 77-83.
17. Z. Ma, R. Mishra and M. Mahoney, "Superplastic deformation behavior of friction stir processed 7075Al alloy", *Acta Materialia*, (October 2002), Vol 50, Issue 17, p. 4419-4430.
18. H. Salem, A. Reynolds and J. Lyons, "Microstructure and retention of superplasticity of friction stir welded superplastic 2095 sheet", *Scripta Materialia*, (March 2002), Vol. 46, Issue 5, p. 337-342.

19. L. Johannes, I. Charit, R. Mishra and R. Verma, "Enhanced superplasticity through friction stir processing in continuous cast AA5083 aluminum", *Materials Science and Engineering A*, (2007), Vol. 464, p. 351-357.
20. R. Mishra, L. Johannes, I. Charit and A. Dutta, "Multi-pass friction stir superplasticity in aluminum alloys", *Proceedings of NSF DMII Grantee Conference, Scottsdale, Arizona, DMI-0323725*, (2005).
21. I. Charit and R. Mishra, "High strain rate superplasticity in a commercial 2024 Al alloy via friction stir processing", *Materials Science and Engineering A*, (October 2003), Vol. 359, Issues 1-2, p. 290-296.
22. K. Jata and S. Semiatin, "Continuous dynamic recrystallization during friction stir welding of high strength aluminum alloys", *Scripta Materialia*, (2000), Vol. 43, Issue 8, p.743-749.
23. Y. Kwon, N. Saito and I. Shigematsu, "Friction stir process as a new manufacturing technique of ultrafine grained aluminum alloy", *Journal of Materials Science Letters*, (2001), Vol. 21, p. 1473-1476.
24. M. Mahoney, W. Bingel, S. Sharma and R. Mishra, "Microstructural modification and resultant properties of friction stir processed Cast NiAl Bronze", *Material Science Forum*, (2003), Vols. 426-432, p. 2843-2848.
25. R. Itharaju and M. Khraisheh, "On the forces generated during friction stir processing of aluminum 5052 sheets", *Ultrafine Grained Material III TMS*, (2004).

26. M. Sutton, B. Yang, A. Reynolds and R. Taylor, "Microstructural studies of friction stir welds in 2024-T3 aluminum", *Materials Science and Engineering A*, (2002), Vol. 323, p. 160-166.
27. M. Santella, T. Engstrom, D. Storjohann, and T. Panet al, "Effects of friction stir processing on mechanical properties of the cast aluminum alloys A319 and A356", *Scripta Materialia*, (2005), Vol. 53, p. 201-206.
28. M. Adams-Hughes, P. Kalu, M. Khraisheh and N. Chandra, "Microcharacterization and texture analysis of friction stir processed AA5052 alloy", *Friction Stir Welding and Processing III*, TMS annual meeting (2005), p. 3-10.
29. J. Su, T. W. Nelson and C. J. Sterling, "Friction stir processing of large-area bulk UFG aluminum alloys", *Scripta Materialia*, (2005), Vol. 52, p. 135-140.
30. Y. Sato, H. Park, A. Matsunaga, A. Honda and H. Kokawa, "Novel production for highly deformable Mg alloy plate", *Journal of Material Science*, (2005), Vol. 40, p. 637-642.
31. A. Denquin, D. Allehaux, M.-H. Campaganc and G. Lapasset, "Relationship between microstructural variations and properties of friction stir welded 6056 aluminum alloy", *Welding in the World*, (2002), p.14-19.
32. H. Park T. Kimura, T. Murakami and Y. Nagano, "Microstructures and mechanical properties of friction stir welds of 60% Cu-40% Zn copper alloy", *Materials Science and Engineering A*, (2004), Vol. 371, Issues 1-2, p. 160-169.

33. R. S. Mishra, Z.Y. Ma and I. Charit, "Friction stir processing: a novel technique for fabrication of surface composite", *Material Science and Engineering A*, (2003), Vol. 341, Issues 1-2, p. 307-310.
34. C. Lee, J. Huang and P. Hsieh, "Mg based nano-composites fabricated by friction stir processing", *Scripta Materialia*, (2006), Vol. 54, p. 1415-1420.
35. R. Zettler, A. Blanco J. Santos and S. Marya, "The effect of process parameters and tool geometry on thermal field development and weld formation in friction stir welding of the alloys AZ31 and AZ61", *Magnesium Technology*, TMS, (2005) p. 409-423.
36. S. Lambarkos, R. Fonda, J. Milewski and J. Mitchell, "Analysis of friction stir welds using thermocouple measurements", *Science and Technology of Welding and Joining*, (2003), Vol. 8, No. 5, p. 385-390.
37. A. Askari, S. Silling, B. London and M. Mahoney, "Modeling and Analysis of Friction Analysis of Friction Stir Welding Processes" *Friction Stir Welding and Processing*, TMS, (2001), p. 43-54.
38. M. Song and R. Kovacevic, " Numerical and experimental study of the heat transfer process in friction stir welding", *Proceeding of the Institution of Mechanical Engineers. Part B, Journal of Engineering Manufacture*, (2003), Vol. 217, Issue 1, p. 73-85.
39. T. Nelson, R. Steel and W. Arbegast, "In situ thermal studies and post-weld mechanical properties of friction stir welds in age hardenable aluminum", *Science and Technology of Welding and Joining*, (2003), Vol. 8, No. 4, p. 283-288.

40. A. Reynolds, Z. Khandkar, T. Long, W. Tang and J. Khan, "Utility of relatively simple models for understanding process parameter effects on FSW", *Materials Science Forum*, (2003), Vols. 426-432, p. 2959-2694.
41. C. Chen and R. Kovacevic, "Thermomechanical modeling and force analysis of friction stir welding by the finite element method", *Proceeding of the Institution of Mechanical Engineers. Part C, Journal of Mechanical Engineering Science*, (2004), Vol. 218, p. 509-519.
42. C. Chien, T. Chen and Y. Chao, "Thermal modeling and optimal tool moving velocity for friction stir welding", *Journal of the Chinese Society of Mechanical Engineers*, (2005), Vol.26, No.2, p.195-200.
43. P. Ulysse, "Three-dimensional modeling of friction stir-welding process", *International Journal of Machine Tools & Manufacture*, Vol. 42, (2002), p. 1549-1557.
44. C. Chang, C. Lee and J. Huang, "Relationship between grain size and Zener-Holloman parameter during friction stir processing in AZ31 Mg alloys", *Scripta Materialia*, Vol. 51, (2004), p. 509-514.
45. P. Heurtier, C. Desrayaud and F. Montheillet, "A thermomechanical analysis of the friction stir welding process", *Material Science Forum*, Vol. 396-402, (2002), p. 1537-1542.
46. H. Schmidt, J. Hattel and J. Wert, "An analytical model for the heat generation in friction stir welding", *Modelling and Simulation in Materials Science and Engineering*, Vol. 12, (2004), p. 143-157.

47. W. Arbegast, "Modeling friction stir joining as a metal working process", Hot Deformation of Aluminum Alloys III, TMS, (2003), p. 313-327.
48. J. Schneider and A. Nunes, "Thermo-Mechanical Processing in Friction Stir Welds", Friction Stir Welding and Processing II, TMS, (2003), p. 43-51.
49. R. Nandan, G. Roy and T. Debroy, "Numerical simulation of three-dimensional heat transfer and plastic flow during friction stir welding", Metallurgical and Materials Transactions A, (April 2006), Vol. 37A, p. 1247-1259.
50. G. Buffa, J. Hua, R. Shivpuri and L. Fratini, "A continuum based fem model for friction stir welding-model development", Material Science and Engineering A, (2006), Vol. 419, p. 389-396.
51. L. Fratini and G. Buffa, "CDRX modeling in friction stir welding of aluminum alloys", International Journal of Machine Tools & Manufacture, (2005), Vol. 45, p. 1188-1194.
52. <http://www.matweb.com>.
53. Abu-Farha, F. and M. Khraisheh, "Deformation Characteristics of AZ31 Magnesium Alloy under Various Forming Temperatures and Strain Rates", Proceedings of the 8th ESAFORM Conference on Material Forming, April 27-29, (Cluj-Napoca, Romania), (2005), p. 627-630.
54. Tsao, L., C. Wu, and T. Chuang, "Evaluation of Superplastic Formability of the AZ31 magnesium Alloy", Materials Research and Advanced Techniques, (2001), Vol. 92, No. 6, p. 572-577.
55. B. Darras "Experimental and analytical study of friction stir processing"; Master degree thesis, University of Kentucky (December 2005).

56. J. Su, T. Nelson and C. Sterling, "Grain refinement of aluminum alloys by friction stir processing", *Philosophical Magazine*, (January 2006) Vol. 86, No. 1, p. 1-24.
57. A. Scialpi, L. Filippis and P. Cavaliere, "Influence of shoulder geometry on microstructure and mechanical properties of friction stir welded 6082 aluminum alloy", *Materials and Design*, (2007), Vol. 28, p.1124-1129.
58. S. Kang, H. Chung, H. Han, K. Oh, C. Lee and S. Kim, "Relationship between formability and microstructure of Al alloy sheet locally modified by friction stir processing", *Scripta Materialia*, (2007), Vol. 57, p. 17-20.
59. M. Peel, A. Steuwer, M. Preuss and P. Withers, "Microstructure, mechanical properties and residual stresses as a function of welding speed in aluminum AA5083 friction stir welds", *Acta Materialia*, (2003), Vol. 51, Issue 16, p. 4791-4801.
60. S. Benavides, Y. Li, L. E. Murr, D. Brown and J. McClure, "Low-temperature friction-stir welding of 2024 aluminum", *Scripta Materialia*, (September 1999), Vol. 41, Issue 8, p. 809-815.
61. Y. Kwon, I. Shigematsu and N. Saito. "Mechanical properties of fine-grained aluminum alloy produced by friction stir process". *Scripta Materialia*, (2003), Vol. 49, p. 785-789.
62. P. Cavaliere and P. Marco, "Effect of friction stir processing on mechanical and microstructural properties of AM60B Magnesium alloy", *Journal of Material Science*, (2006), Vol. 41, p. 3459-3464.

63. F. Hung, C. Shih, L. Chen and T. Luet, "Microstructures and high temperature mechanical properties of friction stirred AZ31-Mg alloy", *Journal of Alloys and Compounds*, (2007), Vol. 428, p. 106-114.
64. C. Chang, X. Du and J. Huang, "Achieving ultrafine grain size in Mg-Al-Zn alloy by friction stir processing", *Scripta Materialia*, (2007), Vol. 57, p. 209-212.
65. Y.S. Sato, M. Urata, H. Kokawa and K. Ikeda, "Hall-Petch relationship in friction stir welds of equal channel angular-pressed aluminum alloys", *Materials Science and Engineering A*, (2003), Vol.354, p. 298-305.
66. M. Sutton, B. Yang A. Reynolds and R. Taylor, "Microstructural studies of friction stir welds in 2024-T3 aluminum", *Materials Science and Engineering A*, (2002), Vol. 323, p. 160-166.
67. A. Denquin, D. Allehaux, M.-H. Campaganc and G. Lapasset, "Relationship between microstructural variations and properties of friction stir welded 6056 aluminum alloy", *Welding in the World*, (2002), p. 14-19.
68. D. Hofmann and K. Vecchio, "Thermal history analysis of friction stir processed and submerged friction stir processed aluminum", *Materials Science and Engineering A*, (2007), Vol. 465, p. 165-175.
69. K. Oh-ishi, A. Zhilyaev, S. Swaminathan, C. Fuller, B. London, M. Mahoney and T. McNelley, "Stir zone temperature during friction stir processing", *Friction Stir Welding and Processing IV*, TMS , (2007), p. 403-407.
70. M. Song and R. Kovacevic, "Heat transfer modeling for both workpiece and tool in friction stir welding process: a coupled model", *Proceeding of the Institution of*

- Mechanical Engineers. Part B, Journal of Engineering Manufacture, (2004), Vol. 218, p. 17-33.
71. A. Reynolds, W. Lockwood and T. Seidel, "Processing-property correlation in friction stir welds". Materials Science Forum, (2000), Vols. 331-337, p. 1719-1724.
72. J. Xu, S. Vaze, R. Ritter, K. Colligan and J. Pickens, "Experimental and numerical study of thermal process in friction stir welding", Proceeding of Joining of Advanced and Specialty Materials, (October 2003), p.13-15, ASM international (2004), p. 10-19.
73. R. Zettler, A. Blanco, J. Santos and S. Marya, "The effect of process parameters and tool geometry on thermal field development and weld formation in friction stir welding of the alloys AZ31 and AZ61", Magnesium Technology, TMS, (2005), p. 409-423.
74. P. Vilaca, L. Quintino, J. Santos, R. Zettler and S. Sheikhi, "Quality assessment of friction stir welding joints via an analytical thermal model, iSTIR", Material Science and Engineering A, (2007), Vol. 445-446, p. 501-508.
75. O. Frigaard, O. Grong and O. Mildling, "A process model for friction stir welding of age hardening Aluminum alloys", Metallurgical and Materials Transactions A, (May 2001), Vol. 32A, p. 1189-1200.
76. M. Omar, M. Hassan, K. Satio, K. Donohue, and R. Alloo, "Infrared Thermography for inspecting the adhesion integrity of plastic welded joints", Journal of International NDT&E, (2006), Vol. 39, p. 1-86.

77. N. K. Del Grande and P. F. Durbi, "Stimulated Dual-Band Infrared Computed Tomography: A Tool to Inspect the Aging Infrastructure", SPIE Optical Science, Engineering, and Instrumentation Conference San Diego, CA July 9-14, (1995).
78. <http://www.magnesium-elektron.com>.
79. G. Buffa, J. Hua, R. Shivpuri and L. Fratini, "Design of the friction stir welding tool using the continuum based FEM model", Materials Science and Engineering A, (2006), Vol. 419, p. 381-388.
80. M. Stewart, G. Adams, A. Nunes and P. Romine, "A combined experimental and analytical modeling approach to understanding friction stir welding", Developments in Theoretical and Applied Mechanics, (1998), Vol. XIX, p. 472-484.
81. M. Song and R. Kovacevic "Thermal modeling of friction stir welding in a moving coordinate system and its validation", International Journal of Machine Tools & Manufacture, (2003), Vol. 43, p. 605-615.
82. B. Darras, M. Omar and M. Khraisheh, Experimental thermal analysis of friction stir processing, Materials Science Forum, (2007), Vol. 539-543, p. 3801-3806.
83. L. Malvern, "Introduction to the mechanics of continuous media", Prentice-Hall, (1969), p. 526.
84. M. Ericsson, L. Jin and R. Sandstrom, "Fatigue properties of friction stir overlap welds", International Journal of Fatigue, (2007), Vol. 29, p. 57-68.
85. Kh. Hassan, A. Norman, D. Price and P. Pragnell, "Stability of nugget zone grain structures in high strength Al-alloy friction stir welds during solution treatment", Acta Materialia, (2003), Vol. 51, p. 1923-1936.

86. H. Zhang, Z. Zhang and J. Chen, "3D modeling of material flow in friction stir welding under different process parameters", *Journal of Materials Processing Technology*, (2007), Vol. 183, p. 62-70.
87. P. Colegrove and H. Sherchiff, "2-Dimensional CFD modeling of flow round profiled FSW tooling", *Friction Stir Welding and Processing II*, TMS, (2003), p. 13-23.
88. H. Schmidt and J. Hattel, "CFD modeling of the shear layer around the tool probe in friction stir welding", *Friction Stir and Processing III*, TMS, (2005), p. 225-232..
89. T. Long, T. Seidel, W. Tang and A. Reynolds, "A friction stir welding model using computational fluid dynamics", *Hot Deformation of Aluminum Alloys III*, TMS, (2003), p. 299-312.
90. User Guide, Modeling Guide and Training Guide. STAR-CCM+, CD-adapco Computational Dynamics Ltd, (2005).
91. User Guide and Tutorials. STAR-Design Version 4.02. CD-adapco Computational Dynamics Ltd, (2005).

VITA

Basil Mohammad Darras

Date and Place of Birth

- May 28, 1978 Amman, Jordan.

Education

- Masters of Science in Manufacturing Engineering, University of Kentucky, Lexington KY, USA, 2005.
- Bachelor's degree in Mechanical Engineering, University of Jordan, Amman, Jordan, 2001.

Experience

- Teaching Assistant (Aug. 2003- Dec. 2008) (Mechanical Engineering Department -University of Kentucky, Lexington, Kentucky, USA).
- Research Assistant (Jul. 2003- Present) (Mechanical Engineering Department - University of Kentucky, Lexington, Kentucky, USA).
- Mechanical Engineer (Aug. 2001- Jul. 2003) (Consolidated Consultants Amman, Jordan).
- Technical Training (Practicum) (Jul. 2000- Sep. 2000) (Maintenance Division - Royal Jordanian, Amman, Jordan).

Awards & Honors

- Awarded Kentucky Graduate Scholarship by University of Kentucky to make a poster presentation at the TMS 2007 meeting (March 2007).
- Awarded Kentucky Graduate Scholarship by University of Kentucky to make a presentation at The 3RD International Conference on Structural Stability & Dynamics (June 2005).
- The paper "Finite Element Modeling and Optimization of Superplastic Forming Using Variable Strain Rate Approach" was highlighted in ASM international news letter Volume 5 Issue 7 2005.
- United Nation Five-year Scholarship (1996-2001).

Publication

Refereed Journal Papers

- "Analytical Modeling of Strain Rate Distribution during Friction Stir Processing"; **B. Darras** & M. Khraisheh; *ASM Journal of Materials Engineering and Performance* (Accepted In-press).
- "Friction stir processing of AZ31 commercial Magnesium alloy"; **B. Darras**, M. Khraisheh, F. Abu-Farha & M. Omar; *Journal of Materials Processing Technology* Vol. 191(1-3) (2007) pp. 77-81.

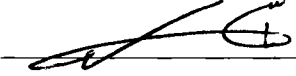
- “Experimental thermal analysis of friction stir processing”; **B. Darras**, M. Omar & M. Khraisheh; *Materials Science Forum* Vols. 539-543 (2007) pp. 3801-3806.
- “Correlation between the microstructure and forces generated during friction stir processing of AA5052”; M. Khraisheh, **B. Darras**, P. Kalu, M. Adams-Hughes & N. Chandra; *Materials Science Forum* Vols. 475-479 (2005) pp. 3043-3046.
- “Finite element modeling and optimization of superplastic forming using variable strain rate approach”; M. Nazzal, M. Khraisheh & **B. Darras**; *ASM Journal of Materials Engineering and Performance*, Vols. 13(6) (2004) pp. 691-699.

Posters and Presentations

- “Modeling of strain rate distribution during Friction stir processing”; **B. Darras** & M. Khraisheh; was presented at the 18th AEROMAT conference (Baltimore, MD) (June 2007) (*Presenter*).
- “Thermo-mechanical investigation of friction stir processing of 5052 Aluminum sheets”; **B. Darras** & M. Khraisheh; was presented as a poster in the TMS annual meeting (Orlando, Florida) (March 2007) (*Presenter*)
- “Investigation of “Wear” During the Processing of Aluminum Sheet Alloys”; G. Jha, W. Yin, **B. Darras**, M. Khraisheh and S. Ningileri; TMS 136th Annual Meeting (Orlando, Florida) (March 2007).
- “Integrated approach to superplastic forming of advanced materials”; M. Khraisheh, F. Abu-Farha, M. Nazzal & **B. Darras**; was presented as a poster in the DMII-MPM NSF Conference (St Louis, MO) (2006).
- “Friction stir processing”; **B. Darras** & M. Khraisheh; was presented at the 3RD International Conference on Structural Stability & Dynamics (Orlando, FL) (June 2005) (*Presenter*)
- “Friction stir processing”; **B. Darras**; was presented at the Sustainability Seminar-Center for Manufacturing -University of Kentucky (Lexington, KY) (April 2005) (*Presenter*)
- “Friction stir processing: a tool to produce nanocrystalline sheet metals”; **B. Darras** & M. Khraisheh; was presented as a poster in the International Workshop of Nanomaterials (Lexington, KY) (2004) (*Presenter*)

Other Publications

- “Experimental and analytical study of friction stir processing”; **B. Darras**; *Master degree thesis*, University of Kentucky (December 2005).
- “Full mechanical systems for a hospital”; **B. Darras**, F. Jucka & M. Omari; *Bachelor degree graduation project*, University of Jordan (January 2001).



 02/18/2008